SURFACE MODIFICATION OF IRON AND ALUMINUM BY ELECTROLYTIC PLASMA PROCESSING

by

ADAM J. SMITH

Presented to the Faculty of the Graduate School of
The University of Texas at Arlington in Partial Fulfillment
of the Requirements
for the Degree of

DOCTOR OF PHILOSOPHY

THE UNIVERSITY OF TEXAS AT ARLINGTON
August 2014

Acknowledgements

I would like to thank my advisor, Dr. Meletis, for allowing me to propose this research and to pursue it and for the guidance offered during the course of this research. I would also like to acknowledge the large amount of work that was done by the Materials Science and Engineering staff, specifically Jennifer and Beth. Whether it involved ordering material, scheduling appointments, or booking flights their help was very much appreciated and a good portion of this work was able to be accomplished because of their help. I would also like to acknowledge the help received from the Surface and Nano-Engineering Laboratory members. Finally, I would like to thank my wife, Lauren Cooper, for her support in this endeavor and the countless hours she spent listening to me talk and discuss various aspects of this project.

June 11, 2014

Abstract

SURFACE MODIFICATION OF IRON AND ALUMINUM

BY ELECTROLYTIC PLASMA PROCESSING

Adam Smith, PhD

The University of Texas at Arlington, 2014

Supervising Professor: Efstathios I. Meletis

Electrolytic Plasma Processing (EPP) is an emerging, clean surface modification technology which is able to both clean and, depending on the circuit polarity, deposit either cationic or anionic species from an aqueous electrolyte. EPP offers several benefits including environmental cleanliness, high deposition rates, and a nanograined surface structure. The following work presents research conducted on EPP, including surface cleaning of Fe and deposition of Ni onto Fe and Al substrates. Investigations were made into the microstructure of the surface as well as the atomic compositions of the coating and coating/substrate interface. EPP cleaning was initially conducted in order to determine optimum processing conditions for later work on EPP deposition as well as to determine the capabilities of the process.

EPP deposition of Ni onto Fe substrates was then conducted utilizing the process parameters determined from the EPP cleaning process. Coating thickness, deposition rate and coating coverage were determined and corrosion properties of the coated samples were then investigated. Best results were obtained for a deposition time of 30 s which resulted in a positive shift of the corrosion potential of 200 mV and a reduction of the corrosion rate of ~37%.

Research progressed to the application of EPP deposited Ni onto Al substrates. An investigation into the effect of deposition voltage onto coating quality and composition was conducted in order to determine optimum coating properties. Two processing conditions were chosen and were conducted at three separate deposition times: 185 V for 30 s, 60 s, or 90 s, and 210 V for 30 s followed by 30 s, 60 s, or 90 s at 185 V. Coating thickness, deposition rate and coverage were determined. Investigations into the mechanical properties, including hardness and tribological properties, and corrosion properties of the two conditions were conducted. It was determined that the coating process containing the initial 210 V step formed a discontinuous, intermetallic interlayer which proved to be beneficial to both the mechanical and corrosion properties of the samples.

Table of Contents

List of Illustrations

List of Tables

Chapter 1

Introduction

1.1 Introduction and Motivation

Due to its high strength-to-weight ratio, aluminum has seen increasing use in the automotive and aerospace industries. However, due to aluminum's low hardness and poor corrosion properties when compared to other available metals, its use is limited to areas in which wear is not a significant factor [1]. While some aluminum alloys, particularly those of the Al-Si system, have shown improved tribological properties, these alloys have yet to greatly improve aluminum's role in wear situations. The application of a hardened surface coating may be the most effective method of improving the wear performance of aluminum alloys.

As previously noted, most aluminum used for tribological applications contains silicon. In these alloys, the wear resistance is attributed to the hardness of the dispersed Si containing phases in the Al-Si alloys. It has been reported that wear resistance increases with increasing Si content up to the near-eutectic composition, after which wear resistance decreases as Si content increases [2].

Additionally, some work has been conducted on improving the performance of aluminum through the addition of surface coatings. Research has been conducted on surface coatings, such as nitride and nickel coatings, as well as on surface coatings consisting of metal matrix composites. The benefit of these coatings is still being researched, with some coatings, particularly those consisting of Al_2O_3 [3] or Ni_3Al particles [1] created via a metal powder compaction method, showing a marked decrease in wear performance while others, particularly those containing SiC particles [3], show an

improvement in performance. In the previous cases, the Al_2O_3 or Ni_3Al particles tend to pull out of the metal aluminum matrix and act as additional abrasive, whereas the SiC particles remain fixed in the matrix and contribute to increased wear resistance. Additionally, the application of surface coatings in order to improve the surface properties of the metal is inherently difficult due to the well-known tendency of aluminum to immediate form an Al_2O_3 barrier layer upon exposure to air and/or water.

1.2 Research Objectives

It is clear that lightweight materials such as aluminum exhibit several highly desirable properties, yet, due to their lack of appropriate surface properties, such as hardness and corrosion resistance, the scale of their use has been limited. Further research into the development of a protective wear surface for aluminum is needed. The formation of surface coatings via Electrolytic Plasma Processing (EPP) is a relatively new process, with investigations into this area taking place mostly within the last decade. Previous work in our lab investigated the effect of substrate and coating melting point on the composition of the final coating by examining the coatings formed by the deposition of Zn, Ni and Mo onto an Fe substrate. This study, however, did not examine any substrate other than Fe and it is believed that a material with a lower melting point may exhibit different characteristics. Additionally, no published work has been conducted on EPP of low melting temperature materials.

The deposition of nickel onto aluminum via EPP shows promise as a method for achieving this coating material. Similar to the deposition of molybdenum onto iron demonstrated by Cionea, the high local deposition temperature should result in molten aluminum existing as a base onto which nickel deposition will occur. Based on the

understanding of melting temperature effect presented by Cionea [4], this should result in the diffusion of aluminum into the nickel layer, creating a gradually increasing Ni content in the coating. This will result in the formation of a coating consisting of nickel-aluminum intermetallics, which should result in an improvement of the surface qualities of the substrate.

The specific objectives of the present research are:

- To understand the substrate/coating interface as a function of various EPP characteristics – power, electrolyte concentration, anode-cathode separation distance, and flow rate – in order to best utilize the capabilities of the process. The steel-nickel system will be used as a model system for this understanding due to the considerable amount of previous research into this system.
- Apply the knowledge gained from the steel-nickel system to study the EPP interaction with low melting point materials, specifically aluminum, and their surface modification through the development of intermetallics on their surface.

1.3 Dissertation Overview

The dissertation consists of seven chapters. A brief description of each chapter is given below.

Chapter 1 – Introduction: A brief summary of the motivation behind the current work is presented as well as a quick overview of the current state of Al tribological research.

Chapter 2 – Literature Review: An in-depth overview of several subjects which are pertinent to work conducted in this dissertation are presented in this chapter. Sections

contained in this chapter include overviews of Nickel-Aluminum intermetallics and their application to tribological systems, Ni coatings (predominantly formed via electroless deposition) and their current state of research as applied to aluminum substrates, and an overview of the anodic as well as the cathodic electrolytic plasma processing (EPP) mechanisms and their uses.

Chapter 3 – Experimental Methods: This chapter contains descriptions of all characterization procedures conducted as well as details of the materials used and experimental set-up.

Chapter 4 – Effect of Process Variations on Surface Morphology and Current Density of EPP Cleaning on 1018 Steel: Initial experiments involved verifying that the Surface and Nano-Engineering Laboratory (SaNEL) EPP system performed adequately. Once this verification was accomplished, optimization of several processing variables was conducted. The results from these initial experiments and validations are presented here.

Chapter 5 – EPP Deposition and Characterization of Ni deposited on Fe: EPP depositions were conducted on low carbon steel substrates and the resultant coatings were then characterized. Analyses was then conducted on the corrosion properties of the Ni coatings which were then compared against the corrosion properties of the substrate as well as commercially pure Ni. These results are presented in this chapter.

Chapter 6 – EPP Deposition and Characterization on Ni deposited on Al: This chapter contains all relevant work conducted on the deposition of Ni via EPP onto an Al substrate and subsequent characterization of the resultant coating. Analyses of the corrosion and

wear properties of the EPP Ni coating was conducted and compared to that of commercially pure Ni and the commercially pure Al substrate.

Chapter 7 – Conclusions: Summaries of the work conducted in this dissertation is presented in this chapter.

Chapter 2

Literature Review

2.1 Ni Coatings

One realm of current research into improving the surface properties of Al involves the application of a pure Ni coating. While several methods exist in order to deposit Ni onto Al with some of the most noteworthy being laser alloying [5], and plasma spraying [6], by far the best established is electroless deposition. The application of a Ni coating to metals through an electroless process is a rather well established process on most metals. While electroless Ni coatings can be used for many different purposes, the majority of its use has been due to its tribological and corrosion resistant properties [7]. While the electroless process is relatively simple when depositing on most metals the process becomes complicated when dealing with an Al substrate due to the extremely strong electronegativity of Al which results in almost instantaneous oxidation of the exposed metal surface when in contact with water or air. This thin, tenacious aluminum oxide layer prevents contact of any surface coating with the underlying metal, decreasing the strength of adhesion between the coating and the substrate [8]. The majority or coating techniques attempt to remove the oxide layer through a mechanical of chemical action prior to coating. While most coating techniques struggle to remove this oxide layer a process has been developed to achieve this with electroless Ni deposition.

The deposition of Ni through an electroless process is commonly conducted by utilizing hypophosphite as the reducing agent. This invariably results in the inclusion of small amounts of P in the Ni layer, and thus the coating are often referred to as Ni-P coatings [8]. The deposition process tends to consists of several steps involving:

1. Solvent degreasing utilizing either acetone of tri-chloroethylene in ultrasound frequently for 5-10 minutes.
2. Alkaline cleaning in a strong base in order to remove the original oxide layer. This solution consists of sodium carbonate (Na_2CO_3) and trisodiumorthophosphate ($Na_3PO_4*12H_2O$) for a total time of 3-4 minutes.
3. Acid cleaning in a solution of sulphuric acid, hydrofluoric acid, and nitric acid or a solution of orthophosphoric acid and nitric acid for 3-4 minutes.
4. An initial zincating stage for 1 minute. This process removes the oxide layer and replaces it with a thin, porous zinc layer via a displacement reaction of aluminum and zinc [8].
5. Stripping of the first zinc layer through a process involving a nitric acid for 0.5-2 minutes in order to improve the quality of the zinc layer and thus improve the subsequent adhesion strength of the coating.
6. Re-zincating for 0.5- 1 minute providing a coating of zinc consisting of layer of uniform and compact fine grains.
7. Electroless Ni plating. [9] [10]

The above process can range in duration from 13 minutes up to 22 minutes without including the Ni plating step (which will vary depending on the desired thickness of the final coating). Additionally the process utilizes several strong and dangerous acids and bases. It can be seen that while the deposition of Ni onto Al is practiced, the current method certainly leaves a great deal to be desired in terms of efficiency and environmental impact.

The application of electroless Ni-P coatings has received a great deal of attention for use as a corrosion resistance coating and as a coating for protection from wear on

many substrates, particularly steels. The properties of the coating are observed to improve for these applications upon heat treatment at 400° C for 1 hr. This has been shown to result in a phase change of the coating which transforms the metastable phase (as deposited P saturated Ni) into a dual phase structure consisting of Ni and Ni_3P. Furthermore, it has been determined that further heat leads to a decrease in the hardness and an increase in the wear rate of the coating, likely due to grain coarsening. While these temperatures are acceptable for use with steel substrates as they cause no structural changes to the steel itself, when this degree of heat treatment is applied to a coating on an aluminum substrate the effect is quite noticeable. Some of the most widely used Al alloys are of the 6xxx series which attain their desired properties through use of precipitation hardening achieved at low temperatures (125-200°C). At temperatures above 200° C, the hardened structure is damaged, leading to a decrease in substrate hardness and an expected premature failing of the coating due to cracking caused by the softer substrate. Low temperature (~200° C) for 1 hr was shown to result in a slight improvement of low- to medium-P coatings' properties while having little to no effect on the properties of the Al substrate [11].

Coatings of Ni-P can fall into three broad categories, low-P (1-3 wt. % P), medium-P (4-7 wt. % P), and high-P (>8 wt. % P), which are created by varying the initial P level of the solution [12]. Several advantages exist for each of the coatings when compared to the others and determination of the most advantageous P content is dependent on the desired properties. High-P coatings have been shown to offer an improved corrosion resistance and compressive stresses but results in a decrease of the fatigue properties of high strength steels. Additionally, medium-P coatings deposited an Al can either increase or decrease the fatigue properties of the coatings depending on the aluminum substrate being studied [13].

Additional improvements to the coating wear resistance and corrosion resistance can be achieved by the incorporation of high hardness particles such as SiO_2 [12] or SiC [14]. It has been determined that coatings containing hard particles, such as Al_2O_3, SiC, and B_4C, improve the overall hardness and wear properties whereas inclusion of softer particles, such as graphite, MoS_2 and PTFE, have been shown to be preferable for lubricating requirements. Of the above listed particles, SiC has been determined to be the most advantageous particle for co-deposition when the requirement is that the coating be highly resistant to abrasion [14]. In this case, the SiC particles are simply entrapped in the Ni-P matrix (i.e. there is no chemical binding between the particles and the coating). At temperatures between 450° C and 650°C the formation of Ni_3Si occurs which is expected to more securely anchor the particles into the Ni-P matrix. Figure 2-1 shows the improvement in hardness achieved with heat treatment of the Ni-P electroless coatings with and without zincating as well as coatings containing Si-C particles. Nevertheless, it should be noted that while this is useful in the application of electroless Ni coatings onto Fe based substrates, the heat treatment temperature is far higher than what can typically be applied to Al substrates for reasons detailed previously. However, in aluminum alloys with high Si content, frequently used in engine components, operating temperatures can exist above 400° C. In these alloys a 400° C heat treatment for 1 hour was shown to improve the resistance of the material to abrasive wear by 20 times when compared to the uncoated substrate [7]. Further, research is ongoing in order to overcome the issue with heat treating and resultant effects that can occur to the Al substrate. Research on laser alloying the surface layer is one such method currently being conducted [7] [5].

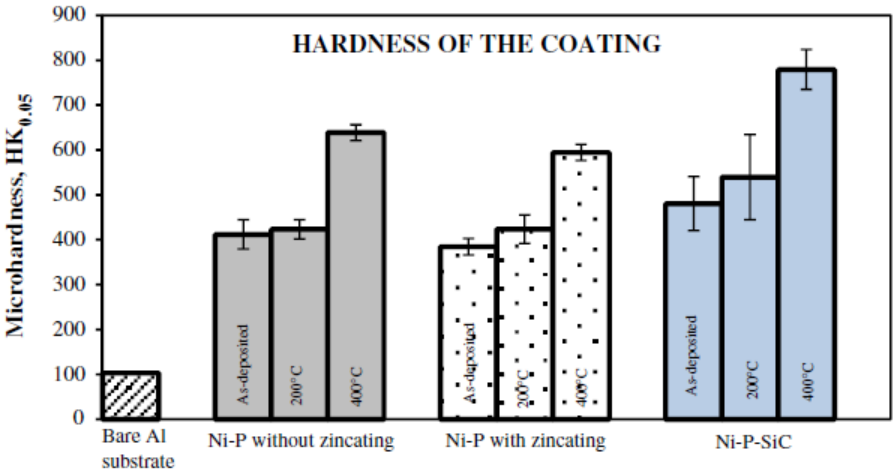

Figure 2-1. Microhardness of Ni-P electroless coatings with and without SiC particle co-deposition.

Additional uses for the improvement of electroless Ni-P coatings is due to their corrosion resistance properties. Several studies have been conducted which detail the improved corrosion resistance of the Ni-P coatings on steels. These studies suggest that the inclusion of particles into the Ni-P matrix results in corrosion resistance of equal or better performance for similar coating thicknesses. These particles tend to be those which also offer improved tribological properties, such as Al_2O_3, TiC, Si_3N_4, and SiC. However, limited work has been conducted on the corrosion resistance of Ni-P or Ni-P/particle composite coatings. An improvement to the corrosion resistance has been shown through the co-deposition of Ni-P and SiO_2. It was found that corrosion rate decreases with increasing concentration of SiO_2 particles up to 4.5 wt. % after which the corrosion rate increases. The initial improvement is attributed to the particles acting to prevent the expansion of corrosion cavities while the latter increase in corrosion rate above 4.5 wt. % is attributed to the agglomeration of the SiO_2 particles [12].

2.2 Intermetallic Coatings

One option to improve the surface properties of aluminum is the application of an intermetallic layer consisting of nickel aluminide. Nickel aluminides are well-researched intermetallic compounds. There are four stable intermetallics of nickel and aluminum ($NiAl_3$, Ni_2Al_3, NiAl, and Ni_3Al) as well as one metastable phase (Ni_5Al_3) which can be seen in the phase diagram shown in Figure 2-2 [15]. In general, nickel-aluminide intermetallics exhibit high melting points, high corrosion resistance, high chemical stability, low density, low friction coefficient, and improved wear performance [16] [17] [18]. However, these materials also exhibit poor ductility and fracture toughness at low temperatures. While the drawbacks are severe enough to prevent these materials from structural applications, they have limited effect on these materials' use as a surface coating, and they are ideally suited to coating situations in which they are exposed to wear, corrosion, or high temperature oxidation [16]. Ding et al. showed that NiAl coatings deposited via PVD exhibited greatly improved wear rate and a decreased coefficient of friction when compared to pure aluminum [19], and the coefficient of friction was found to be approximately that of steel sliding on steel by Blau and DeVore [20].

While nickel aluminide intermetallic coatings have been relatively well researched, no single formation process has been found to be preferred over the many others. Currently, these coatings are generally created by one of several methods including: PVD, reactive sintering, reactive casting, pack cementation, thermal spraying, laser cladding, or high velocity oxy-fuel thermal spraying [21]. Of these techniques, pack cementation and high velocity oxy-fuel spraying have emerged as the two most used

processes, however, each of these methods has exhibited some serious limitations. Pack cementation, while possibly being the most useful for industry due to its ability to coat complex geometries and its low cost [22], has some severe limitations due to its long processing times at elevated temperature including: the inability to retain any pre-coating heat treatment, the presence of microstructural changes, pronounced grain coarsening in both the coating and the substrate, poor bonding, and material porosity [18]. Coatings produced by high velocity oxy-fuel thermal spraying, while dense, adherent and homogeneous, consist of several overlapping lamellae which has been shown to alter the tribological properties of these coatings when compared to the better studied bulk material [23] [24]. With these limitations in mind it is clear that new processing methods of applying these coatings needs to be developed.

2.3 Electrolytic Plasma Processing

Plasma Electrolytic Deposition (PED) is an emerging coating technique which, although first demonstrated in the 1960's, has only begun to be heavily studied in the past decade. PED exhibits some very promising attributes including: high deposition rate, relative simplicity, good coating adhesion, ecological friendliness, and the ability to deposit both metals and non-metals. While PED has been shown to be commercially feasible, its use in industry is still limited and additional research into possible applications for its use is still needed [25].

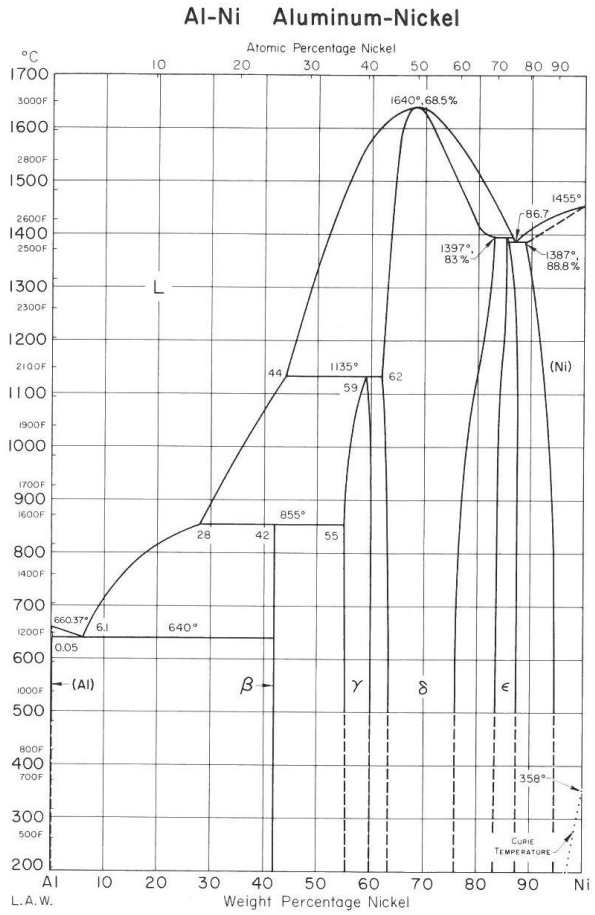

Figure 2-2. Al-Ni phase diagram [15].

2.3.1 Electrolytic Plasma Processing for the Deposition of Metallic Coatings

The EPP process consists of an aqueous electrolyte which serves as a conductive bridge between two electrodes, one of which is the workpiece to be treated. Depending on the desired process, the workpiece can either be treated as the anode (in which case non-metal deposition occurs) or the cathode (in which case either cleaning or deposition of metal species takes place) of the electrical circuit. The anodic process, often referred to as plasma electrolytic arc oxidation (PEAO), plasma electrolytic

oxidation (PEO), or micro-arc oxidation (MAO), has been rather well researched and coatings consisting of carbon, nitrogen, oxygen, boron, and combinations of these elements have been well documented [26]. The cathodic regime, often referred to as plasma electrolytic saturation (PES), electrolytic plasma processing (EPP) or cathodic plasma electrolysis (CPE), while being less well researched, has been shown capable of cleaning of metal surfaces and deposition of metal coatings such as Mo, V, Ni, Zn, Cu, Al, and others [25] [26] [27].

The cathodic process occurs in four distinct phases, easily discerned from the corresponding V-I diagram, shown in Figure 2-3. During the initial regime, U_1, current increases linearly with voltage and is accompanied by the evolution of gas due to the electrolysis of water; in this case H_2. As voltage increases further, the system begins to deviate from the previously observed linearity and current begins to decrease, U_2. This is accompanied by frequent flashes of gas luminosity. At U_3, the cathode is completely surrounded by continuous plasma and a marked drop in current occurs. This is the regime in which EPP treatment is conducted and controllable surface treatment is possible. As voltage is further increased, U_4, current begins to increase. This is accompanied by increased, and intense arcing along the sample surface resulting in detrimental effects on the sample [25].

In the cathodic process, application of an electric potential results in the evolution of hydrogen gas through the electrolysis of water forming small, fine hydrogen bubbles on the sample surface. Metal cations in the electrolyte solution, usually added to the electrolyte, though occasionally present due to the reduction of the anode material, are drawn towards the cathodically charged workpiece. The hydrogen bubbles act as a barrier to the migration of these metal cations, and effectively form small capacitors. The electric field present due to this formed capacitor causes the hydrogen gas to ionize,

forming a high temperature plasma which, due to its high temperature, expands before becoming unstable and rapidly collapses. The high temperature plasma, estimated at between 2000 and 6000 K [25] [28], melts the adjacent surface, and the cations ride the collapsing bubble shockwave, which can have a pressure on
the order of several hundred MPa [25], and thus are incorporated into the molten layer. The electrolyte then acts to quench the molten surface, resulting in a cooling rate of ~10^8 K/s and a surface morphology consisting of micro-craters and protruding spheroids with nanocrystalline grain size. Additionally, this rapid cooling has the effect of causing certain high temperature phases and super saturated solid solutions to be retained within the surface layer [28]. The entire process is extremely rapid, complete hydrogen bubble life is approximately 1 ms and hydrogen plasma exists for between 1 and 10 µs [29]. It should be noted that this process does not occur as a continuous plasma but as a layer of discreet plasma discharges across the surface of the workpiece [25] [26]. A schematic of the EPP process is given in Figure 2-4.

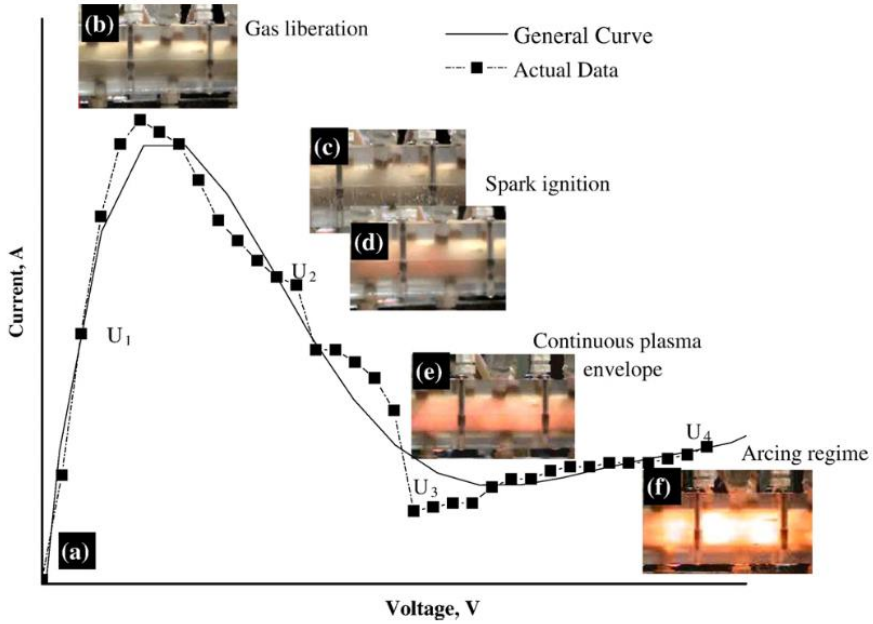

Figure 2-3. Typical V-I diagram of the EPP process [25].

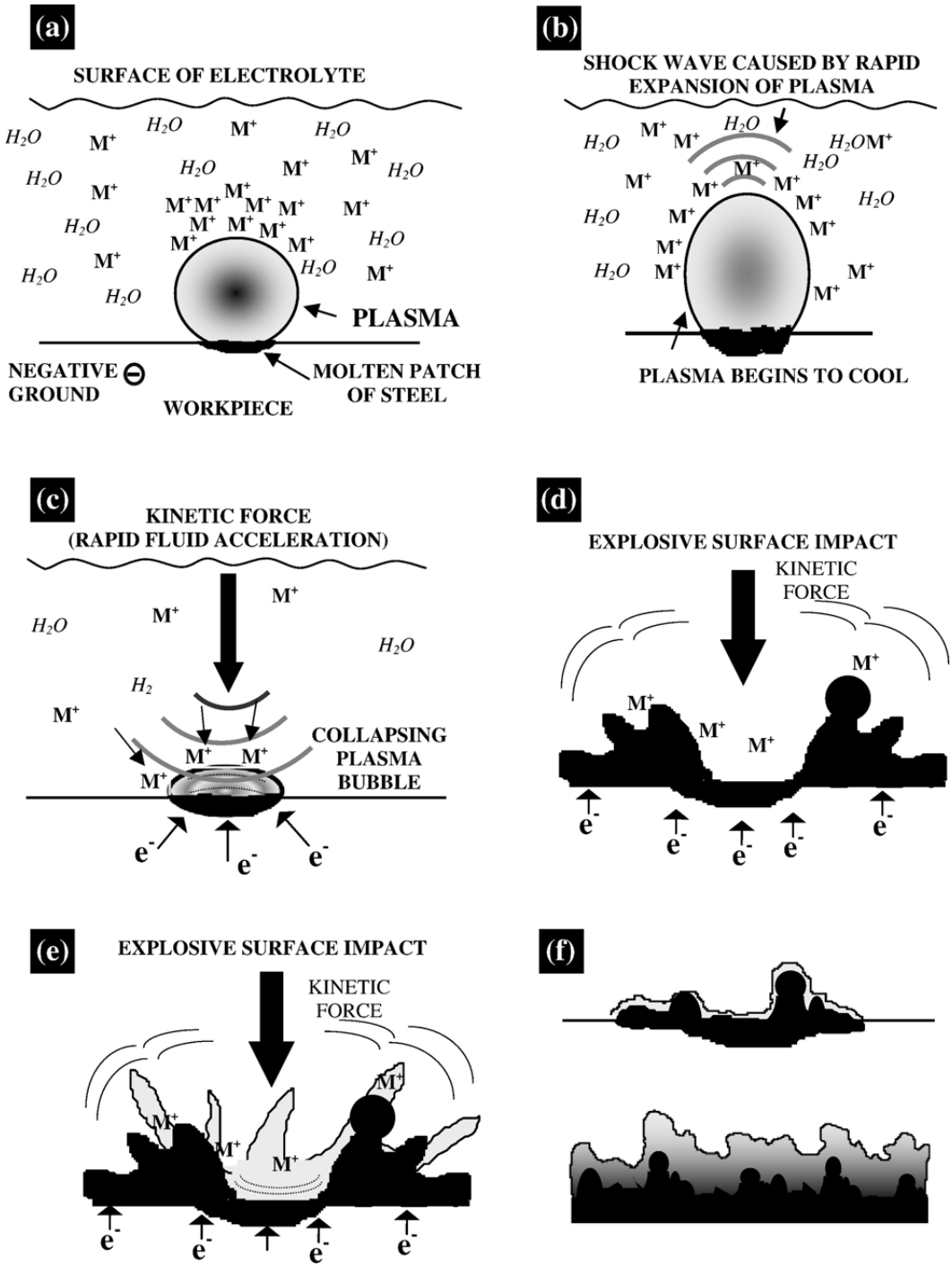

Figure 2-4. Schematic representation of individual hydrogen bubble formation, rupture, and ionic species deposition [25].

In order to better comprehend the underlying process of EPP, an understanding of the many variables' effect on surface properties is needed. While current research into the cathodic deposition process is limited, much work has gone into the anodic process and it can be assumed that these two processes behave similarly with regards to parameter changes and their effects on the final surface coating. Specific parameters of interest are: voltage and melting temperature of both the substrate and deposition metal. Research has shown that voltage tends to have an extremely important role in controlling the final characteristics of the surface coating. Aliofkhazraei et al determined that increasing voltage led to an increase in the corrosion resistance of 316L stainless steel due to increasing deposition rate and thus an increase in coating thickness. However, this study also reported that simply increasing the coating thickness via longer deposition time did not have as beneficial of an effect as increased thickness due to higher voltage. This demonstrates that higher voltage played a separate role other than just raising the deposition rate. Furthermore, it was found that increasing voltage led to an increase in the average nanocrystalline size and also led to a deeper diffusion zone which was attributed to an increase in the power of the ion bombardment allowing for a deeper penetration of the depositing ions [30].

The final parameter of interest is the melting points of the substrate and depositing metal. It was shown by Cionea [4] that the relationship between these two temperatures determines the final composition and extent of the interface of the surface coating. It was found that as the ratio of the substrate T_m and coating metal T_m increases,

the thickness of the mixed zone decreases and the outer, pure metal coating thickness increases. This relationship exists up to a point beyond which it is believed that the substrate is continuously molten which results in the penetration of the substrate material far into the coating. In the Mo coatings produced by Cionea, the surface composition still showed small percentages of Fe even though the thickness was 15-20 μm thick.

Recent results in EPP have shown some remarkable achievements. The simplest EPP process, and therefore the process offering the easiest path to commercialization, is cleaning. In this process an electrolyte, typically consisting of $NaHCO_3$ [28] [25] [31] (though other electrolytes are possible), is used to form the H+ plasma. Due to the nature of the conducting ions in the electrolyte, deposition does not occur. The H+ plasma acts to rapidly clean the surface of the workpiece of any dirt, oxides, or organics which may be present. The speed at which this is achieved, as well as the environmental cleanliness of the process makes this EPP cleaning a highly desirable process. A schematic of the steps needed for traditional acid pickling and for EPP cleaning is presented in Figure 2-5. EPP cleaned iron has shown a higher (more noble) open-circuit potential (OCP) compared to the untreated material when corrosion experiments were conducted in tap water, and in solutions containing sulfuric acid and NaCl an order of magnitude lower corrosion rate was observed in EPP cleaned steel compared to grit blasted steel [25]. Clearly, EPP cleaning offers some considerable advantages over traditional cleaning methods.

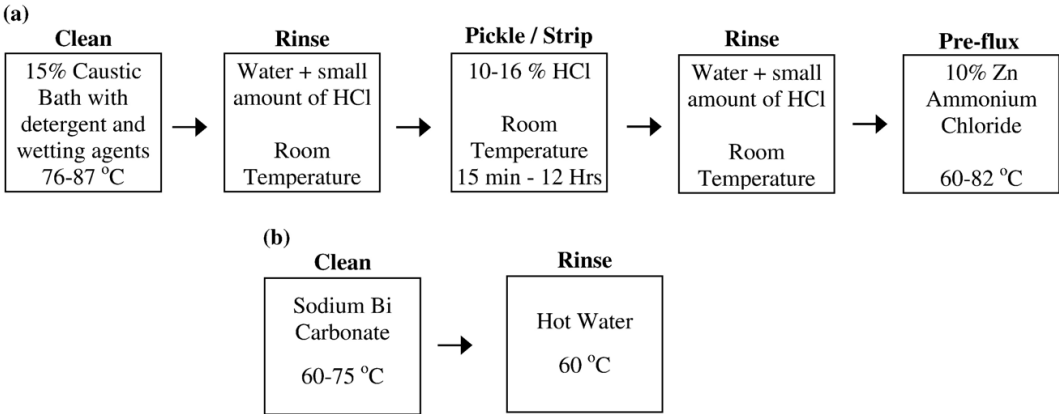

Figure 2-5. Comparison of steps necassary for cleaning in traditional cleaning (a) and EPP cleaning (b) [25].

While EPP cleaning is a process which presents several advantages serious research is further progressing the understanding of the capabilities of EPP as a metal coating process. As mentioned previously, coatings consisting of Mo, V, Ni, Zn, Cu, Al, and others [25] [26] [27] have been created. As a coating technique, EPP offers the advantages over traditional techniques of possessing high deposition rates, nanocrystalline grain structure (which tends to only be present in the coating allowing for the retention of desirable subsurface grain structures), and high interfacial bonding [25]. Typically, coatings tend to exist in two layers: a thin transition zone covered by a layer consisting of nearly 100% the depositing species. This can be seen in reported results from Meletis et al. In their experiments Zn coatings were formed through EPP using AISI 1010 steel. Results showed a small transition zone covered by a much thicker Zn layer. It should be noted that dual deposition of Zn and Al was attempted but very little (~3 at. %) Al was achieved in the coating. Corrosion experiments conducted on the EPP Zn coated samples showed the possible benefit of these coatings as a useful sacrificial anode layer.

Two recent results have deviated from the presence of this two phase coating structure and instead have shown the ability of EPP to form coatings consisting entirely of an alloy of the two materials. The first, involves the deposition of Mo onto Fe. In this case, even after a thick coating was formed, Fe atoms were found to be present throughout the coating, although in decreasing concentrations further from the substrate. Cionea attributed this difference in coating structure to be due to the much higher melting temperature of Mo compared to the substrate, Fe. In this case it was believed that a molten bed of Fe was formed onto which Mo was slowly deposited. As this deposition occurred, Fe was able to rapidly diffuse upwards into the Mo layer. High hardness was reported in these coatings [4] [32]. The second deviation from the typical two stage coating was reported by Aliofkhazraei. In this instance, Al was deposited via a bipolar EPP method. In this method, a relatively dense coating was formed which was observed to consist of Ti and Al with an increasing Al concentration further from the substrate. A cross-sectional SEM micrograph and cross-sectional EDS spectra of this Ti-Al coating is given in Figure 2-6. While the deposition rate was much slower than in a typical EPP deposition (~40 μm in slightly over 3 hr) the ability to deposit Al is something that is typically not capable with other non-vacuum deposition technologies [27].

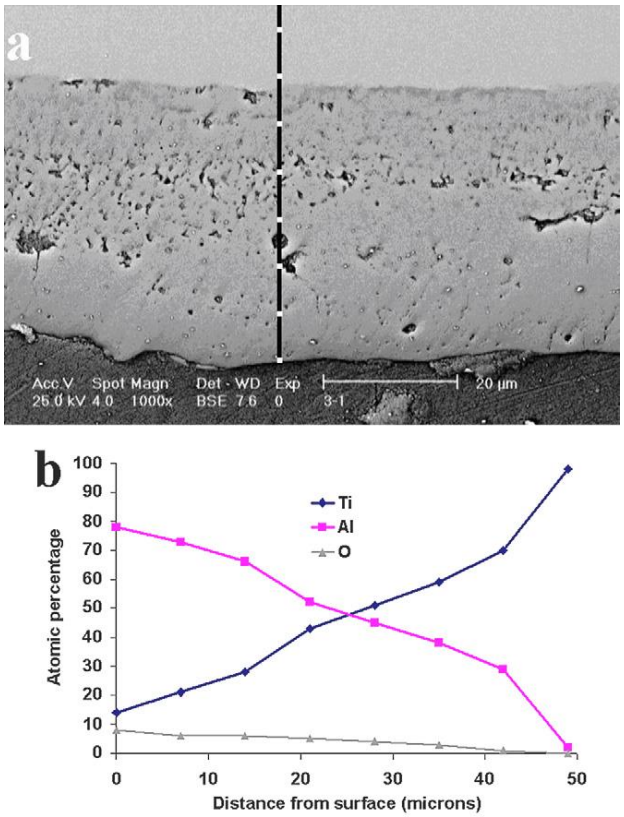

Figure 2-6. Cross-sectional SEM microhraph (a) and EDS spectra (b) of Al deposited on Ti via pulsed bipolar EPP [27].

2.3.2 Plasma Electrolytic Oxidation

Plasma Electrolytic Oxidation (PEO), also known as Micro Arc Oxidation (MAO), Anode Spark Deposition (ASD) [33], and Plasma Anodizing [34], is a coating technology that has gained much interest as of late for its high efficiency and its ability to effectively form ceramic coatings on Al, Ti, Mg, and other valve metals [35]. PEO utilizes high anodic potentials, above the dielectric breakdown voltage of the film [36], which lead to microdischarges along the metal-electrolyte boundary and large gas evolution. This, in

turn, leads to the formation of a thin plasma layer covering the metal sample [37]. The plasma temperature has been estimated to range from 6800 – 7800 K [38]. However, due to the large volume of surrounding electrolyte the surface is almost instantaneously quenched; cooling rates are approximately 10^8 K/s, which allows for the retention of high temperature phases (α- and γ-Al_2O_3, anatase and rutile TiO_2, δ-Nb_2O_5, etc.) [39]. The presence of large amounts of oxygen gas present, due to the breakdown of water, combined with the high surface temperatures caused by the plasma leads to the rapid formation of oxide coatings [39]. Additionally, the inclusion of different salts in the electrolyte results in certain species being incorporated into the oxide film creating more complex oxide structures [39].

PEO typically results in a three-layered surface coating between 50 and 150 μm thick. The outer layer contains large cavities and pores and typically contains much higher ratios of ions present in the electrolyte than the underlying layers due to the increased distance from the substrate. The middle layer is typically dense, with some presence of sub-micrometer pores and microcracks, while the inner layer, also called the barrier layer, is typically 200 – 500 nm and is considered to be the reason for the high interfacial adhesion of PEO coatings [40]. It should be noted that this inner layer is often ignored and is not reported in many papers and the coatings are thus often considered to have a two-layer structure. The surface of PEO coatings generally consists of pan-like structures centered on a small discharge channel through which molten substrate material migrates to the surface as illustrated in Figure 2-7. The molten substrate material

then comes into contact with the electrolyte, quenching, oxidizing and absorbing ions present in the electrolyte.

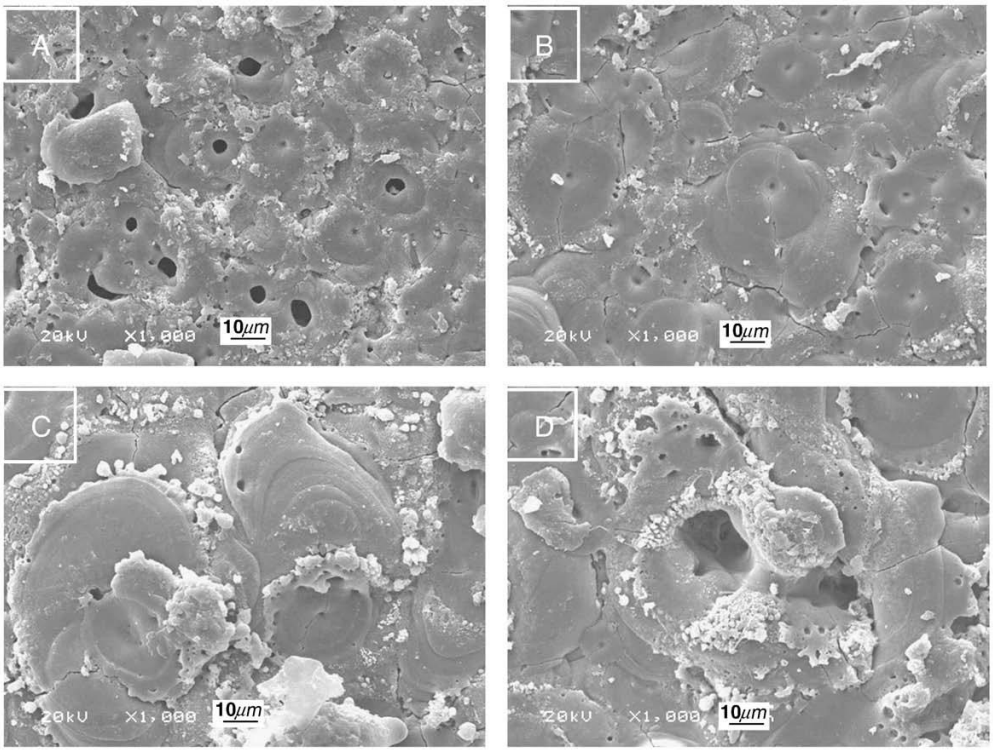

Figure 2-7. Typical surface morphology of a PEO oxide film. AlON-Al_2O_3 film is shown with deposition times of (a) 5 min, (b) 10 min, (c) 15 min, and (d) 30 min [35].

Several factors have been attributed to modifying the surface structure, coating formation rate, and general properties. The most prevalent of these are voltage, processing time, and electrolyte composition and concentration.

Initially, PEO experiments were carried out under a DC mode. However, recent experiments have determined that the use of pulsed DC and biased AC or pulsed bipolar current results in a thicker and more dense structure with fewer defects and improved properties. As stated previously, PEO occurs due to the presence of microdischarges on

the sample surface. These discharges have a lifetime of up to 4 ms and if allowed to continuously occur, as in the pure DC mode, some of these discharges are able to gain strength and lead to damage of the surface coating. However, in the pulsed DC mode a voltage difference is generally applied for only 100 – 500 μs which prevents discharges from lasting for their entire potential lifetime. This leads to much less damage to the coating. In the biased AC or pulsed bipolar current modes the lifetime of the microdischarges is similarly limited, however, due to the opposite polarization for part of the cycle, a small amount of the oxide coating deposited on the previous half-cycle is reduced and reenters the electrolyte. This has the added benefit of decreasing the surface roughness by preferentially reducing those features most prominently exposed to the plasma. In addition to the current mode, the voltage value has been shown to have an effect on the coating. Increasing the voltage has been shown to increase the deposition rate, due to creating a more intense plasma, however increasing voltage has also been linked to decreasing film quality [41]. Figure 2-8 clearly shows that as voltage is increased the surface roughness and pore diameter increase drastically.

In order for the PEO process to take place the conductivity must be maintained at a particular level. Beyond this requirement of the electrolyte, the composition of the electrolyte itself has been shown to have dramatic effects on the quality of the coatings that are produced. This can clearly be seen when the surface morphologies of a PEO coating created with an electrolyte containing Na_2SiO_3-NaOH is compared to a coating created with an electrolyte containing $(NaPO_3)_6$-NaOH in Figure 2-9. In addition to the electrolyte having an effect on the surface morphology, it is also able to influence the atomic composition of the coating as well. The formation of an oxide coating containing mullite, AlON, and various Zr compounds has been reported [42] [43] [44].

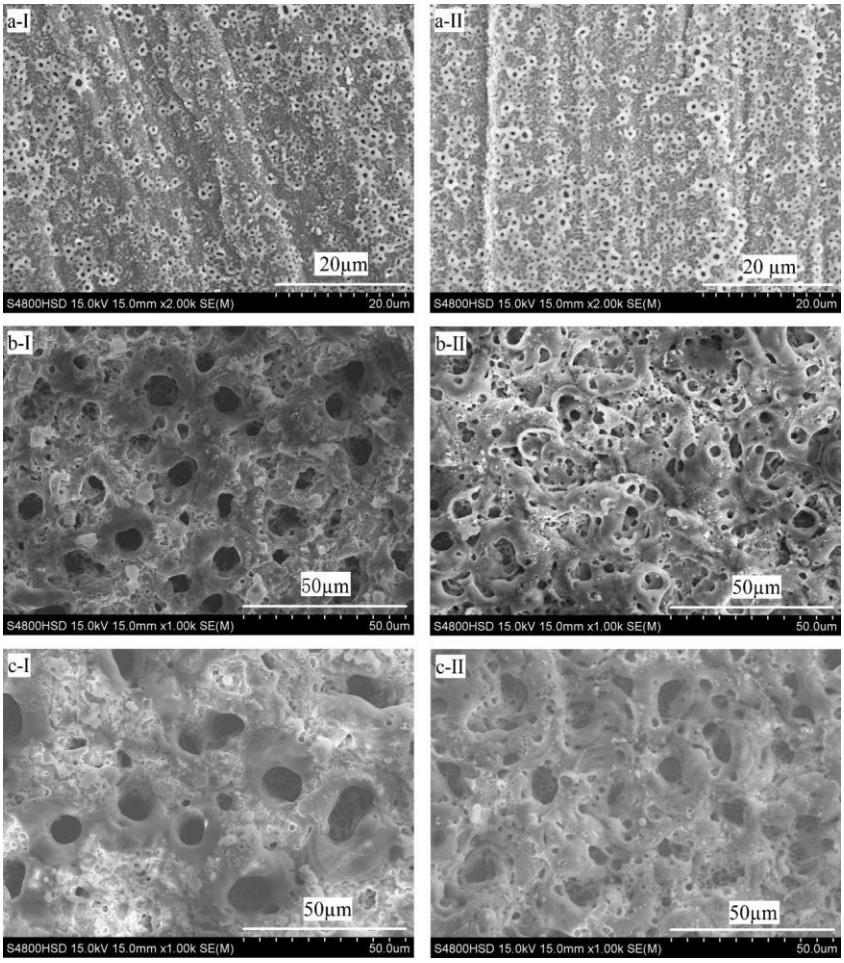

Figure 2-8. Surface morphology of Ti_6Al_4V due to increasing voltage - (a) 400 V, (b) 470 V, (c) 480 V - and increasing frequency - (I) 100 Hz, (II) 1000 Hz [39].

The final processing parameter which effects PEO is the duration of the process itself. As would be expected, increasing the deposition time increases the thickness of the ceramic layer. Slightly less intuitive however, is the effect that increasing processing time has on the surface roughness of the sample. The effects of processing time can be seen in Table 2-1, showing that as processing time increases, the roughness

(represented by the standard deviation of thickness) increases substantially due to the plasma preferentially forming around prominent features. Additionally, increased processing times have been linked to an increased hardness in the coating [43].

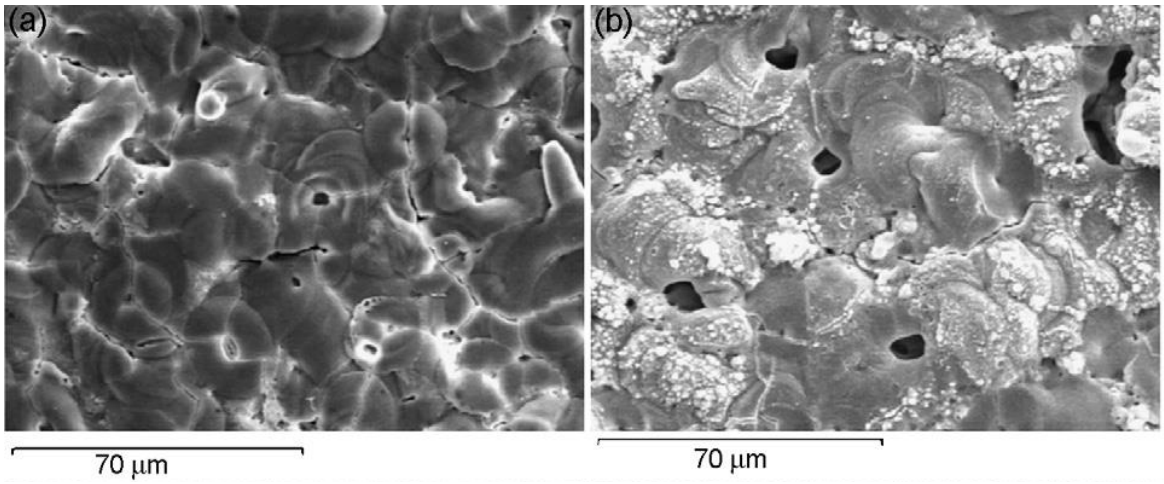

Figure 2-9. SEM micrographs of a surface prepared with (a) Na_2SiO_3-NaOH and (b) $(NaPO_3)_6$-NaOH under identical concentrations and processing parameters [31].

Table 2-1. Thickness parameters of PEO coating on Ti alloy at various processing times [42].

Time (min)	10	20	40	60
Mean thickness (μm)	12.1	19.8	35.2	52.8
Max thickness (μm)	13.4	21.6	38.6	63.7
Min thickness (μm)	10.6	16.8	31.2	38.6
Standard deviation	0.8	1.8	2.1	7.8

2.3.3 Plasma Electrolytic Saturation for the Formation of Non-Metallic Coatings

Plasma Electrolytic Saturation (PES) is the overall term for processes involving the formation of non-oxide ceramics. PES processes form surface layers containing carbon, nitride, boride, or a combination of these elements and the individual processes are termed Plasma Electrolytic Carburizing (PEC), Plasma Electrolytic Nitriding (PEN), Plasma Electrolytic Boronizing (PEB), etc. While PEO utilizes anodic potentials, PES is capable of using either anodic or cathodic potentials but has been shown to be more effective when operating under the cathodic regime [45]. Under cathodic polarization hydrogen gas rapidly evolves on the sample surface due to the electrolysis of water. Increasing voltage causes an ionization of the gas bubbles which expand and then rapidly collapse. The species present in the electrolyte are pulled along with the collapsing plasma bubble and bombard the sample surface which is molten due to the plasma temperature. A schematic of the interface reactions is shown in Figure 2-10. This leads to a high diffusion rate, 200-250% greater than that associated with gas carburizing or pack metalizing, and thus a rapid growth of the surface coating [39]. A prominent example of this is the reported ability of PES to create a borided layer on steel of several millimeters in only 15 minutes of processing [45].

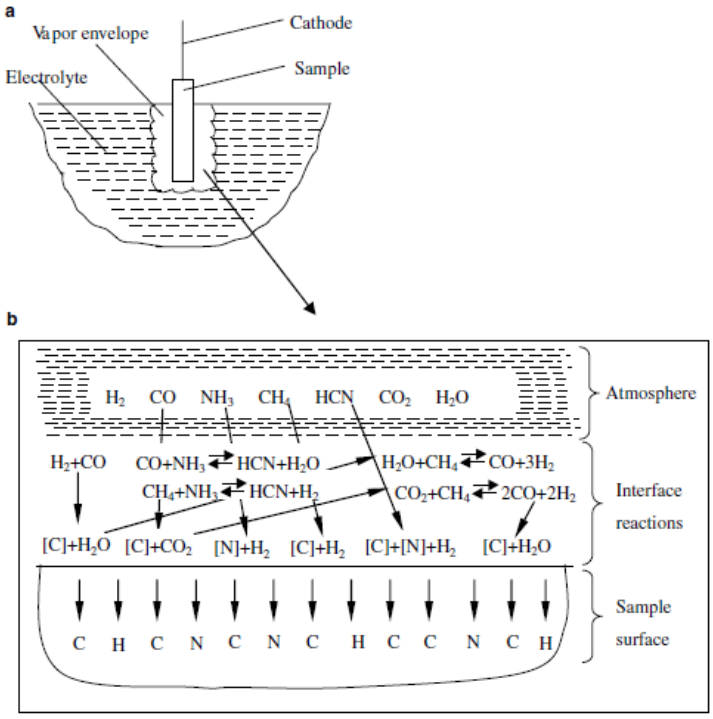

Figure 2-10. Schematic of the carbonitriding system and reactions [44].

The PES process results in a porous surface layer as shown in Figure 2-11 [46]. As can be seen, the film consists of evenly spaced and fully disconnected pores and, upon higher magnification, a grain size in the nano regime. Similarly to PEO, the PES process results in a two layer structure consisting of an outer ceramic layer and an inner diffusion layer. The outer layer has a relatively uniform composition which changes abruptly at the interface with the diffusion layer. The diffusion layer thickness varies depending on the ceramic coating being formed. The composition of the diffusion layer starts at that of the outer layer and, due to the fact that this is a diffusion controlled process dominated by the anionic species, changes at a linear rate to that of the substrate [46]. This has been reported to have a high effect on the adhesion of the

surface coating due to the gradual compositional change of the diffusion zone and due to the mechanical working of the surface by the plasma as the coating is formed [45].

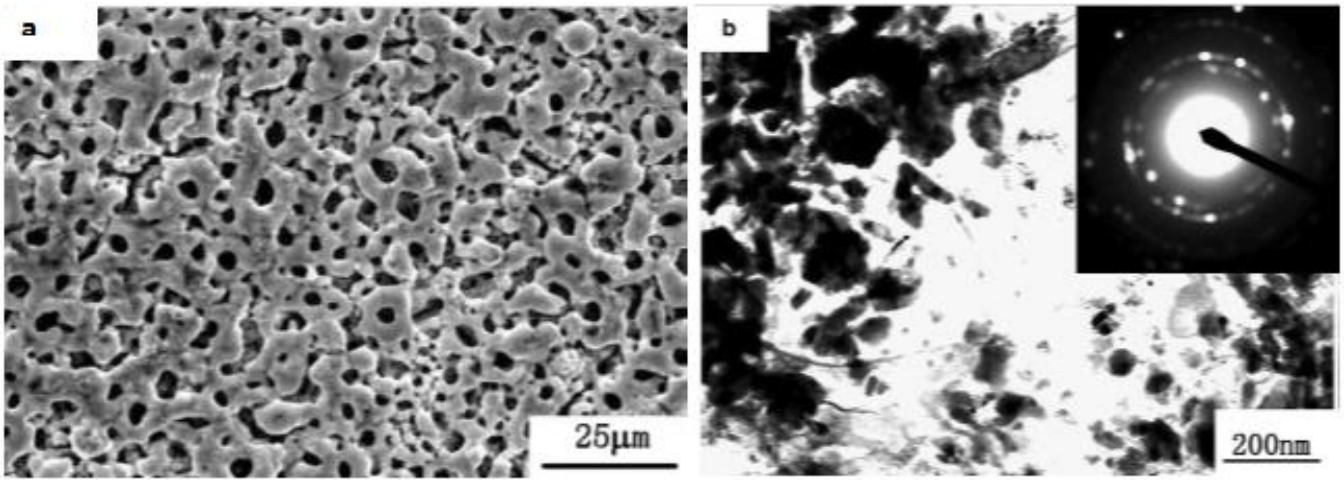

Figure 2-11. (a) SEM and (b) TEM of carbonitrided Ti after 2.5 hr. discharge time [46].

While PEO can be carried out under DC treatment, it has been found that pulsed DC, and in particular higher frequencies of pulsed DC, is needed in order to promote the diffusion of treating species into the metal substrate in PES. In an attempt to carburize aluminum via PES no carbon was detected in the substrate when subjected to 1 kHz pulsed DC, while a pulsed frequency of 10 kHz did result in carbon infiltration. Moreover, the effect of duty cycle is much more pronounced in PES than it is in PEO. With a duty cycle greater than 40%, the carbon content was three times less than that in a sample treated at less than 40% duty cycle and this was attributed to the fact that at duty cycles greater than 40% the sample begins to melt and then oxidizes which inhibits the carbon diffusion [47]. Higher voltage is also linked to higher coating growth rate which is ascribed to the increase temperature and thus higher diffusion rate [48]. Figure 2-12 shows the relationship that voltage and deposition time have on the thickness of the

coating. Also, as noted earlier, PES can take place anodically, but better results are obtained in the final coating if the treatment is carried out cathodically. This is clearly illustrated by the hardness values for a boronized steel sample carried out under both regimes shown in Figure 2-13.

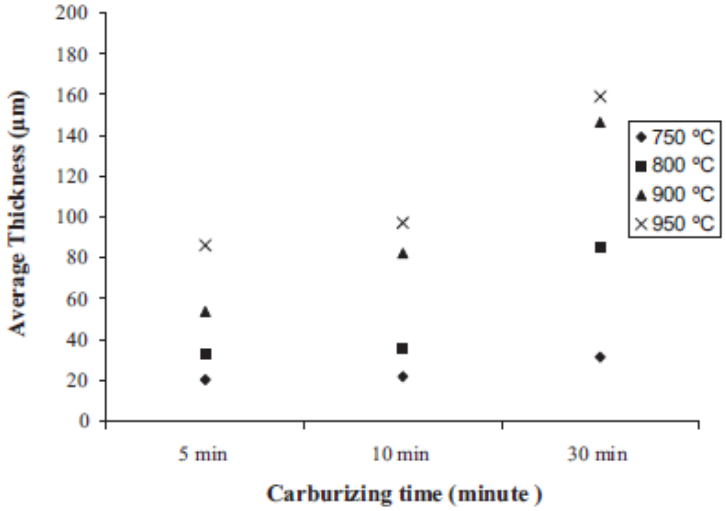

Figure 2-12. The effects of deposition time and voltage on coating thickness for carburizing of pure iron. 750 °C, 800 °C, 900 °C, and 950 °C correspond to the voltages 180 V, 200 V, 220 V, and 240 V, respectively [46].

The electrolyte composition has the expected effect of controlling the final composition of the coating (i.e. a carbonitride coating must have an electrolyte with both carbon and nitrogen present). Also, as would be expected, increasing the concentration of the electrolyte increases the deposition/diffusion rate of the anionic species, and

adjusting the composition ratio of the electrolyte (i.e. more or less nitrogen in a carbonidriding electrolyte) will result in a change in the final stoichiometry of the coating.

Two major effects of processing time have been reported for PES: increased thickness with increased processing time, which can be seen in Figure 2-12 earlier, and increased roughness with increased processing time. The reason for increased thickness is intuitive, and the reason for the increased roughness is similar to that for the PEO process. One notable effect not reported in PEO is that as discharge time is increased the diameter of the pores reported in the coating surface tends to decrease [46].

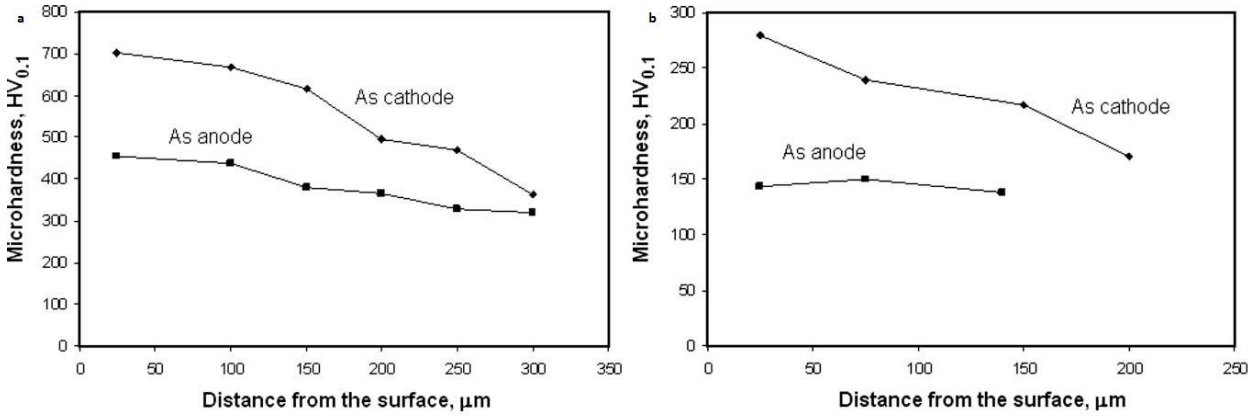

Figure 2-13. Effect of polarity on cross-sectional hardness of (a) 4140 steel and (b) 1020 steel treated in 5% borax electrolyte for 10 min [43].

Chapter 3

Experimental Methods

3.1 Materials

Substrates used in the experiments conducted in this research were composed of 1018 steel and Aluminum 1100 (commercially pure Al), for simplification these two substrates are referred to as Fe, and Al, respectively. Disc samples were machined to a diameter of 12.7 mm (0.5 in.) and a height of 8.96 mm (0.353 in.); #8-32 tapped hole was centered on one round side in order to attach the substrate to the cathode arm of the Surface and Nano-Engineering Laboratory (SaNEL) EPP setup (a dimensioned schematic of the samples is given in Appendix A for reference). All samples were ground with 600 grit SiC polishing paper before being rinsed with methanol and dried with compressed air.

Two different electrolyte solutions were utilized depending on the particular experiment being conducted. For the EPP cleaning process, a $NaHCO_3$ electrolyte was utilized at a concentration of 12%. It should be noted that this concentration was varied with values of 8%, 10%, and 12% in order to determine the effect of electrolyte concentration. When the experimental concentration was not 12% it will be clearly specified. For EPP deposition of Ni typically a 20% $NiSO_4$ electrolyte was used with a resultant pH of ~3.8 and a conductivity of ~ 44 mS/cm at a temperature of 75° C. Similar to the electrolyte used for the cleaning solution, this value was altered at times to determine its effect and when this is the case it will be clearly specified.

3.2 Electrolytic Plasma Processing

The SaNEL EPP chamber is shown below in Figure 3-1. It consists of an acrylic plastic housing with a fully removable lid. An acrylic plastic tube passes through the removable top and height adjustment is provided by a vertically mounted screw attachment. A stainless steel receiver is attached to the bottom of the tube into which a graphite anode is screwed, shown in Figure 3-2, allowing for easy replacement of damaged and/or worn anodes (a dimensioned drawing of the replaceable anode is given in Appendix B for reference). Additionally, this configuration allows for the use of anodes of different material, such as Ni, Mo, Zn, etc. which may prove beneficial in the deposition of certain materials, although this capability was not utilized in the current research. A copper rod enters through the side of the acrylic housing and a screw located at the end allows for easy and secure fastening of the substrate. Power was supplied by an Advanced Energy 10K power supply for initial experiments and a Sorrensen SGA 600-17 power supply capable of producing 10 kW of power and a maximum voltage and current of 600 V and 17 A respectively, for all coating experiments. Electrolyte was pumped through the system with a centrifugal pump and flow-rate is adjustable via an inline valve.

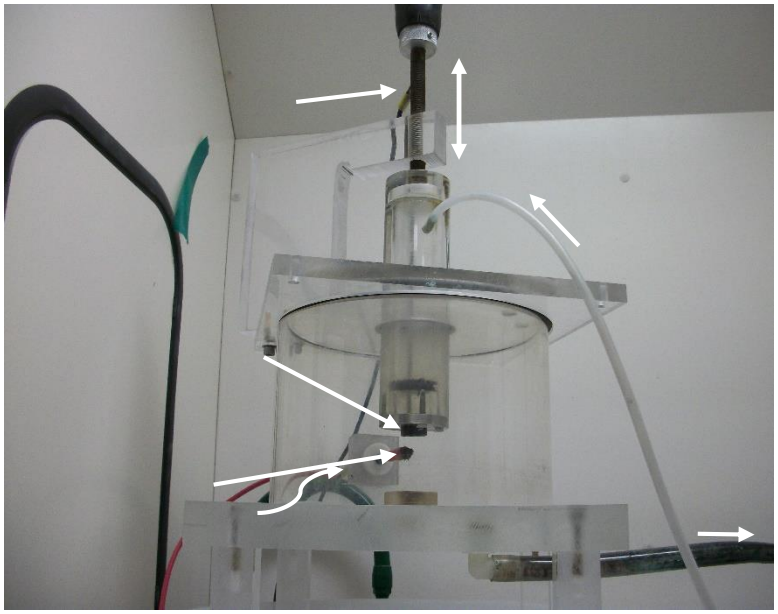

Figure 3-1. SaNEL EPP chamber.

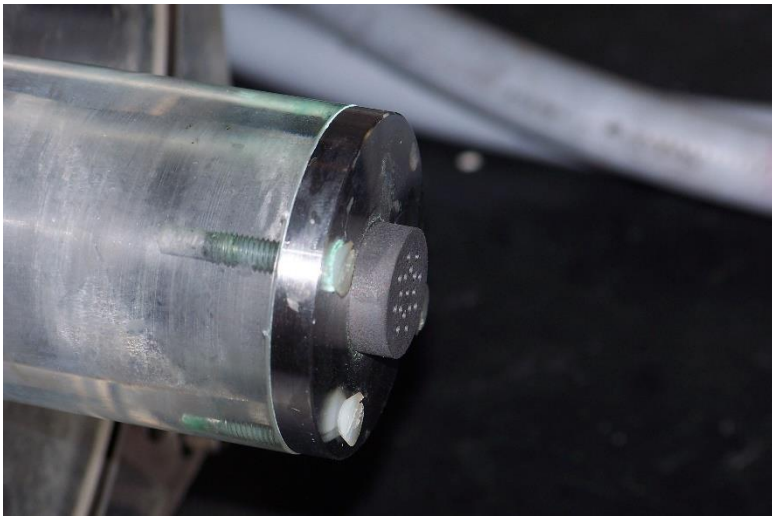

Figure 3-2. Replaceable graphite anode and stainless steel anode receiver.

For deposition of Ni onto Fe substrates a voltage of 200 V was used which resulted in a typical current density of 3.0-3.5 A/cm^2. Depositions were conducted at times of 10 s, 20 s, and 30 s in order to determine the changes in coating thickness, uniformity, and coverage with respect to deposition time. All EPP Ni depositions on Fe were conducted with an electrolyte of 20% $NiSO_4$, at a flow rate of ~2 L/min, and an anode-cathode separation distance of 5 mm. The electrolyte was held at a temperature of ~75° C, which resulted in a conductivity of 44 mS/cm and a pH of ~3.8.

Depositions of Ni via EPP onto Al substrates were conducted with the same electrolyte used in the Fe substrate depositions: 20% $NiSO_4$, temperature of 75° C, pH of ~3.8, and a conductivity of ~44 mS/cm. The flow rate and anode-cathode separation distance were also the same values, 2 L/min and 5 mm, respectively. Voltages used for the deposition of Ni onto Al differed from those used to deposit onto Fe, with voltages of 185 V and 210 V used. The resultant current densities for these conditions were 3.0-3.5 A/cm^2 for both instances, although the total current did increase slightly at longer deposition times. Depositions were carried out at 185 V for times of 30 s, 60 s, and 90 s and a separate group of depositions were conducted with an initial 210 V step for 30 s followed by processing at 185 V for either 30 s, 60 s, or 90 s. The different deposition times were conducted in order to determine the changes in the coating characteristics, coverage, thickness, and uniformity with respect to time and the addition of the 210 V step for 30 s was added in order to determine the effect of a non-continuous intermetallic interlayer which was observed to form at this condition.

3.3 Characterization Methods

Several methods were used in order to fully characterize the cleaned surfaces and deposited coatings. Surface morphology was examined by Scanning Electron Microscopy (SEM) and optical profilometry. Energy Dispersive X-Ray Spectroscopy (EDS), both as an area scan from the surface and as a line scan in cross-section was utilized to determine the elemental composition of the coatings. X-Ray Diffraction Spectroscopy (XRD) was used in order to determine the crystalline phases present in the coatings as well as to estimate the grain size of the coatings through the use of the Scherrer equation. Transmission Electron Microscopy (TEM) was utilized in order to more accurately determine the grain size of the coatings through direct measurement. Determination of the mechanical properties of the coatings was obtained through Vickers micro-hardness testing, tribological wear experiments, in the form of pin-on-disk experiments, and pull-off adhesion measurements. Final characterization of the deposited Ni coatings involved measurements of the corrosion resistance through anodic polarization and open-circuit potential (OCP) vs. time. The combination of these several characterization methods is expected to result in a detailed understanding of the microstructure of the material and its properties.

3.3.1 SEM/EDS

Surface Morphology was observed using a Hitachi S3000N SEM. All images were obtained using an accelerating voltage of 20 keV and a typical working distance of 15 mm. Observations were made as to the apparent surface quality of the coatings, including the surface coverage and the surface texture. Additionally, samples were cross-

sectioned and SEM was used to determine the surface coverage and to measure the average coating thickness in order to calculate the average deposition rate. EDS measurements, both surface and cross-sectional line analysis were conducted with an attached EDS manufactured by EDAX.

3.3.2 TEM

Direct measurement of the grain size was conducted by a JEOL 1200EX STEM using an accelerating voltage of 120 keV and capable of a point resolution of 0.34 nm. Initial processing of the samples involved removal of a large portion of the substrate in order to more easily work with the surface section. In the case of the sample containing an Fe substrate it was necessary to insure that the majority of the Fe substrate was removed due to magnetic effects on the electron beam. All samples were then subjected to mechanical dimple grinding and subsequent ion milling only from the substrate side performed by a Gatan Model 691 Precision Ion Polishing System.

3.3.3 Optical Profilometry

Optical profilometry measurements were used in order to determine the surface roughness of cleaned and coated samples and to determine the wear scar cross-sectional area for tribological testing. A Veeco NT9100 Optical Surface Profilometer was used. All roughness and wear scar data was collected using a 5X objective lens which resulted in a scan windown of 1.3mm x 0.95 mm. While several roughness parameters exist for surface characterization only the R_a values were used for the present study due

to its wide spread usage. R_a represents the arithmetic mean of all surface heights in the sample, presented in Equation 3-1.

Equation 3-1. Equation for calculating surface roughness, R_a.

$$R_a = \frac{1}{n}\sum_{i=1}^{n}|y_i|$$

3.3.4 XRD

X-Ray diffraction was carried out using a Bruker D-8 Advance X-Ray Difractometer. Emitting radiation was from a Cu Kα source with a wavelength of 1.54 Å with an accelerating voltage of 40 kV and an accelerating current of 40 mA. A step size of 0.025 degrees was used in order to insure high precision and a dwell time of 2 seconds was used in order to ensure a more accurate scan value. XRD scan were performed in θ-2θ mode and in low angle mode in order to determine the crystalline phases present in the coating. In addition to determining the crystalline phases, XRD was also used to estimate the grain size in the coatings through the use of the Scherrer equation, shown in Equation 3-2, in which τ represents the grain size of the material, K represents the dimensionless grain size shape factor, λ the wavelength of the incident radiation, β represents the full width half maximum (FWHM) of the peak, and θ is the Bragg angle of the peak being analyzed.

Equation 3-2. Scherrer equation for estimating grain size.

$$\tau = \frac{K\lambda}{\beta \cos\theta}$$

3.3.5 Microhardness

Microhardness measurements were conducted with a LM 300AT microindenter using a Vickers tip and a loading force ranging from 10 g_f up to 250 g_f. The hardness values were converted from H_v values to GPa through the relationships shown in Equation 3-3.

Equation 3-3. Equation for converting from Vickers hardness (H_v) to GPa.

$$H_v = 0.009807\ GPa$$

3.3.6 Wear

A pin-on-disc tribometer (CSM Instruments) was used to make measurements of the wear properties of EPP deposited Ni coatings on Al. All wear experiments were conducted with a 6 mm alumina ball at a wear track radius of 3 mm. A linear speed of 5 m/s (159 rpm) at a distance of 1000 m (53,000 revolutions) and a 2 N load was used for all experiments. The coefficient of friction was measured continuously with respect to time. The wear track morphology and the cross-sectional wear area were calculated with the aid of an optical profilometer. Optical profilometer scans were taken at four separate locations on the wear track and three measurements were conducted on each scan in order to determine an average area for the individual scan. These values were then used to create an overall average for the wear track. The 2-D cross sectional area was then multiplied by the wear track circumference in order to determine the wear volume,

presented in Equation 3-4, where ẇ is the wear rate, V represents the worn volume loss, L is applied normal force, and d is the total sliding distance.

Equation 3-4. Equation for calculating the wear rate of worn samples.

$$\dot{w} = \frac{V}{L * d}$$

3.3.7 Adhesion

Determination of the adhesion of the coatings to the substrates was performed by conducting vertical stud pull adhesion tests. Adhesion studs were manufactured by Quad Group and had a fracture strength of 70 MPa (~10,000 psi). In the process of vertical stud pull adhesion tests either the bonded epoxy breaks first, indicating that the coating adhesion is above 70 MPa, or the coating pulls off from the substrate, in which case the coating adhesion is wear than 70 MPa. Both of these instances are easy to observe on the stud after it has been pulled from the sample surface. Vertical pulling and measurement was conducted with an electromechanical tensile machine manufactured by Instron (Model 4202) with a custom made grip. Sample preparation was conducted by holding the sample along with a adhesion testing stud in a purpose designed holder and then placing into an oven held at 150° C for 1 hour. Samples were then removed and allowed to cool in air. After the samples were carefully loaded into the custom made grip, being sure to align the specimen vertically so as to apply pure tensile stress and avoid any shear stress as much as possible, a constant pulling rate of 1 mm/min was applied. Load vs distance results were recorded.

3.3.8 Corrosion

Open-circuit potential vs. time and anodic polarization measurements were made using a EG &G Corrosion Measurement System Model 273. All experiments were conducted in 3.5% NaCl aqueous electrolyte with a measured pH of 5.5. Samples were mounted in an epoxy resin with only the treated surface exposed. Measurements of the OCP value were conducted in open air using a Saturated Calomel Electrode (SCE) as reference and were conducted over a time length of 10,000 s with measurements taken every 10 s. Anodic polarization measurements were conducted in a de-aerated environment by bubbling Ar gas for 25 min, and graphite counter electrodes were utilized. Anodic polarization scans were begun 200 mV below the OCP and were continued up to 800 mV above the OCP, intentionally resulting in the corrosion progressing into the dissolution regime. SEM observations were conducted following corrosion testing in order to observe the resiliency of the coatings to corrosion in Cl^- containing environments and to determine the overall corrosion resistance of the coatings.

Chapter 4

Effect of Process Variations on Surface Morphology and Current Density of EPP Cleaning on 1018 Steel

4.1 Introduction

Initial experiments were performed in order to determine the optimum setting for EPP cleaning which could then be transferred to EPP deposition and to explore the capability of the process. Specifically, there was interest in how the V-I curves varied with changing anode-cathode separation distance and electrolyte concentration with the goal being to find the parameters which resulted in the lowest processing current while producing the highest surface quality.

All samples were polished down to 600 grit SiC paper as the last step and were dried with compressed air. The electrolyte consisted of $NaHCO_3$ at a concentration of 12 wt. % a flow rate of 2 L/min was used, and the anode-cathode separation distance was set to 5 mm. For determining the effect of separation distance, spacings of 3, 4, 5, 7.5, and 10 mm were chosen. When varying the concentration of the electrolyte, concentrations of 8, 10, and 12 wt. % were selected, and flow rate variations were 2, 0.8, 0.5, and 0.3 L/min.

4.2 Effect of Electrolyte Flow Rate

Initially, the effect of flow rate was examined, and it was determined that the lower flow rates resulted in a lower current across the V-I curve as well as an increase in the U_1 voltage. This is likely due to the increased flow rate acting to wash the hydrogen bubbles from the surface, thus requiring higher voltage to initiate and maintain a plasma.

Additionally, the current associated with the processing conditions was slightly lowered believed to be due to the presence of fewer plasma events occurring across the sample at any given time. This lower current, while beneficial, was once again hindered by the fact that the plasma quality was significantly reduced due to the lack of continuous coverage of the sample surface, resulting in much lower working of the sample surface. In this case, the slight increase in voltage and current is desirable to the lower working quality that results from lower flow rates. Comparative images of varying flow rates can be seen in Figure 4-1. Additional experiments were performed in which the flow rate was maintained constant while the flow velocity was increased. In this case, the voltages associated with each phase of the V-I diagram increased significantly demonstrating that there is an ideal velocity and quantity of electrolyte which will result in the best possible plasma.

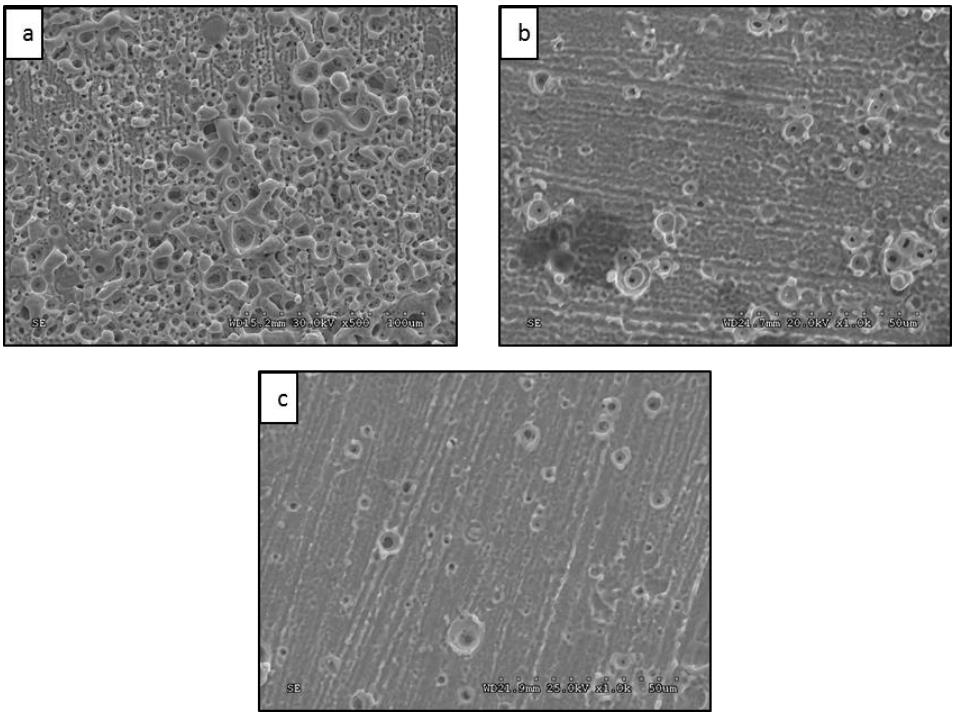

Figure 4-1. Effect of flow rate on the surface quality of EPP cleaned 1018 steel.

(a) 2 L/min, (b) 0.8 L/min, (c) 0.3 L/min.

4.3 Effect of Electrolyte Concentration

With 2 L/min mm determined to be the optimum flow rate, the concentration of the electrolyte was then varied. The results from this set of experiments indicated that as electrolyte concentration decreased the general shape of the V-I graph remains the same, but the curve was shifted slightly to a larger current value at all points. This would be expected as a less concentrated electrolyte would contain fewer conducting species and a greater current would be required to attain a critical charge density. Additionally, while the current increases in order to draw enough charge carriers to initiate a plasma, the quality of the plasma was reduced and the expected presence of micro-craters diminished significantly indicating a lesser working of the surface as can be seen in Figure 4-2. Additionally, experiments were also carried out when depositing Ni in which the $NiSO_4$ concentration was decreased. It was observed that small reductions of $NiSO_4$ concentration led to an unstable plasma and an inability to treat the samples, likely due to smaller number of charge carriers being present causing the plasma to cease. Experiments were then conducted in which the $NiSO_4$ concentration was reduced to 10% and the conductivity was increased by adding Na_2SO_4 (~20g/L). In this case a thick $NiFe_2O_4$ layer was created on the Fe samples.

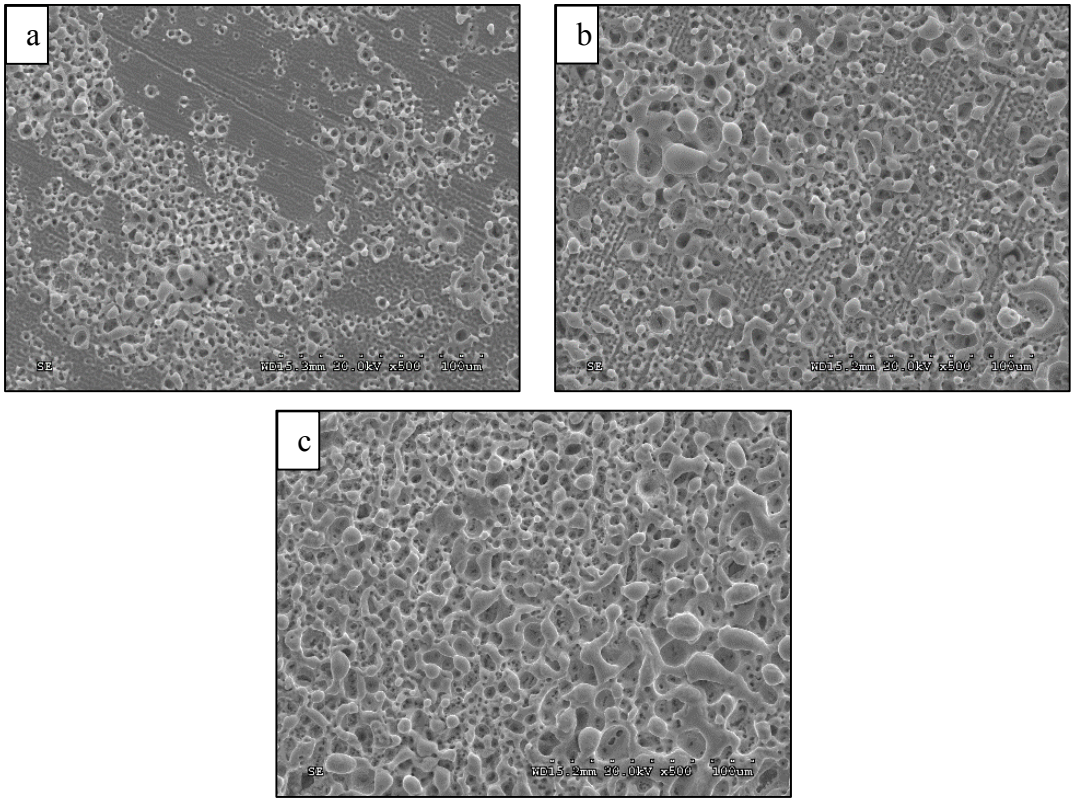

Figure 4-2. Effect of electrolyte concentration on EPP cleaning. (a) 8% $NaHCO_3$, (b) 10% $NaHCO_3$, (c) 12% $NaHCO_3$.

4.4 Effect of Anode-Cathode Separation Distance

Results from varying the anode-cathode separation distance showed that the peak associated with U_1, from Figure 2-3, is shifted to lower current and higher voltage while the operating condition associated with U_3 increases. Although the processing current is lowest at the lowest separation distance, the quality of the sample surface was greatly diminished due to the much increased presence of micro-arc discharges; present due to the decreased resistance between the anode and the cathode. The presence of

these discharges can be observed as the large craters present on the sample surfaces shown in Figure 4-3.

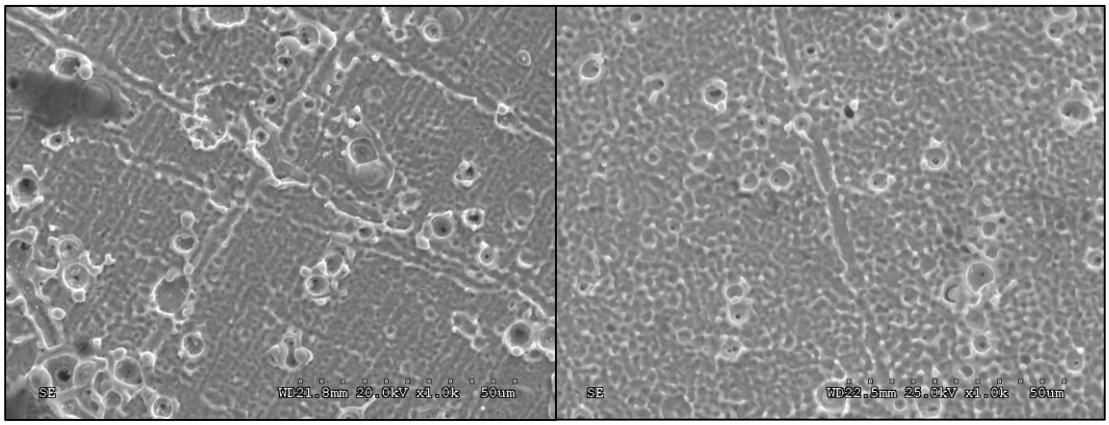

Figure 4-3. Effect of anode-cathode separation distance during EPP cleaning. (a) 3 mm, (b) 5 mm.

4.5 Effect of Voltage Controllability

While conducting experiments it became evident that an additional parameter was significant in attaining good quality surface coatings. This parameter, voltage controllability, is not commonly discussed. Initial experiments used an MDX 10K power supply manufactured by Advanced Energy. This power supply was shown to have poor performance with regards to maintaining a uniform voltage after the formation of the EPP plasma. Later depositions used a much newer Sorrensen SGA 600-17 power supply. A comparison of the two power supplies is presented in Figure 4-4. In the MDX power supply, the voltage is set to be maintained at 200 V, but, as can be seen, the actual voltage varies from 0-400 V (which is the highest value recordable by the oscilloscope in use which suggests that the actual voltage is likely even higher). This leads to very high

rates of arcing and a high level of coating damage and degradation of overall quality. It should be noted that due to these issues, it was not possible to obtain useable coatings on either Fe or Al substrates. The SGA 600-17 power supply shows both the voltage and current vs. time and it can be seen that the voltage, set to be maintained at 185 V, varies only slightly from the set point. This leads to much lower arcing and much higher overall coating quality.

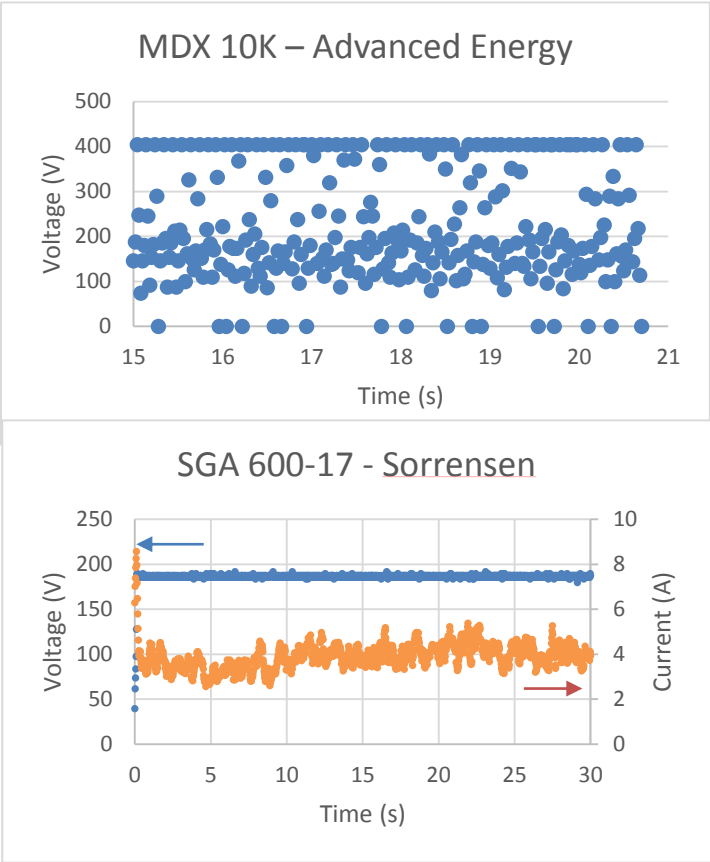

Figure 4-4. Voltage vs. time diagram for MDX 10K power supply (top) and voltage and current vs. time diagram for SGA 600-17 power supply (bottom).

4.6 Characterization of EPP Cleaned 1018 Steel

Using the above determined parameters, a full range V-I curve was attained and is presented below in Figure 4-5. As can be seen, the experimentally attained V-I curve matches well with the V-I curve presented earlier in Figure 2-3. The rapid increase in current occurring beyond ~175 V represents the onset of the sparking regime, U_4. EPP cleaning was conducted on 1018 low carbon steel substrates at 170 V, 12 % $NaHCO_3$, for a duration of 30 s. An SEM micrograph of the developed surface is presented below in Figure 4-6. The morphology duplicates that which is described in literature as either “hills and valleys” or as “spheroids and microcraters.” This morphology is a direct result of the localized melting and freezing events which occur at the surface due to hydrogen plasma heating and subsequent quenching by the electrolyte. Using optical profilometry, the Ra value of the cleaned surface was determined to be 1.412 μm averaged over 10 separate measurements with a low roughness value of 1.09 μm and a high of 1.99 μm. Surface EDS measurements taken of the cleaned surface were not able to detect the presence of O to any significant extent, showing that the hydrogen plasma generated by EPP is highly effective at the removal of surface oxides and contaminants.

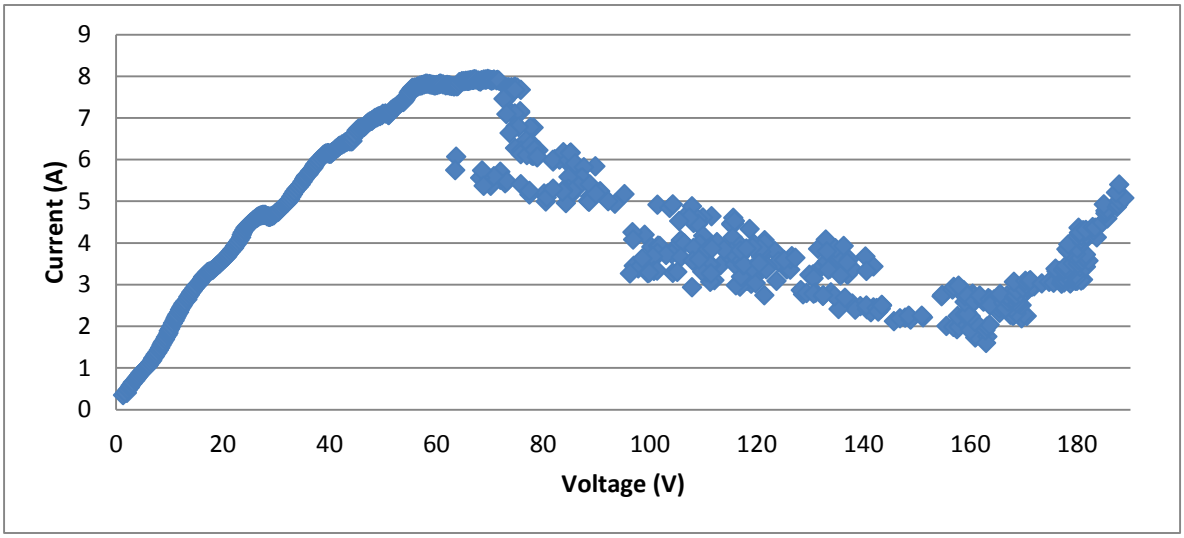

Figure 4-5. Voltage vs. current plot of EPP cleaning process utilizing the experimentally determined parameters.

4.7 Discussion

From these sets of experiments it was determined that the optimum separation distance is 5 mm, with lower separation distances leading to increased micro-arcing. Also, the flow rate was shown to have a greater effect than was expected and the best results were obtained when the maximum amount of electrolyte exposed to the sample surface was 2 L/min. However, separate experiments also revealed that increasing the velocity of the electrolyte further resulted in an increase in the required voltage, in effect stretching the V-I curve to higher voltages due to the higher velocity acting to wash the hydrogen bubbles from the sample surface. The final parameter analyzed, electrolyte concentration, demonstrated that decreasing the concentration leads to increasing current and decreasing surface working due to a lack of conducting ions. Experiments with deposition parameters also led to the realization of the importance of voltage

controllability, which proved to have an unexpectedly large effect on the quality of the coatings. It was determined that better controllability led to lower arcing rates which decreased coating damage during deposition. EPP cleaning of a Fe substrate was then conducted using these parameters with results showing a typical “hills and valleys” morphology typically reported for this process. Additionally, the surface was shown to possess very low O content, indicating the highly performance of this process to remove O.

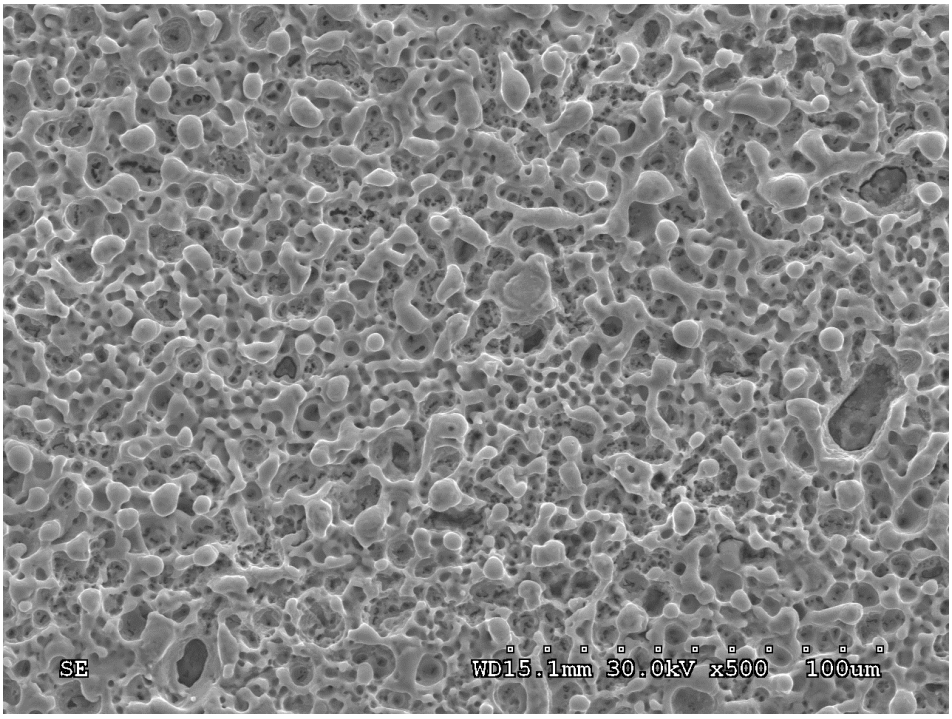

Figure 4-6. Surface SEM micrograph of EPP cleaned Fe sample.

Chapter 5

EPP Deposition and Characterization of Ni Coating on Fe

5.1 Introduction

Deposition of Ni via EPP onto Fe substrates was conducted in order to determine the effectiveness of EPP as a Ni coating technology. A full description of the processing parameters is given in Chapter 3. The following chapter contains a brief summary of the deposition parameters for clarity as well as results and discussion on the surface morphology, deposition rate, coating composition, and corrosion properties of the EPP Ni coating on Fe substrate.

5.2 Deposition

Deposition of Ni onto the Fe substrates was conducted utilizing the knowledge gained through the experiments described in the preceding section. A deposition voltage of 200V was utilized with an anode-cathode separation distance of 5 mm and an electrolyte flow rate of 2 L/min. The electrolyte used consisted of 20% $NiSO_4$ in deionized water. The electrolyte was heated to approximately 75 °C which resulted in a conductivity of ~44 mS/cm and a pH of ~3.8. For reference a complete scan of the V-I data was conducted beginning at 40 V and ending at 250 V. This was conducted in order to determine any differences in the V-I behavior owing to the use of different electrolyte composition. This data is presented in Figure 5-1. As can be observed, the overall shape of the V-I plot differs from that shown previously in Figures 2-3 and 4-5. At this time, this

difference is believed to be caused by the presence of Ni electrodeposition occurring in tandem with hydrogen gas evolution. The onset of the sparking regime can be observed to occur after approximately 210 V.

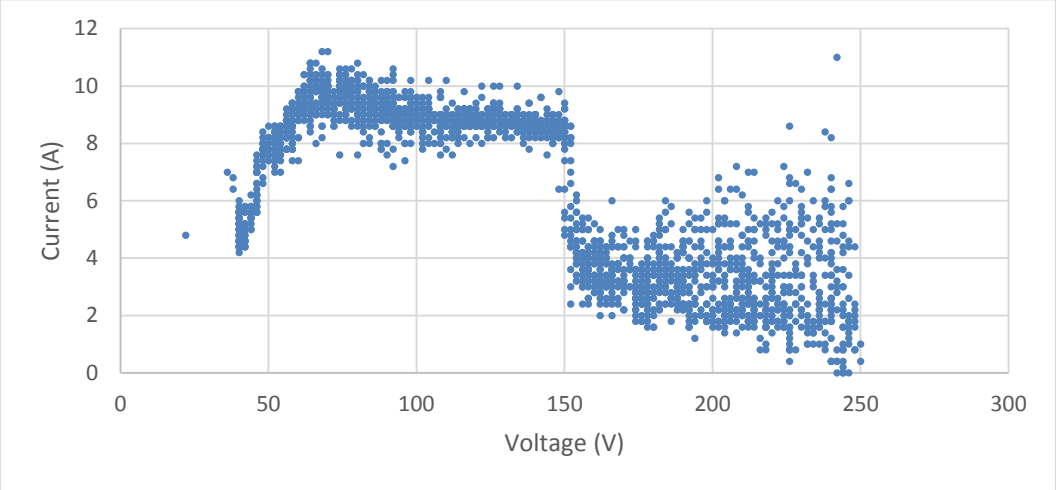

Figure 5-1. Voltage vs. current plot of Ni deposition on Fe (40 V - 250 V).

Depositions were carried out over a range of times and the resulting coatings were then analyzed. Surface SEM images, shown in Figure 5-2, detail the coating surface morphology. As can be seen, the surface consists of protruding nodules and the presence of small valleys. While this is similar to the typical “hills and valleys” attributed to the cleaning process the difference is noticeable and is likely attributed to the differing plasma properties of the two systems resulting from dissimilar electrolytes.

The samples were then cross-sectioned, mounted, polished and etched with Nital in order to study the coating-substrate interface and to determine the coating thickness and uniformity. Figure 5-3 shows a representative cross section of a Ni coating on Fe substrate. As can be seen, the coating is continuous across the surface and contains a high degree of variation in coating thickness. The average coating thickness was

determined for depositions of 10 s, 20 s, and 30 s and a deposition rate was determined as can be seen in Figure 5-4, the coating growth rate is highly linear, and was determined to be ~165 nm/s. Typical coating growth through most coating techniques follows a $t^{1/2}$ relationship which is due to the growth of the coating through diffusion. The fact that the EPP coating growth rate is shown to be linear indicates that coating growth is not slowed by diffusion mechanisms and is instead due to transport of the ions to the surface through hydrogen bubble. This leads to much faster increase in the overall coating thickness than what can be achieved in similar time frames with traditional coating techniques.

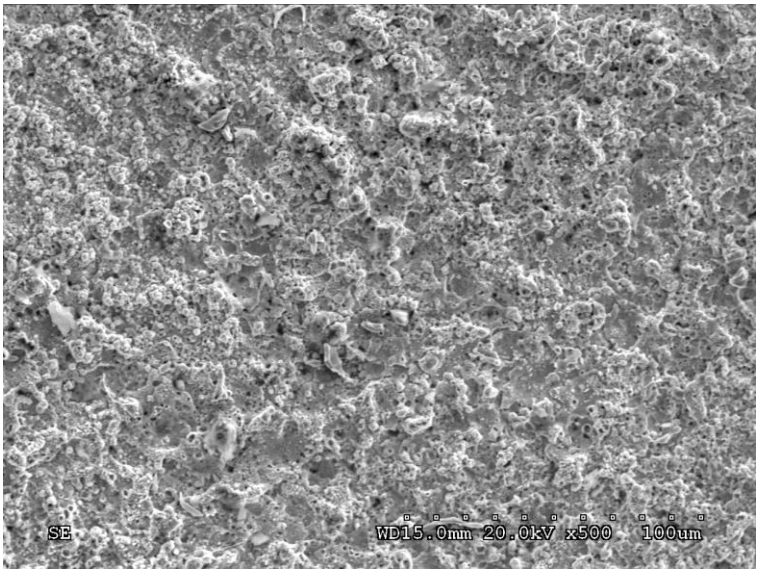

Figure 5-2. Surface SEM micrograph of EPP deposited Ni on Fe for 30 s at 200 V.

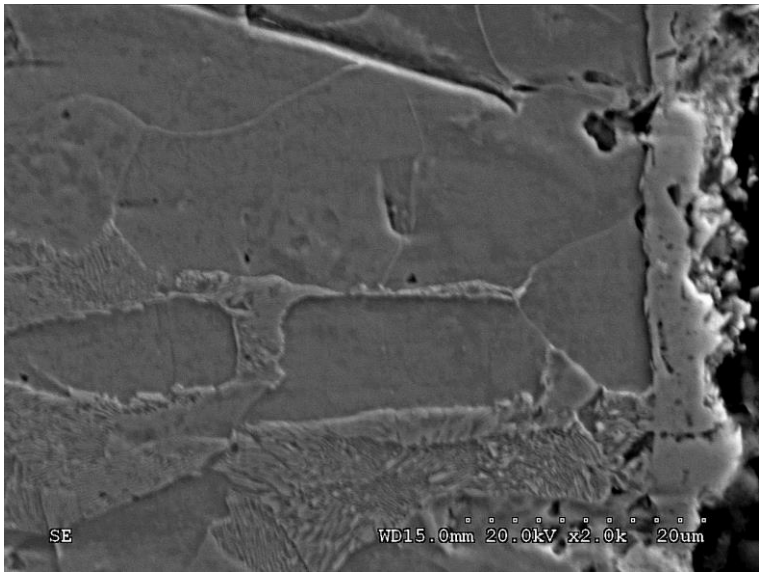

Figure 5-3. Cross-sectional SEM micrograph of EPP deposited Ni on Fe for 30 s at 200 V. Note that the voids present are caused by the nital etching process.

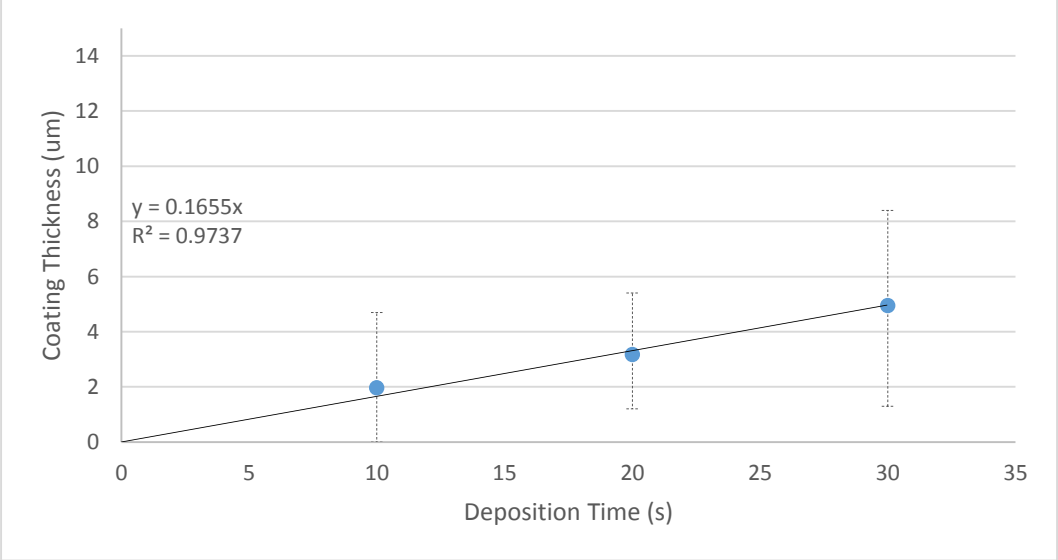

Figure 5-4. Deposition rate for EPP deposited Ni on Fe.

5.3 Characterization

Initial characterization of the Ni-deposited samples consisted of low-angle XRD examination. Figure 5-5presents a typical XRD pattern from an EPP Ni coating showing the presence of broad diffraction peaks consistent with a fcc Ni crystal structure. The (111) and (200) 2-θ diffraction angles were found to be 44.46° and 51.62°, respectively. These values are close enough to the expected (111) peak of 44.34° and the (200) peak of 51.67° that they can be assumed to be pure Ni. Additionally, the grain size of the Ni coating was estimated using Eq. 3-2 A grain size of about 92 nm was estimated, indicating the presence of a nanoscale Ni coating. Indeed, in view of the melting and quenching events prevailing during deposition, the presence of a fine grain structure is anticipated. Finally, the relative peak intensities match up well with what is expected for a randomly crystal orientation indicating that the structure does not contain any preferred orientation or texturing.

Direct measurement of the grain size of the coating was conducted via TEM and these results are shown in Figure 5-6. As can be seen from the dark field image, grain size varies from about 20 nm up to about 40 nm. Slightly smaller than the value estimated via the Scherrer equation. The measured grain size of the coating clearly demonstrates the nano-crystalinity of the EPP Ni coating.

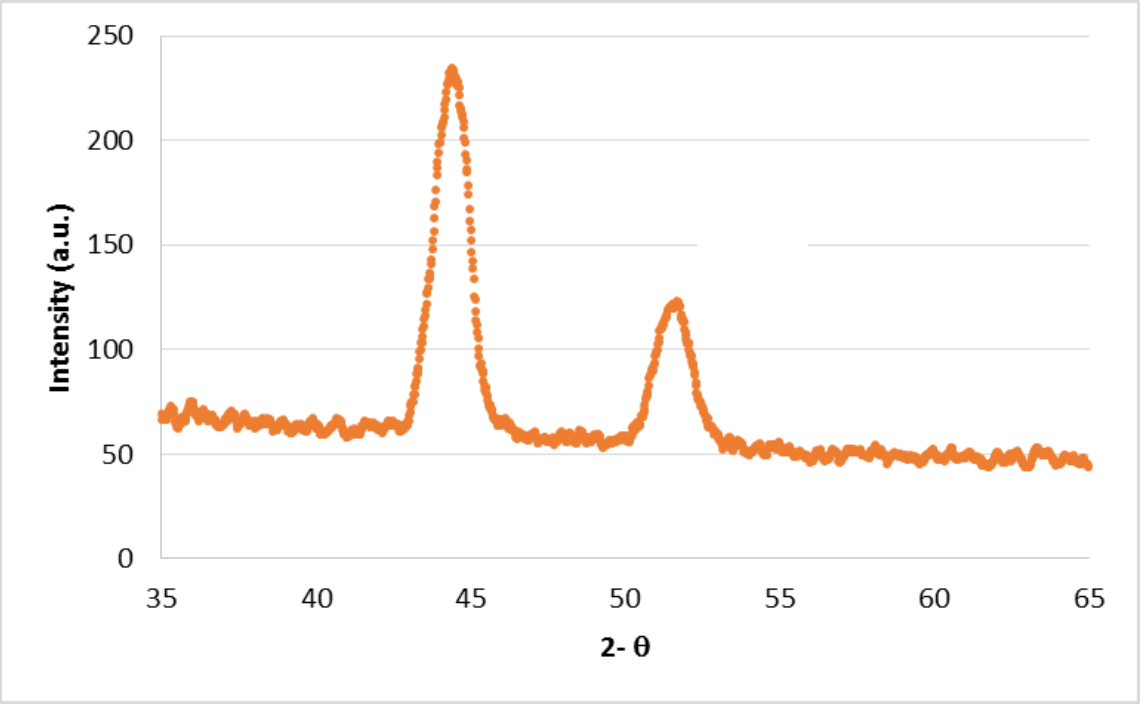

Figure 5-5. XRD spectra showing Ni (111) and (200) peaks deposited on Fe substrates.

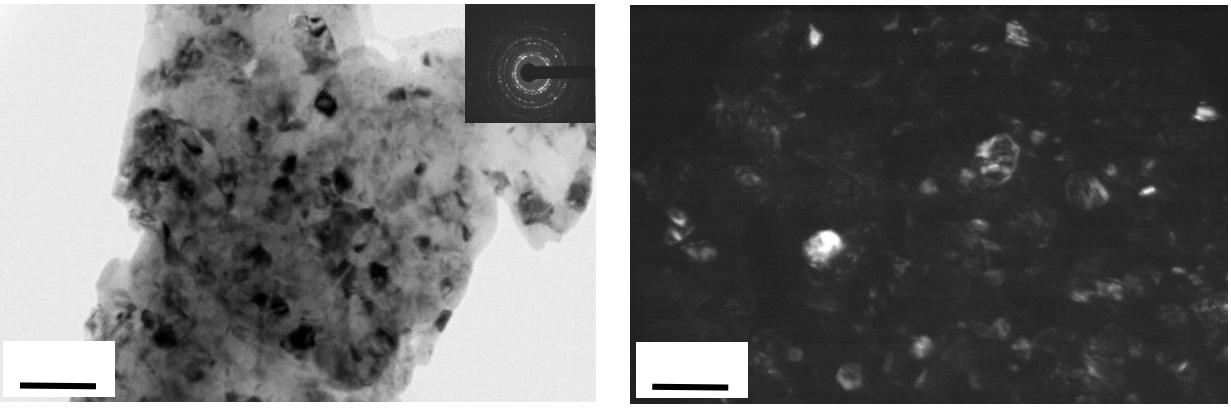

Figure 5-6. Plan view TEM micrographs: bright field (a) and dark field (b) of EPP deposited Ni on Fe.

Surface and cross-sectional SEM examinations were conducted to determine the effect of deposition time on the thickness, microstructure and coating uniformity. Figure 5-7 presents SEM micrographs of the surface and cross section of all three samples coated for 10 s, 20 s, and 30 s. As can be seen, the Ni coverage of the Fe substrate is not complete in the 10 s deposition and small areas can be observed in which the underlying substrate is clearly visible. However, as the deposition time increases, the prevalence of these regions decreases until, in the case of the 30 s deposition, they have largely disappeared. The surface morphologies of the three samples appear very similar, indicating that the quenching followed by the plasma bubble collapse is able to remove sufficient excess heat so as to allow each bubble growth and collapse event to take place under similar circumstances. The cross-sectional profiles show an increasing coating thickness with increasing deposition time. Additionally, the coating showed a uniform hardness through the substrate with a slight decrease in the hardness through the Ni coating, suggesting that the Ni coating is slightly softer than the Fe substrate. However, no noticeable softening in the substrate was observed indicating that the no noticeable decarburization occurred during the plasma processing, and a uniform hardness was observed through the coating suggesting that the coating did not contain any unobserved porosity.

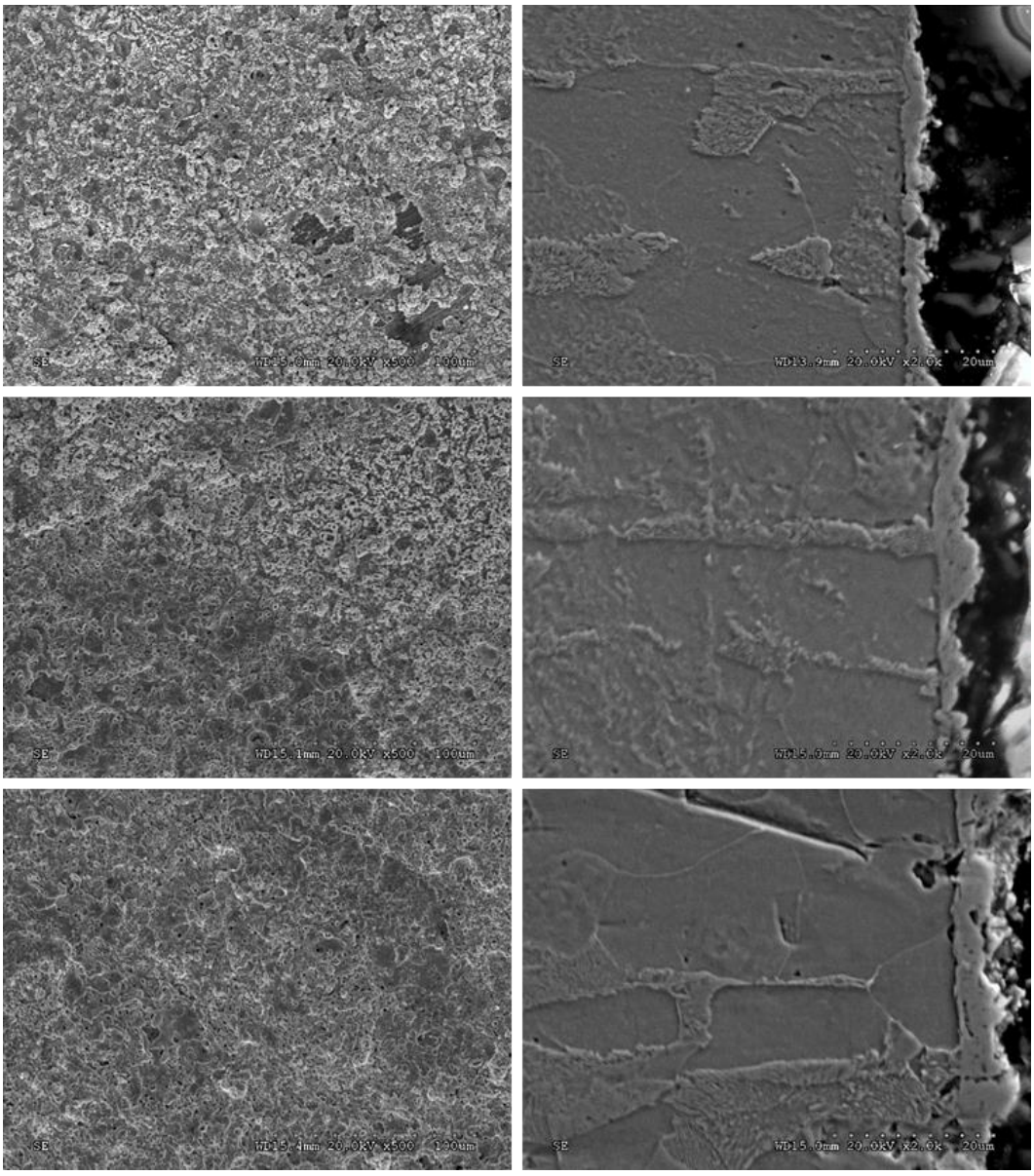

Figure 5-7. Surface and cross-sectional SEM micrographs of EPP deposited Ni on Fe at 10 s (a, b), 20 s (c, d), and 30 s (e, f).

5.4 Elemental Composition of Ni Coatings on Fe

Elemental composition both from the surface and cross-sections of the coatings was determined via EDS. Results are presented in Figure 5-8 and Table 5-1. Surface EDS results show the presence of Ni and Fe with a small presence of O. It is believed that the O is due to surface oxidation present after EPP processing. The presence of Fe can be due to either the penetration of the electron beam excitation volume penetrating into the substrate or due to some small amount of Fe being lifted into the Ni coating from the melting and mechanical working of the surface during the EPP process. For the 10 s deposition the low Ni and higher Fe content is due to the low coating thickness as well as the presence of gaps in the coating which results in the exposure of the Fe substrate. The Fe seen in longer deposition times, 20 s and 30 s, in the surface EDS is likely due to penetration of the electron beam through the Ni coating. It is important to observe that the O content is very low and decreases as the processing time is increased. This demonstrates the ability of the hydrogen plasma to remove any O present by reduction and the ability to clean the sample surface while deposition occurs. It should also be noted that the EDS spectra acquisition was taken after sample exposure to air, likely a source of the small amount of O present. Cross-sectional EDS is needed in order to determine the source of the Fe signal seen in surface EDS. Figure 5-9 shows a typical cross sectional EDS spectra for a 200 V deposition for 20 s. Cross sectional results showed a 100% Ni coating with a minimal transition zone. It should be noted that measurement of the transition zone from this EDS data is not an accurate determination

due to the fact that the transition zone width is within the distance enclosed by the excitation volume of the electron beam. Additionally, further proof of the ability of EPP to simultaneously clean and coat can be seen in the nearly constant O content from the substrate through the interface and through the coating.

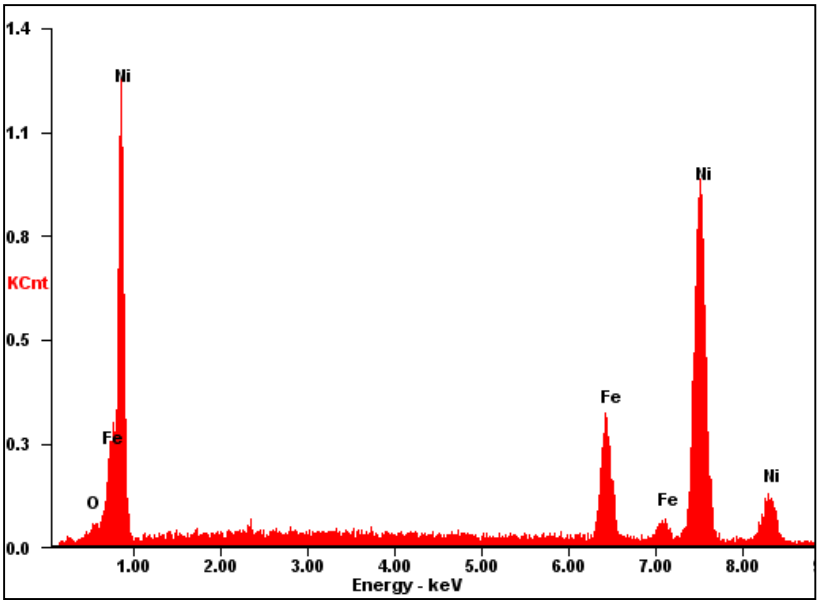

Figure 5-8. Surface EDS spectra of EPP deposited Ni on Fe for 30 s at 200 V.

Table 5-1. Elemental composition of Ni coating on Fe as determined by EDS. Note that the Fe present is due to excitation volume extending into the substrate.

	% at. Composition		
Sample	**O**	**Fe**	**Ni**
10 s	9.0 %	34.3 %	56.7 %
20 s	5.3 %	15.9 %	78.8 %
30 s	5.6 %	11.0 %	83.4 %

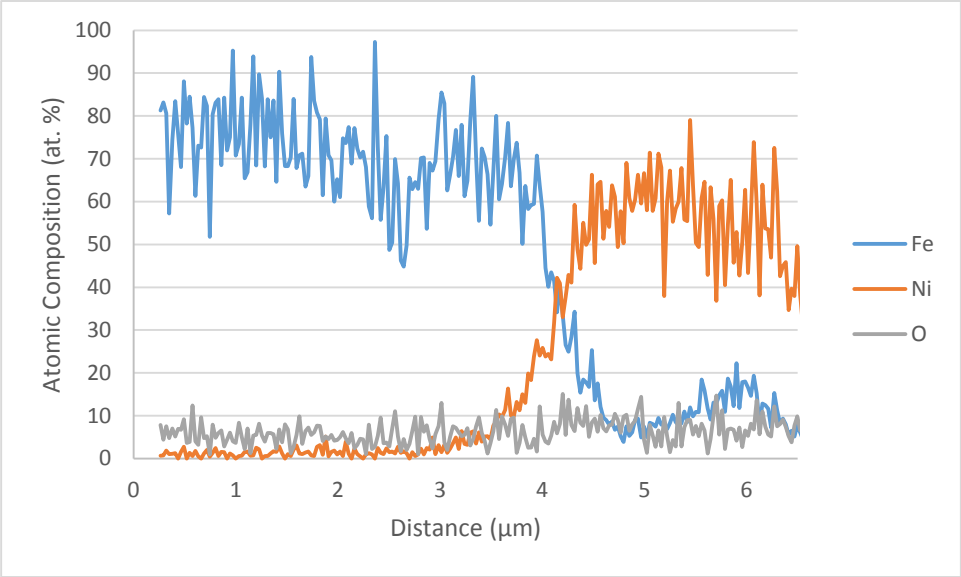

Figure 5-9. Cross-sectional EDS profile of EPP deposited Ni on Fe for 30 s at 200 V.

5.5 Corrosion Resistance of EPP Deposited Ni Coatings on Fe

The OCP values in open air for EPP Ni depositions along with those for Fe and pure Ni are shown in Figure 5-10 and Table 5-2. It is evident that the OCP values for the EPP-coated Ni are between those of Fe and pure Ni with the OCP increasing, and approaching that of Ni, as the coating thickness increases. As expected, the results exhibited an increase in the OCP in relation to the underlying Fe substrate, although still lower than that of bulk Ni, with an increase in the EPP deposition time with the largest improvement coming from the 30 s EPP deposition. In the 10 s deposition, even though it exhibited a higher initial potential, it eventually approached that of Fe, likely due to the incomplete coverage of the coating. For the longer deposition times of 20 s and 30 s the

OCP can be observed to remain far more stable which indicates a much more robust coating than that present in the 20 s deposition. However, the OCP values remain lower than that present in Ni with the 30 s and 20 s sample resulting an OCPs ~370 mV and ~270 mV, respectively, below that of Ni. Some of this decrease in OCP is likely due to the nano-crystalline grain size of the coating. It is widely known that nano-crystallinity leads to a far larger number of grain boundaries and triple junctions which can greatly lower the corrosion potential of the material. Additional decrease in the OCP of the two coatings may be due to the presence of very small amounts of Fe being present in the Ni layer, although this is not supported by cross-sectional EDS data. A final possibility may be the presence of small micro-cracks present in the coating. These would result in the gradual exposure of substrate Fe to the NaCl solution as the electrolyte penetrates into the micro-cracks leading to a lower overall OCP. This is supported by the swift decrease in the 30 s deposition coating during the first few hundred seconds. While this may explain the observed behavior, the presence of these micro-cracks was not observed with SEM.

Table 5-2.Table 5 2. OCP values for Ni coated samples as well as Fe and Ni control samples

Sample	**Open-Circuit Potential**, mV (SCE)
Ni	-230
30 s	-498
20 s	-594
10 s	-719
Fe	-708

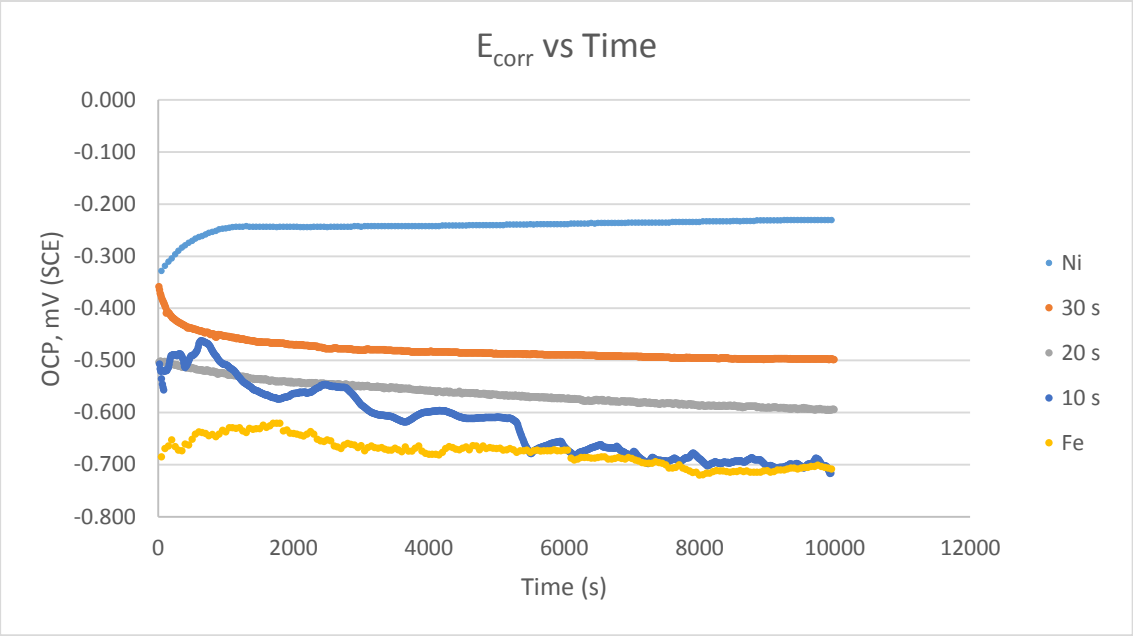

Figure 5-10. OCP vs. time for EPP deposited Ni on Fe conducted in 3.5% NaCl aqueous electrolyte.

Surface SEM images of the EPP Ni coated samples after being exposed to 3.5% NaCl electrolyte for 10,000 s can be seen in Figure 5-11. Some small signs of degradation can be seen on the surface when compared to the samples prior to NaCl solution exposure, but, overall, the samples remain in good condition and the coatings tend to endure the NaCl solutioin quite well. It should be noted that some iron oxide streaking was observable on the sample surfaces of the 10 s and 20 s deposition samples upon completion of the experiments. Surface EDS measurements of the 30 s sample revealed a slight increase in the Oxygen content (~1 at. %) from before and after the OCP measurements indicating the small increase in the surface oxide over the experiment duration. Further support for the high corrosion resistance of the coating can be viewed in Figure 5-12, which shows the cross section of the 30 s sample. The micrograph shown here represents a typical cross section and, as can be observed, no

coating damage can be seen. It should be noted that the sample was etched with Nital in order to distinguish the Fe substrate from the Ni coating and that the voids along the interface were not present prior to the application of the etching process.

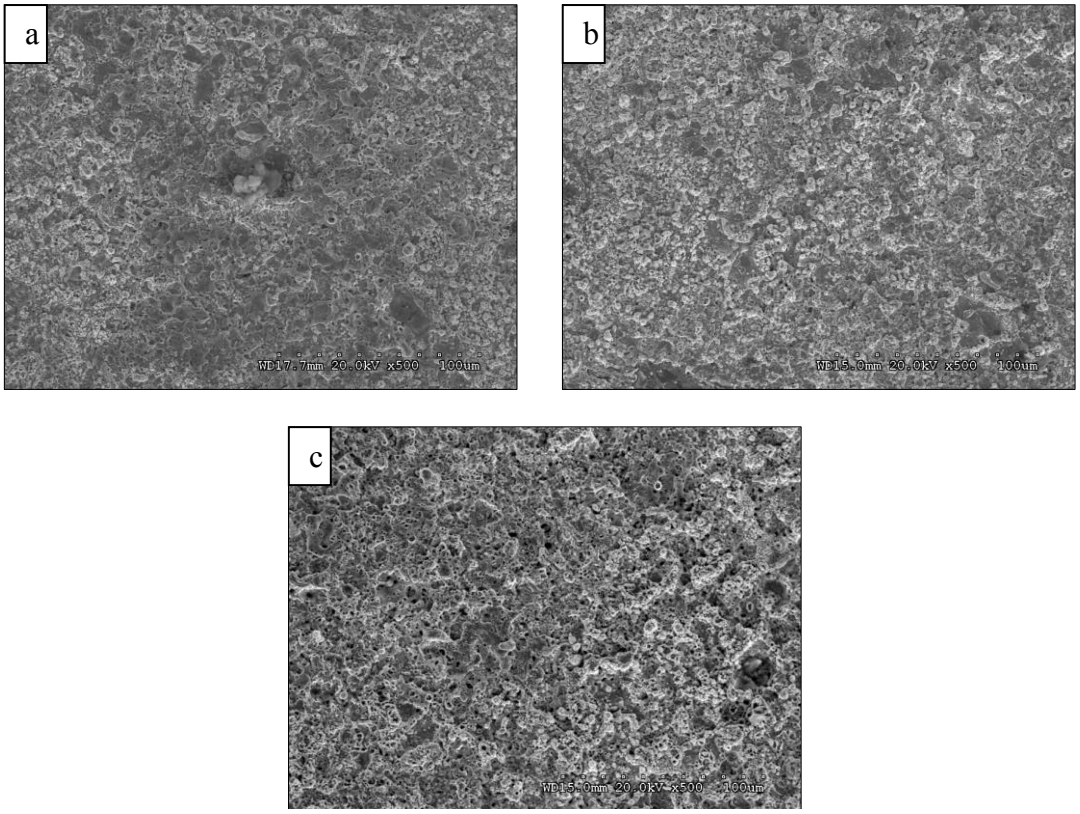

Figure 5-11. Surface SEM of 10 s EPP (a), 20 s EPP (b), and 30 s EPP (c) after exposure to 3.5% NaCl solution for 10,000 s.

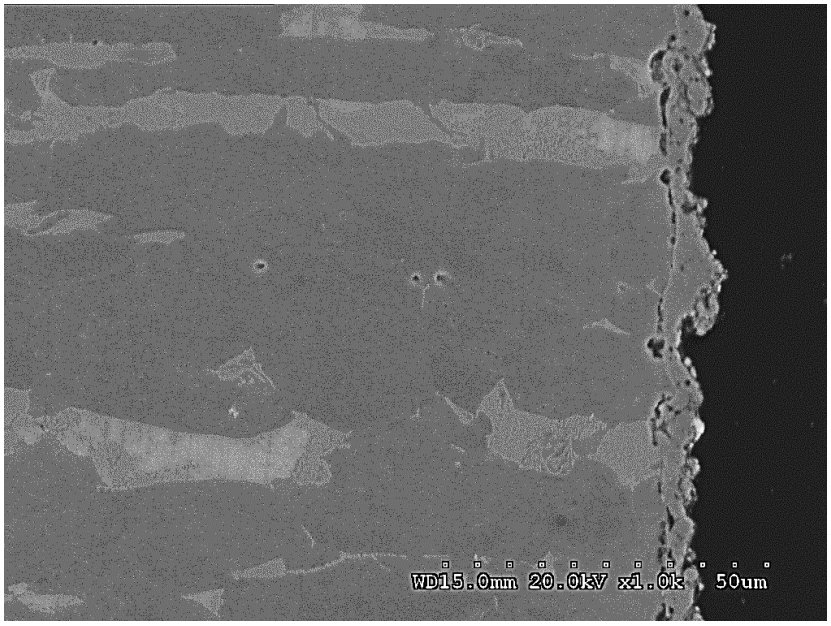

Figure 5-12. Cross-sectional SEM micrograph of 30 s EPP Ni on Fe after exposure to 3.5% NaCl for 10,000 s. Note: the voids at the interface are due to the nital etching process.

Figure 5-13 shows the results for the anodic polarization experiments of the EPP-coated Ni samples and the two baseline materials (Fe and Ni). Also, a summary of the corrosion potentials and corrosion rates calculated from these experiments is presented in Table 5-3. The results clearly show that the corrosion behavior of the three Ni coated samples lie between those of Fe and pure Ni. This behavior refers to the corrosion potential, anodic behavior and corrosion rate. The greatest improvement to the corrosion resistance was found with the greatest deposition time. While the lowest protection was provided by the 10 s deposition, showing a corrosion potential and corrosion rate of just slightly better than that of Fe. The 20 s deposition showed a larger improvement of slightly better than half-way between the two control samples. Finally, the largest

improvement was observed with the 30 s deposition in which an improvement of over 200 mV was seen. In addition, the corrosion rate decreased with increasing deposition time with the largest improvement, once again, coming from the 30 s deposition; an approximately 40% improvement was observed in this case. Similar to the results seen in the OCP experiments, the corrosion rate and corrosion potential of the samples remains below that of Ni. The lower corrosion potential can be attributed to the same causes as those explained earlier. The elevate corrosion rates when compared to Ni is likely due to the nano-crystallinity of the EPP Ni coatings. Examining the corrosion rates however, it is evident that the EPP Ni coatings all exhibit a lower corrosion rate than that of Fe and, if the high roughness of the sample is taken into account (which would result in a much higher actual surface area) it is evident that the corrosion rates are even lower than those presented.

Table 5-3. E_{corr} and I_{corr} values for Ni coated samples as well as Fe and Ni control samples.

Sample	**E_{corr}** (mV)	**I_{corr}** ($\mu A/cm^2$)
Ni	-595	0.28
30 s	-644	1.74
20 s	-693	2.00
10 s	-793	2.67
Fe	-849	2.77

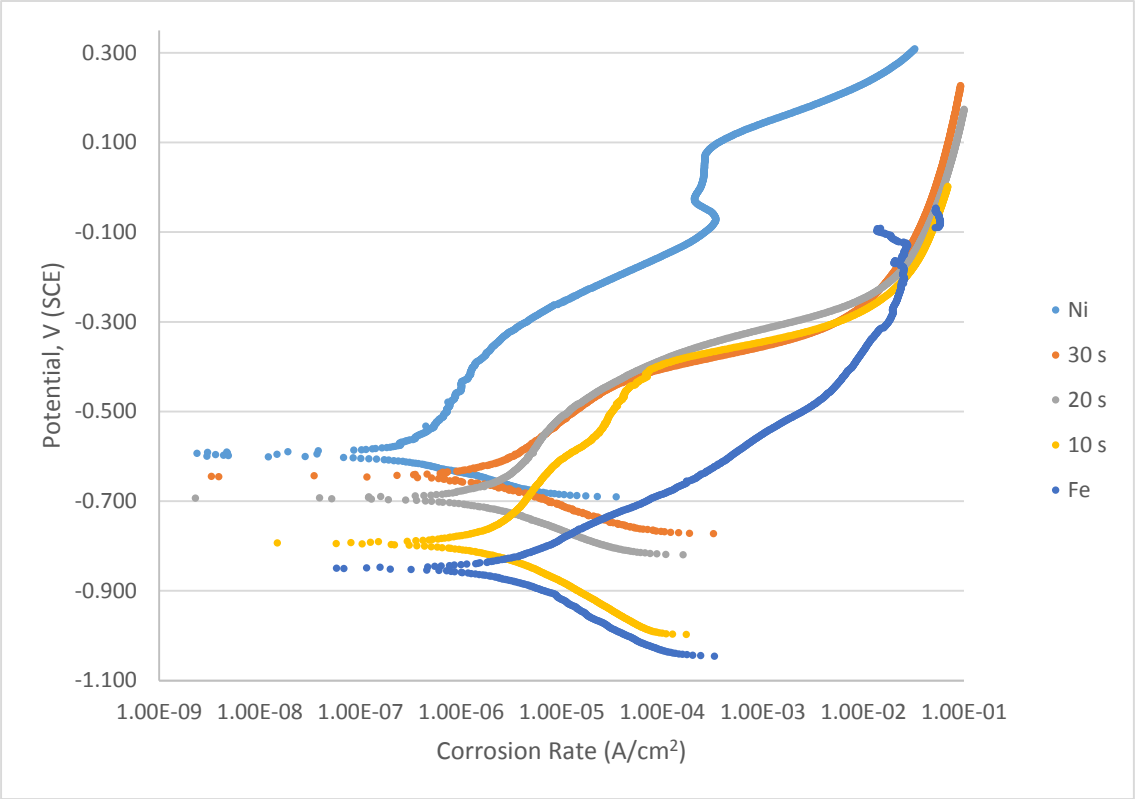

Figure 5-13. Anodic polarization plots for Ni coated samples as well as Fe and Ni control samples.

Results from the sample surface SEM examinations conducted after anodic polarization are shown in Figure 5-14 (a, c, e). The presence of pitting can be seen in all samples, but most noticeably in the 10 s deposition sample. In this case clear boundaries can be identified along which the pitting tends to occur. This is believed to be due to the deposition of Ni being preferred in certain areas leading to thinner coatings between these regions which allows for preferential pitting cites to develop. As the deposition time increases, it is believed that these areas accumulate enough Ni to allow them to resist pitting initiation in par with surrounding areas. Furthermore, in the 10 s deposition case, all observed pits extended into the Fe substrate whereas several pits in the higher

deposition time samples were observed to possess some Ni content at their base demonstrating that thicker coatings offer a prolonged corrosion protection. It should be noted however, that while the prevalence of pits decreases with an increase in deposition time, the depth and overall size of the pits does tend to increase. It is also important to note that during the anodic polarization experiments, the samples go through an extensive anodic dissolution process that is part of the test. The experiment advances by 800 mV above the corrosion potential into the activation polarization region causing intentional dissolution. The subsequent SEM observations are conducted to further explore the corrosion process under the imposed activation (anodic dissolution).

Figure 5-14 (b, d, f) shows SEM micrographs of cross sections after corrosion testing. It is evident that after the imposed anodic dissolution, pitting penetrated through the coating into the substrate. However, several areas where the Ni coating is still present can be observed. Due to the more negative corrosion potential of the substrate, pitting can be seen to spread along the substrate while the coating is far less affected.

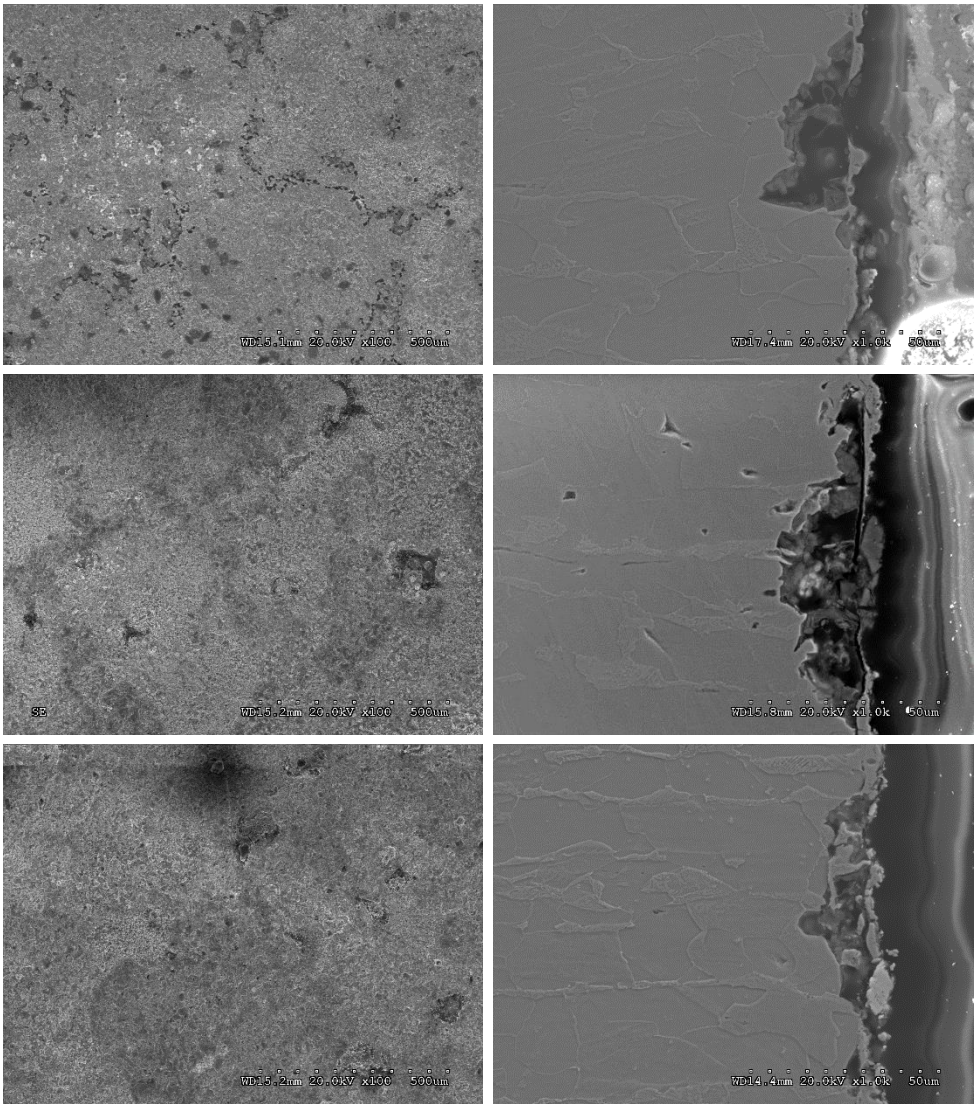

Figure 5-14. Surface and cross-sectional SEM micrographs of EPP Ni deposited on Fe for 10 s (a, b), 20 s (c, d), and 30 s (e, f) after anodic polarization measurements.

5.7 Discussion

Deposition of Ni onto Fe substrates was shown to result in a dense and continuous coating at deposition lengths of 20 s and greater. Grain size was estimated to be ~95 nm through use of XRD and was confirmed to be 20-40 nm via measurement with TEM. Through cross-sectional observation via SEM an extremely high deposition rate of ~165 nm/s was determined. This result indicates that the deposition process does not rely on diffusion of the ionic species but instead is a linear relationship which relies on the collapse of the plasma bubbles and the transport of the ionic species to the sample surface via the resulting shockwave. Corrosion results showed that increased coating thickness leads to increased corrosion resistance, but it was observed that the improvement in the corrosion resistance never reached that of commercially pure Ni. This is likely due to the nano-crystalline nature of the coatings as well as possibly due to the presence of micro-cracks which expose a small portion of the substrate to the electrolyte after the electrolyte has penetrated into the cracks. The coating found to be most resistant to corrosion was the 30 s deposition which exhibited a positive shift in the corrosion potential of ~200 mV and a ~37% decrease in the corrosion rate in comparison to the Fe substrate material.

Chapter 6

EPP Deposition and Characterization of Ni deposited on Al

6.1 Introduction

Utilizing the knowledge gathered in the preceding chapters, work was begun on the deposition of Ni via EPP on an aluminum substrate. It was assumed that the deposition parameters would easily transfer from one substrate to another, however this did not prove to be the case. It is believed that the low melting temperature of aluminum causes issues with the deposition of Ni that is not present in the higher melting temperature of Fe. In order to achieve deposition of Ni onto Al it was necessary to fully re-study the effect of voltage on the coating quality and composition when utilizing Al as the substrate material. Once the effect of voltage was ascertained, two processing conditions were chosen and characterization of these coatings was carried out. A more complete description of the deposition process is given in Chapter 3. The following sections include a brief description of the deposition parameters, presented for clarity, and characterization of the EPP Ni coatings. Characterizations included analysis of the surface morphology, coating composition, analysis of the mechanical properties of the coating, as well as the corrosion properties of the coating. Preliminary work was performed by determining the full range V-I data, which is presented below in Figure 6-1. The general shape of the plot is similar to that shown previously in Figure 5-1. Of note, is the later plasma onset, ~150 V when depositing on Fe and ~ 180 V when depositing on Al. This is likely due to differing plasma properties and hydrogen bubble formation occurring on the sample surface, either due to chemical effects, due to the different elements, or mechanical effects, due to the higher initial roughness attained of Al from polishing. Additionally, much higher variation is seen in the plasma current, when

compared to that of cleaning and Ni deposition on Fe, especially at voltages closer to plasma onset.

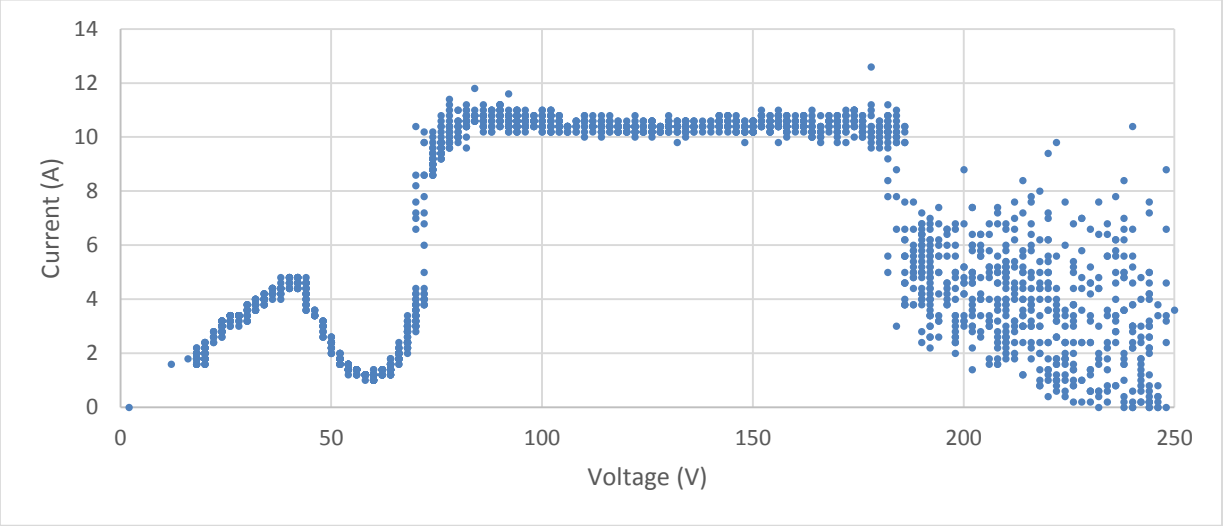

Figure 6-1. Voltage vs. current of Ni deposition on Al (18 V - 250 V).

6.2 Deposition

6.2.1 Effect of Voltage on Coating Quality and Composition

In attempting to deposit Ni onto aluminum two attributes were desired: the coating should be a continuous coating, and the coating should contain intermetallics due to their more advantageous properties. Of these two properties the quality of the coating itself was the most important, thereby giving higher priority to achieving a continuous coating. In order to begin to characterize the effect of voltage on deposition on a low melting temperature substrate a series of experiments was performed in which the voltage was increased (in increments of 5 V and beginning just above the plasma

voltage) for each deposition and a deposition of 60 s was allowed to occur. While it was desired for the initial experiment to be conducted at just above the plasma voltage (~180 V) the resulting plasma was unstable and the use of this deposition voltage was not deemed feasible. The results were then analyzed with SEM. The surface micrographs are given in Figure 6-2 (a-d), and the cross-sectional micrographs are presented in Figure 6-2 (e-h). As can be seen the quality of the coating is quite robust and dense, and has very good coverage in the initial 185 V deposition (Figure 6-2 a,e) and, although some defects in the coating are visible with 190 V (Figure 6-2 b,f), the coating still appears to cover the majority of the sample. However, increasing the voltage beyond this point to 195 V and 200 V (Figure 6-2 c,g and d,h respectively) shows a marked decrease in the coating quality to the point that, at 200 V, the coating is only slightly over 50% of the sample surface. Additionally, an overview of the surface morphology indicates the presence of large nodules covering the sample surface. The intensity of these nodules appears to increase with increasing voltage. This is believed to be due to two issues. The first of these is that increasing voltage increases deposition rate due to an increase in the frequency of hydrogen bubble formation and collapse. The second of these issues is that increasing voltage leads to increasing rate of arcing which erodes the sample. These two issues combined cause areas not prone to arcing (due either to electric field effects or electrolyte flow characteristics over the substrate surface) to grow at a faster rate than at lower voltages due to higher rate of plasma bubble formation and collapse. Areas which are more prone to arcing see a decreased growth rate, no growth, or even in some cases erosion into the substrate resulting from arcing related issues.

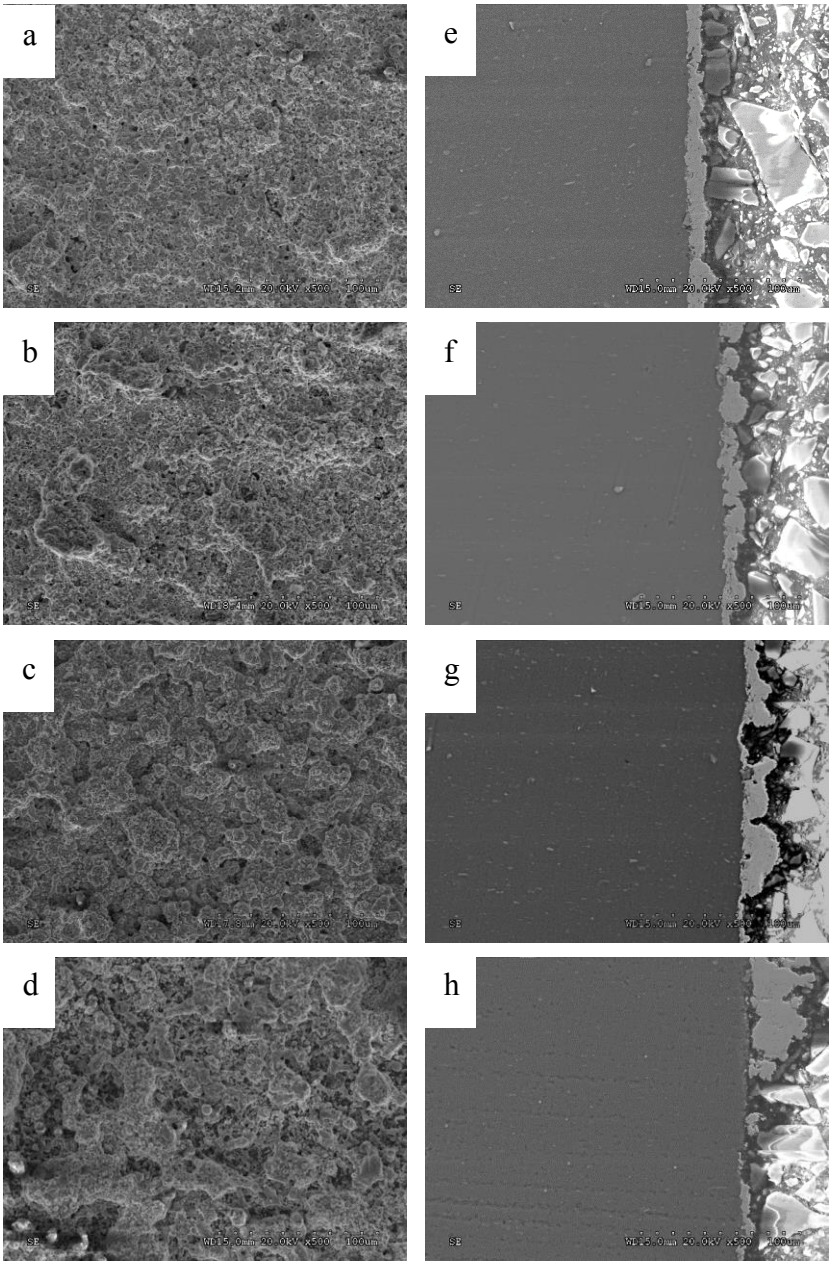

Figure 6-2. Surface and cross-sectional SEM micrographs of EPP deposited Ni on Al conducted at 185 V (a, e), 190 V (b, f), 195 V (c, g), and 200 V (d, h) for 60 s.

Coating thickness was measured and is presented in Figure 6-3. A general decrease in coating thickness is present as deposition voltage increases. While an increased deposition rate may seem likely due to an increased rate of hydrogen plasma formation, the opposite is clearly the case. This discrepancy is believed to be due to arcing, which even though happening at a low rate, appears to have a much greater effect on the Al substrate than was observed in previous work conducted with Fe substrates, likely due to its low melting temperature. In addition, the roughness of the coatings is presented in Figure 6-4 and shows a decrease in roughness with increasing deposition voltage. It is believed that this is caused by the higher arcing rate preventing large roughness from forming and, especially in the case of 200 V, causing a large portion of the sample to lack a coating and thus have a disproportionately low R_a value.

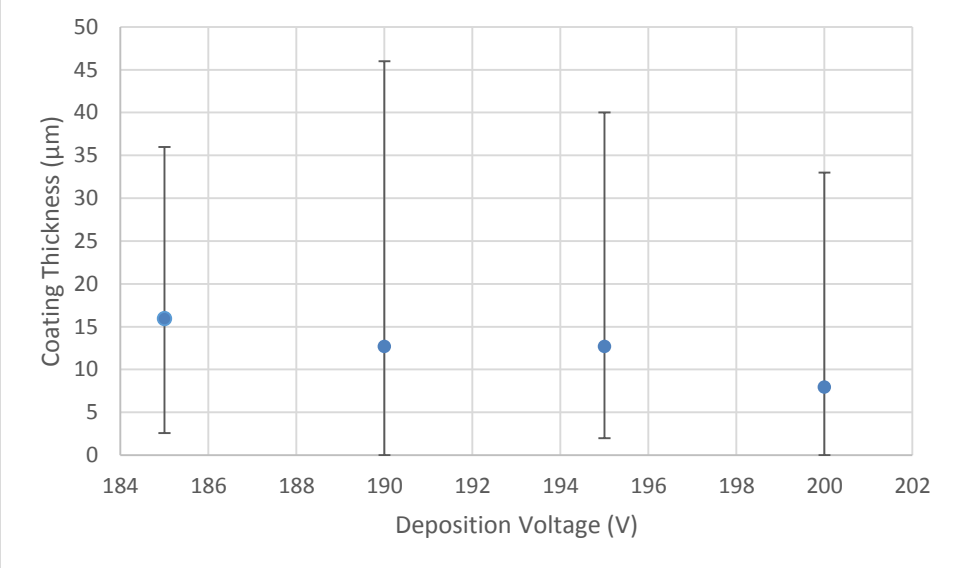

Figure 6-3. Average coating thickness for EPP depositions of 60 s for Ni on Al.

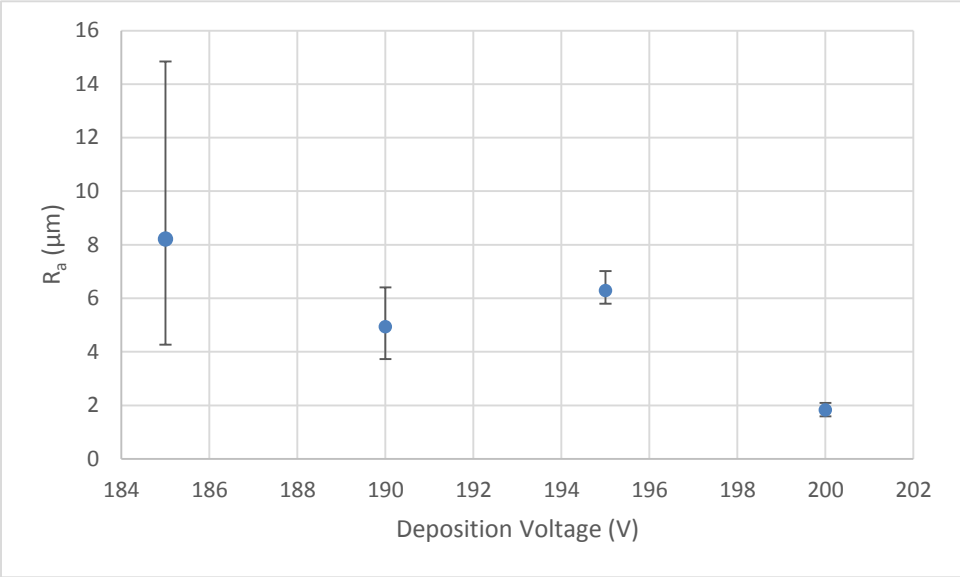

Figure 6-4. Average R_a values for EPP deposited Ni on Al by deposition voltage.

While the series of experiments above indicated a relationship between voltage and coating surface quality and continuity there were no observed intermetallics present in the surface coatings. Reports in literature indicate that increasing voltage leads to an increase in the penetration depth of the ionic species into the sample [29]. In an attempt to determine if this occurs with the present Ni-Al system voltage was increased to 210 V and cross sectional EDS measurements were taken, Figure 6-5. This figure shows the presence of intermetallics in the surface coating. The composition of Figure 6-5 shows a 3:1 ratio of Ni to Al which indicates the presence of Ni_3Al as the present phase. However, scans in other locations revealed the presence of different intermetallic compounds. Nevertheless, a discontinuous coating consisting of various Ni-Al intermetallic compounds was observed throughout the surface. In addition to indicating that intermetallics were present as the surface coating it is also of great importance to notice the level of oxygen present at the interface. No noticeable increase in the O content can

be observed above the level also present in the rest of the sample, indicating that this O content is most likely due to surface oxygen. This behavior is to be expected as the hydrogen plasma should act to reduce the surface oxide; nevertheless, this is very noteworthy due to high difficulty in coating Al due to its rapidly forming and highly durable surface oxide layer which tends to prohibit several common deposition techniques from being used.

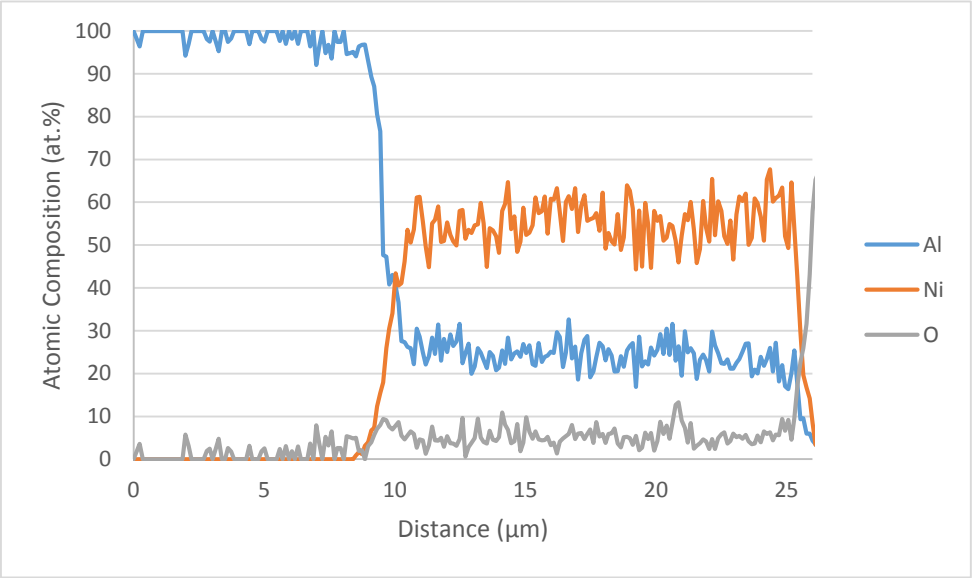

Figure 6-5. Cross-sectional EDS profile of EPP deposited Ni on Al using 210 V for 60 s.

Low angle XRD also was conducted in order to determine the presence of any intermetallic crystalline phases, Figure 6-6. Peaks indicating the presence of several intermetallic crystalline phases are clearly visible. Due to all of the intermetallic phases sharing at least one, and often several, planes with the FCC Ni or Al structure it makes determination of the phases present highly difficult and therefore the peaks are labeled

with the phases which may possibly exist within them. It should be noted that cross-sectional EDS supports the presence of all intermetallic crystal phases, however, the ratio Al and Ni in the intermetallics cannot be determined.

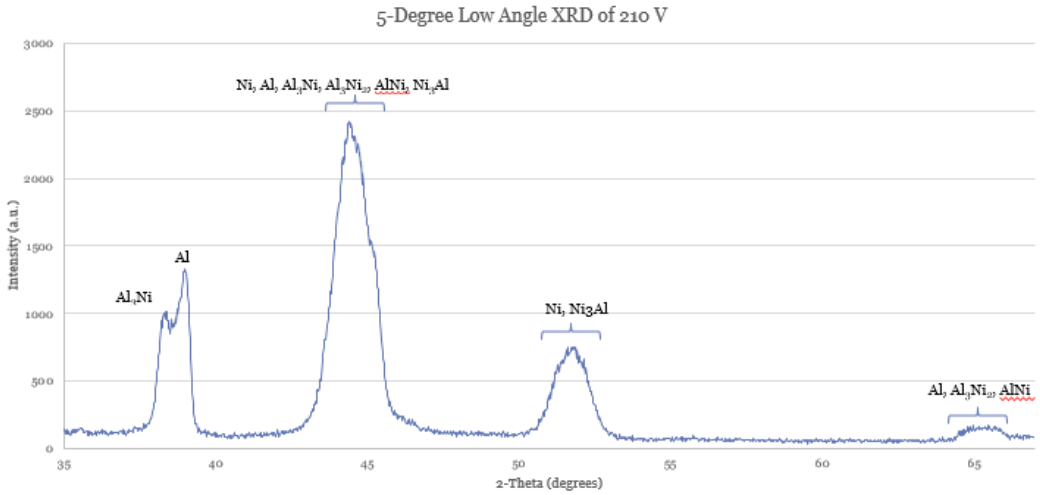

Figure 6-6. 5-degree low angle XRD spectra of Ni deposited on Al via EPP at 210 V for 60 s.

While the presence of these intermetallics is desirable the foremost concern is that the coating be as continuous as possible, and as previously explained this is not the case. A series of depositions was carried out with deposition intervals of 30 s, 60 s, and 120 s in order to determine the coating growth behavior at 210 V, these results can be seen in Figure 6-7. As can be seen from surface SEM, increasing deposition time dramatically increases the size of protruding nodules and appears to increase the coating coverage as well, although complete coverage is still not achieved. In addition, as deposition time increases the presence of small alumina particles becomes prevalent on the sample surface which, when combined with the less than full coating coverage, makes 210 V an unpromising deposition voltage.

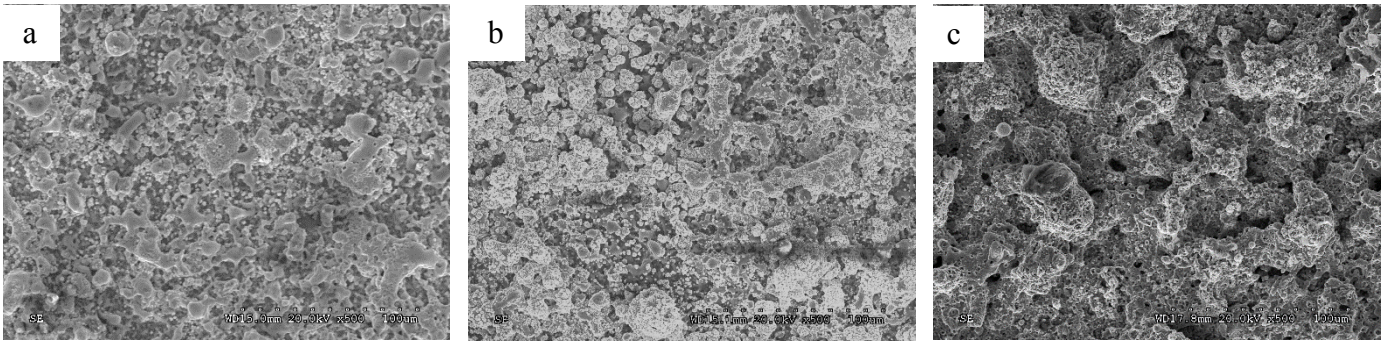

Figure 6-7. Surface SEM micrograph of EPP deposited Ni on Al using 210 V at 30 s (a), 60 s (b), and 90 s (c).

6.2.2 Deposition of Coatings using Determined Voltages

Two deposition conditions were chosen for further examination based on the results described above. The first, deposition entirely at 185 V was chosen due to the uniform surface coverage and rapid transition from Al to Ni in the surface coatings. The second deposition parameter studied entailed an initial deposition at 210 V and 30 s in order to establish an intermetallic anchor site for further deposition, which was then carried out at 185 V for the same reasons described above.

Depositions were conducted at 185 V and times of 30 s, 60 s, and 90 s in order to analyze the coating growth and behavior at the 185 V deposition parameter. A representative voltage and current vs. time graph of the 90 s deposition is shown in Figure 6-8 and the average voltage and currents for each deposition case is presented in Table 6-1. As can be seen, the voltage remains extremely constant throughout the deposition and only slight perturbations are observed. The variations seen in the deposition current are greater and are due to the constantly changing resistance of the electrolyte/plasma medium. Additionally, the results in Table 6-1 show that the average

current increases as deposition time increases, this is due to the method by which the sample surface is limited; an electrically resistive tape is wrapped around the cylindrical sample and as deposition progresses small amounts of Ni begin to be deposited on the tape nearest the exposed surface which in turn allows more Ni to be deposited farther from the sample. This leads to a gradual increase in the area which is electrically conductive and hence increases the exposed and apparent surface area. It should be noted that plasma does not appear to occur on the tape itself, but appears to only be electrodeposited which results in an additional route for current flow.

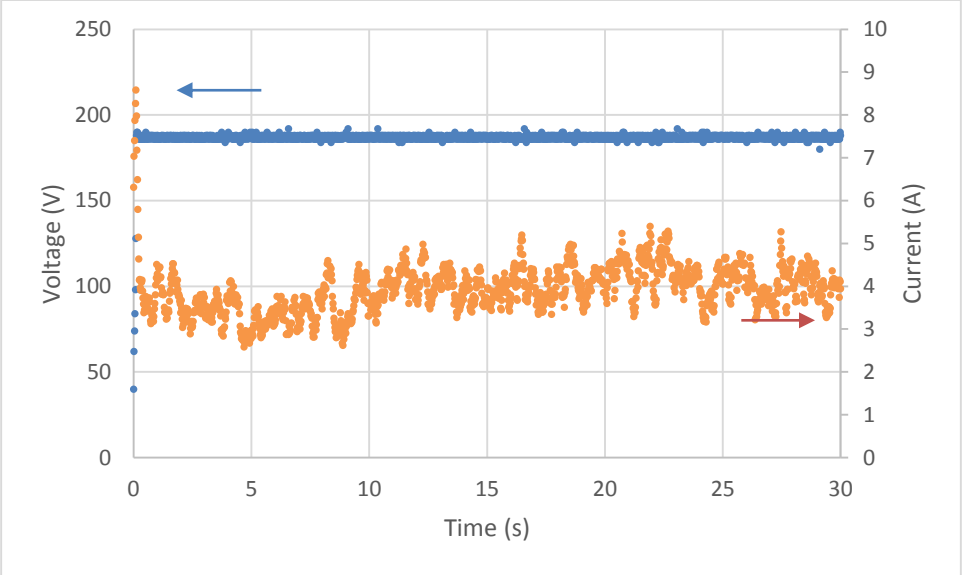

Figure 6-8. Representative voltage and current vs. time plot for 185 V deposition.

Table 6-1. Average voltage and current for 185 V deposition for 30 s, 60 s, and 90 s.

Sample	Avg V (V)	Avg I (A)
30 s	186.4	3.9
60 s	187.7	4.3
90 s	185.9	7.5

Figure 6-9 shows the cross sectional SEM images of 185 V deposition carried out at (a) 30 s, (b) 60 s, and (c) 90 s. Initial deposition up to 30 s shows a poor coating quality as the surface coverage is quite low. As can be seen, the coating continuity increases from 30 s to 60 s to the point at which it can be considered a fully formed surface coating, although some minor gaps in the coating may still be observed at isolated regions of the coatings. Increased deposition time beyond 60 s has the effect of increasing coating thickness while also further filling in the slight gaps in the coating which were observed in the 30 s deposition. Ten cross section micrographs were analyzed and five measurements of the coating thickness were taken in each image from which an average coating thickness was calculated. Figure 6-10 shows the coating thickness plotted against deposition time. The results show a high degree of linearity (an R^2 value of 0.964) and the deposition rate can be calculated as 245 nm/s. The high linearity and high deposition rate both suggest the method of deposition is due to metallic ion transport via bubble collapse as opposed to a diffusion related mechanism which would be expected to be slower and to decrease with increasing coating thickness. It can be recalled from the previous chapter that the deposition rate of EPP deposited Ni on Fe was ~ 165 nm/s, approximately 80 nm/s lower than the deposition of Ni onto Al. It is believed that the reason for this may be due to the much lower plasma voltage which is used in the Al deposition, leading to a lower rate of arcing and hence less surface damage. This would be expected to result in a higher coating growth rate.

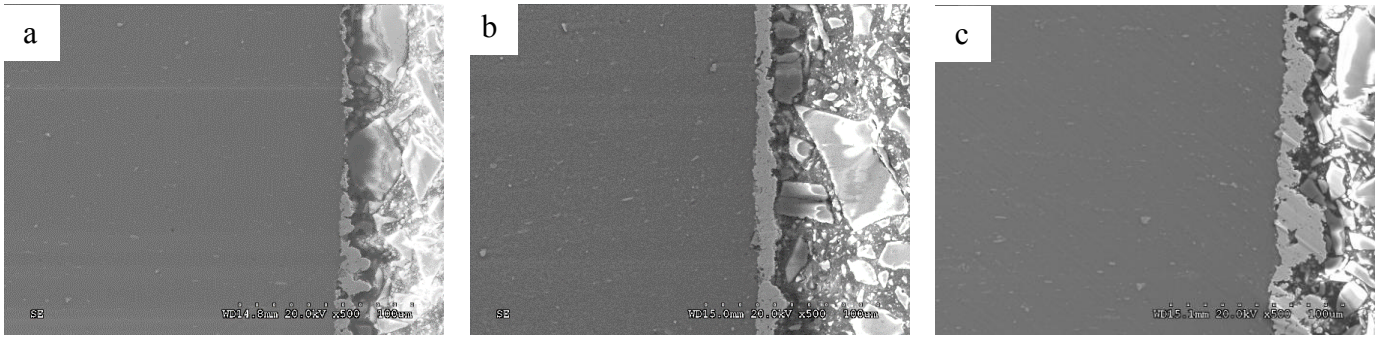

Figure 6-9. Cross-sectional SEM micrograph of Ni coatings deposited at 185 V and 30 s (a), 60 s (b), and 90 s (c).

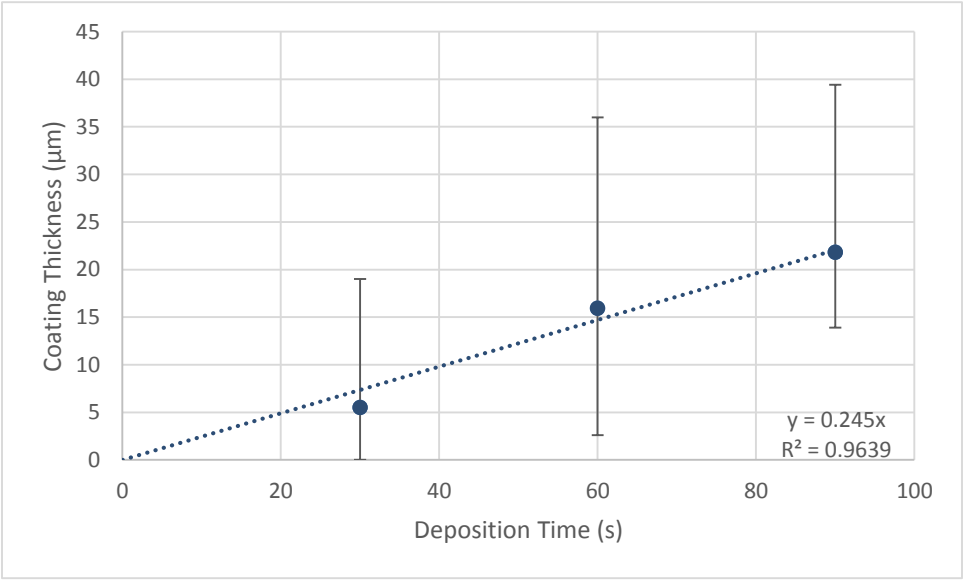

Figure 6-10. Deposition rate of EPP deposited Ni on Al at 185 V.

Depositions were similarly conducted on the 210/185V system with all samples being treated with an initial deposition step of 210 V for 30 s. A secondary deposition step was then conducted at the same voltage as in the previous experiments, 185 V, and for the same time intervals: 30 s, 60 s, and 90 s. A representative voltage and current vs.

time graph for a 210/185 V and 90 s deposition is shown in Figure 6-11. The average voltages and currents for each step are also presented in Table 6-2 for reference. Again, the voltage remains remarkably constant, but variations are seen in the current level, once again attributed to the variations in the resistance of the plasma/electrolyte medium as the process takes place. It should be noted that table _____ includes the average voltage and currents from the initial 210 V and subsequent 185 V steps, V_1/I_1 and V_2/I_2, respectively.

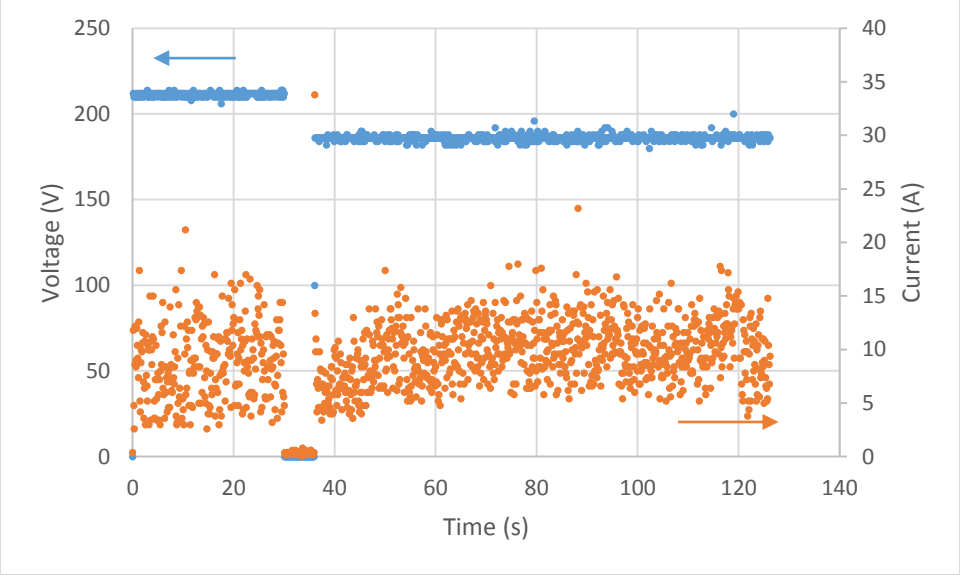

Figure 6-11. Voltage and current vs. time plot for 210/185 V, 90 s deposition.

Table 6-2. Average voltages and currents for 210/185 V Ni depositions at 30 s, 60 s, and 90 s.

Sample	Avg V_1 (V)	Avg V_2 (V)	Avg I_1 (A)	Avg I_2 (A)
30 s	210.5	185.8	9.2	10.1
60 s	210.5	185.8	7.9	8.7
90 s	211.4	185.8	8.8	9.9

Cross-sectional SEM micrographs are presented in Figure 6-12. The coating substrate coverage present in the 30 s deposition (Figure 6-12 a) shows an improvement over the substrate coverage seen in the same deposition time for the coating not containing the interlayer (Figure 6-9 a). While it can be argued that the comparison is not fully valid due to the added deposition time present in the 210 V processing step, it is believed that the added coverage is actually due to the incorporation of the intermetallic ridges acting as building blocks onto which the subsequent 185 V Ni deposition takes place. In addition to this, it is possible that small, fine intermetallics may also exist where no coverage appears to be present after the 210 V deposition. These intermetallics would then likely add a higher melting point layer upon which subsequent Ni growth can occur without the detrimental effect of depositing onto the low melting point Al. Gaps in the coating do appear in the 210/185 V – 30 s deposition, although fewer and smaller than what appear in the 185 V 30 s deposition, but appear to be eliminated at the 60 s deposition. Further deposition, up to 90 s, has the effect of further increasing the coating thickness.

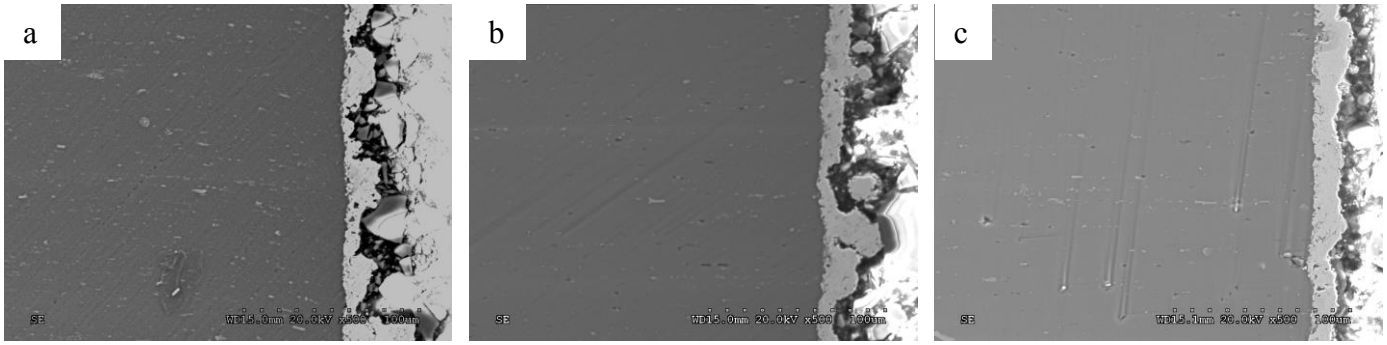

Figure 6-12. Cross-sectional SEM micrographs of 210/185 V Ni deposition on Al at 30 s (a), 60 s (b), and 90 s (c).

Similarly to the 185 V samples, cross-sectional thickness measurements were conducted and plotted, which can be seen in Figure 6-13. Again the behavior shown is

quite linear (R^2 value of 0.977). It should be noted that the deposition rate is slightly slower than that seen in the 185 V processes, although this may be due to small variations in the electrolyte composition, anode-cathode separation distance, and/or degradation of the anode. Analysis of the trend line suggests that the initial 210 V processing step imparts an initial coating thickness of ~7.5 μm. Of note is the increasing amount of scatter in the data, which increases as coating deposition time increases. This will be discussed in more detail in the following surface morphology section.

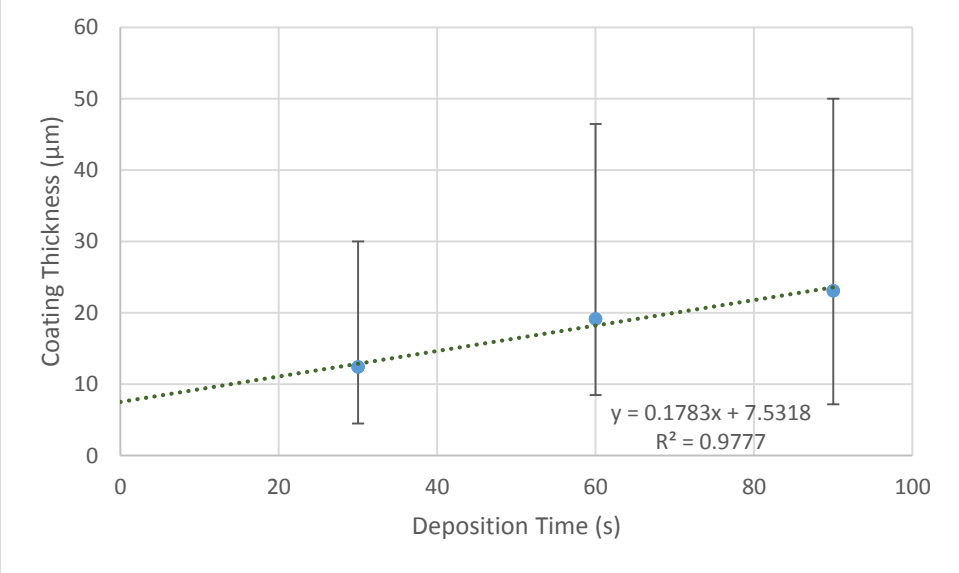

Figure 6-13. Deposition rate for 210/185 V EPP Ni depositions.

6.3 Characterization

Initial characterization of the developed coatings included investigations into the surface morphology and elemental composition. This was followed by a study of the mechanical properties of the coatings, such as surface hardness, coating adhesion, and

wear resistance, and then proceeded to determining the corrosion resistance afforded by the developed coatings. The full results of these characterization methods were analyzed and a comprehensive overview as to which of the two coatings offered better performance was determined.

6.3.1 Surface Morphology

To begin with, surface morphology was characterized with SEM microscopy, Figure 6-14. As can be seen, an increase in the deposition time leads to an increase in the nodule size and an apparent increase in the roughness of the sample surface. It is believed that areas which are preferential for deposition initiate growth of these nodules and, due to the lack of any change in the location of these nodules, Ni continues to preferentially deposit in these regions leading to increased roughness. A significant portion of this phenomenon may be alleviated by the introduction of a rotation to the sample or anode which would continuously change the interplay between the electric field and the substrate eliminating the irregular growth in these regions

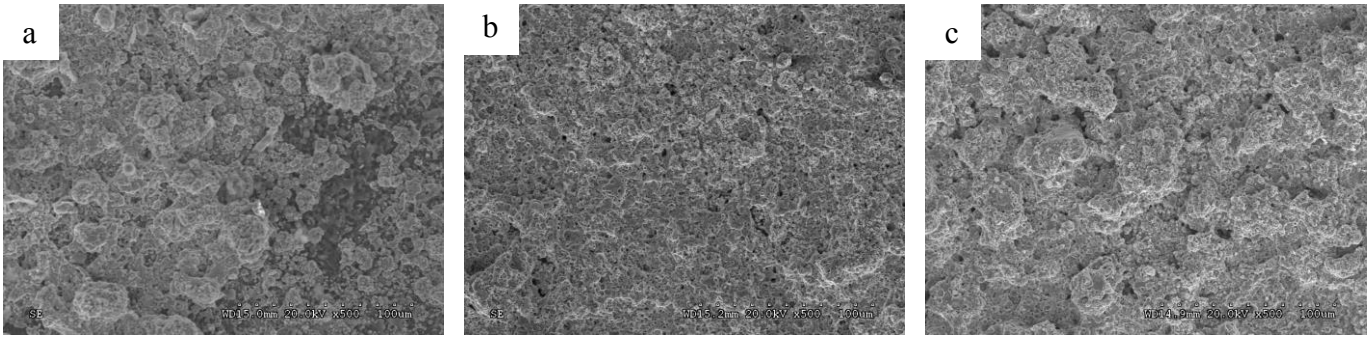

Figure 6-14. Surface SEM micrographs of 185 V EPP Ni depositions at 30 s (a), 60 s (b), and 90 s (c).

Surface SEM analysis was conducted on the 210/185 V samples, given below in Figure 6-15, and showed similar results to what was observed in the 185 V depositions. Much like the 185 V deposition group, the results from the 210/185 V deposition appears to show that the surface roughness increases with increasing deposition time. The cause of this is attributed to the same as that attributed to the above case, namely that preferential deposition sites continue to see increasing deposition due to a lack of substrate rotation. Additionally, it may be possible that added roughness in this case is due to the inclusion of the 210 V, 30 s deposition step which will add an initial roughness prior to the application of the 185 V step.

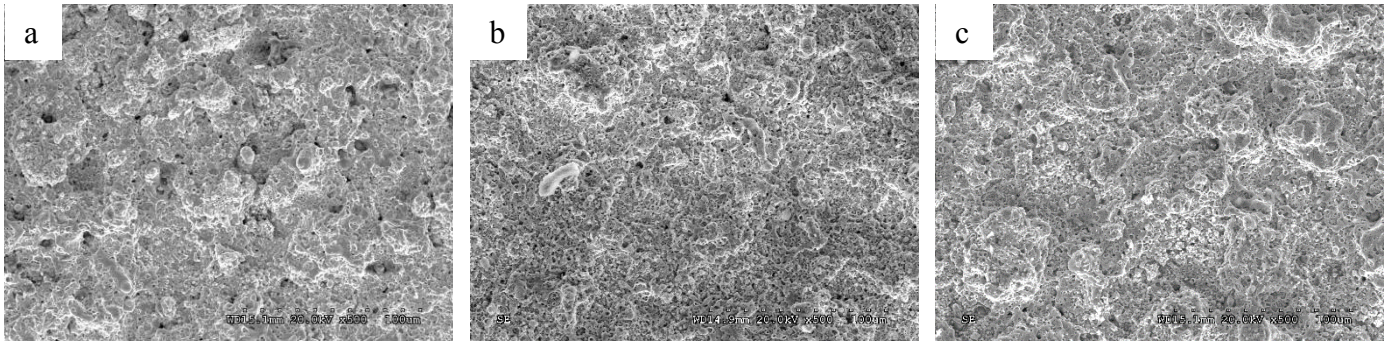

Figure 6-15. Surface SEM micrographs of EPP deposited Ni coatings at 30 s (a), 60 s (b), and 90 s (c).

A more quantitative approach to determining the deposition parameters' effect on surface morphology was conducted with the use of optical profilometry. Measurements were taken at ten different locations on the coating and an average value was determined. The averages for each coating is presented in Figure 6-16, it should be noted that error bars were omitted from the graph intentionally in order to avoid confusion due to overlapping measurements. An increase of R_a is observable with respect to deposition time in both deposition parameters, though it is far more severe in the case of the 185 V deposition. Additionally, it can be seen that the initial roughness attributed to

the 210/185 V deposition at 30 s is higher than that of the 185 V case. This is most likely due to the deposition onto the rougher initial surface from the 210 V deposition step. Furthermore, the greater increase seen in the 185 V samples may be due to a less favorable deposition base as the lower melting temperature Al tends to resist Ni deposition initially. Finally, a levelling off of the roughness is observed in the 185 V deposition at 90 s which, while not present in the 90 s deposition of the 210/185 V sample, may suggest that a maximum roughness is possible with the processes and that longer deposition times with the 210/185 V sample may reach a maximum roughness as well.

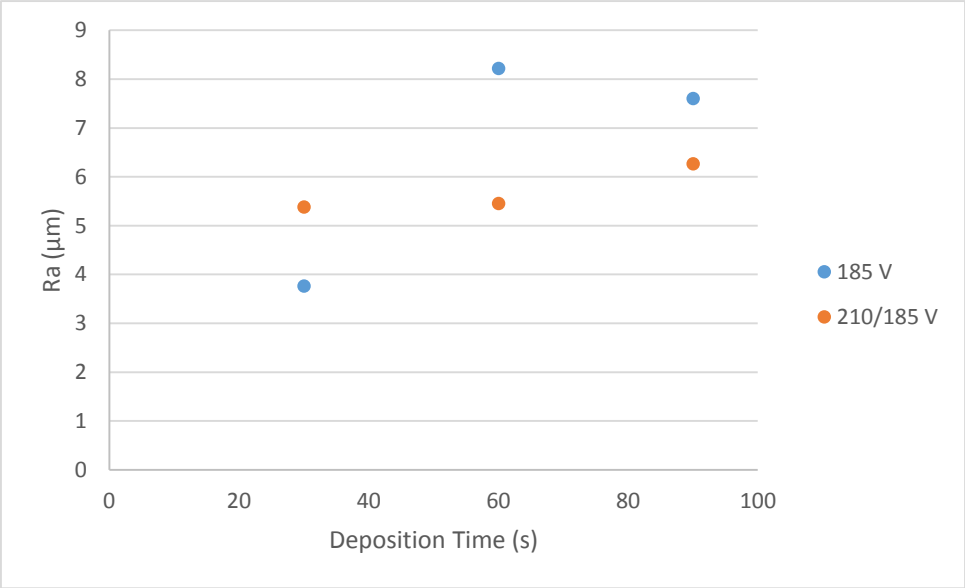

Figure 6-16. Surface roughness values, R_a, for 185 V and 210/185 V EPP deposition.

6.3.2 Elemental Composition

Determination of the elemental composition was an area of high interest in this research and began with the development of XRD spectra for the 185 V system. For this sample group, the 90 s deposition was used in order to improve the intensity of the signal from the Ni coating, and to limit any signal received from the Al substrate, due to its increased thickness. The results of the XRD study is given in Figure 6-17. No intermetallic phases, either in the form of additional peaks or as apparent shoulders, can be observed, and the only crystalline phase which is observed is due to Ni. Both the (111) and (200) phases can be seen. Additionally, the (111) and (200) 2-θ Peak angles match up well, at 44.4° and 51.9°, respectively, with the expected angles for Ni, and the relative peak intensities suggest a random orientation of the crystal structures and the absence of any texturing. This is to be expected as the low plasma intensity of the 185 V deposition limits the ability of the substrate and the coating to interact and should lead to a fully Ni deposited layer. The XRD results are further supported by the analysis conducted with cross-sectional EDS, a representative example of which can be seen in Figure 6-18. As can clearly be observed the Ni content increases rapidly from zero up to nearly 100%. Additionally, the transition from Al to Ni happens in a very short distance, well within that expected of the electron beam's excitation volume, indicating a near instant transition zone. Of note is that the oxygen content at the interface shows no noticeable increase, although some cross-sectional EDS scans do show a small amount of O (~10-15 at. %) at the interface. This indicates that while the hydrogen plasma does tend to eliminate the oxide layer, in some instances full elimination may not occur before deposition of Ni has covered the oxide layer. However, even in instances where O is

present, the amount is far less than what is expected if the hydrogen plasma were not seen to be reducing the oxide.

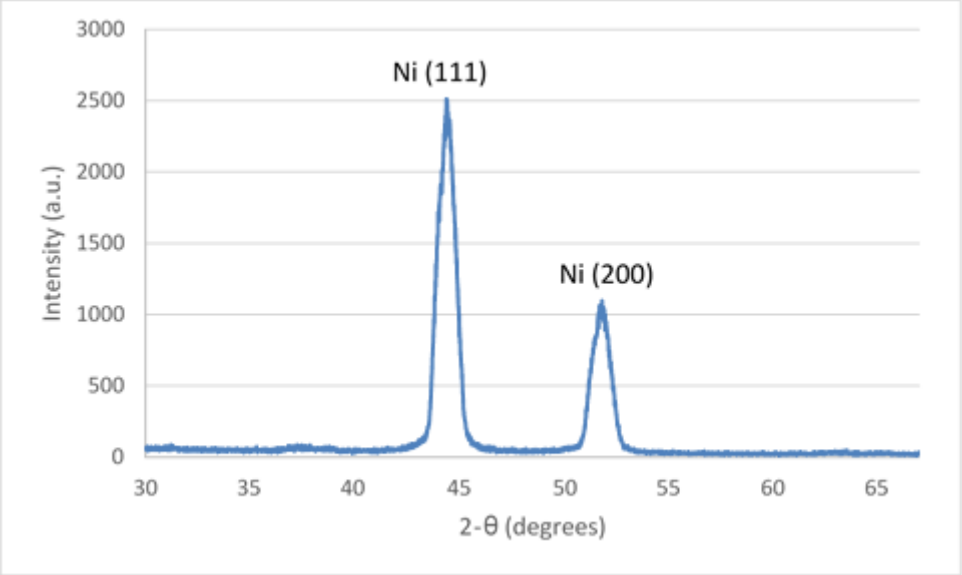

Figure 6-17. 5-degree low angle XRD spectra of 185 V, 90 s EPP deposited Ni on Al.

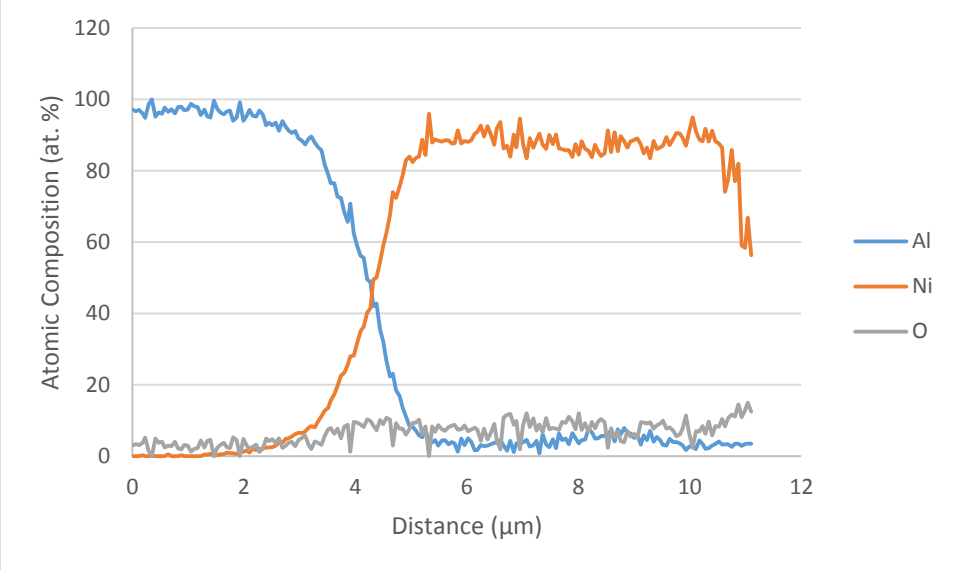

Figure 6-18. Cross-sectional EDS line analysis of 185 V deposition of Ni on Al.

Similar analysis was conducted on the 210/185 V samples and the XRD spectra can be seen below in Figure 6-19. For simplification, only the main element peaks are identified. However, it is clear that there are several shoulders and significant peak broadening present and that separate phases do exist other than the Al substrate, which has a small signal showing for the (111) peak, and the coated Ni which shows peaks at the (111) and (200). Due to the high complexity associated with several peaks, of several phases, overlapping within a few degrees it is not practical to make large assumptions about the phases present. Although, it is possible to determine that the main peaks for the sample lie at 44.60° and 51.90° which are extremely close to the expected values for Ni of 44.37° and 51.67°, respectively. This suggests that the surface layer is likely pure Ni, and small signals are present from underlying intermetallic phases present at the Al-Ni interface.

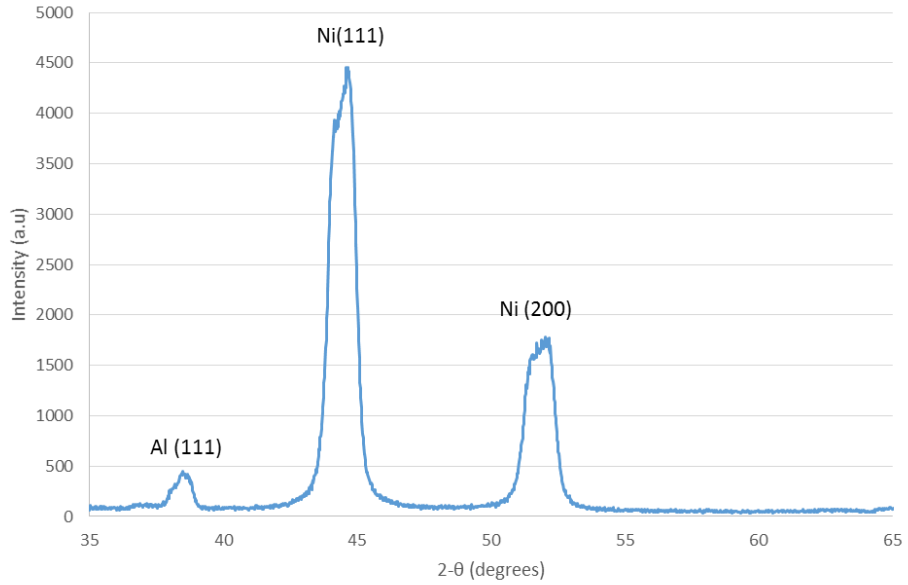

Figure 6-19. 5-degree low angle XRD spectra of 210/185 V 90 s EPP deposited Ni on Al.

Inspection of cross-sectional EDS, shown in Figure 6-20, shows that the sample exists in two discreet layers; further supporting the conclusions drawn from the XRD data presented previously. An initial layer, consisting of dispersed ridges of Ni-Al intermetallics, deposited by the 210 V 30 s processing step, and an upper layer consisting of a ~100% Ni composition, deposited by the subsequent 185 V processing step. These results confirm that the 210/185 V coating results in an interlayer of dispersed intermetallics covered by a dense and continuous coating of Ni. It should be noted that several compositions are observed through cross-sectional EDS and that XRD results presented previously further suggest the presence of several intermetallic phases in the coating. Therefore, it can be concluded that no single intermetallic is present but that a range of the possible intermetallics is spread across the sample. It is expected that this interlayer will prove beneficial in both the mechanical properties and the corrosion properties of the coatings.

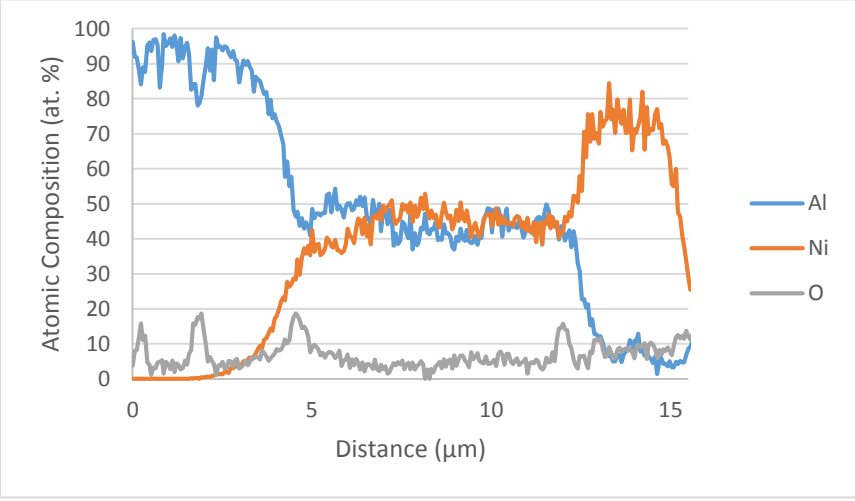

Figure 6-20. Cross-sectional EDS line analysis of dual layer structure of 210/185 V EPP deposited Ni on Al.

6.3.3 Mechanical Properties

6.3.3.1 Adhesion

Adhesion experimentation revealed a marked difference between the coatings containing an interlayer and those without an interlayer. For those without an interlayer, deposited with only the 185 V condition, coating pull-off was observed at very low loads and, typically, the stud was covered entirely by the Ni coating afterwards. However, for the coatings created with the initial 210 V processing step much higher loads were required to remove the coating. In this case, it was observed that the bonded epoxy fractured prior to coating adhesion failure in some cases, and in those cases where fracture occurred earlier than expected the stud was observed to only be partially covered with the Ni coating. This suggests that the coating may not have had a uniform adhesion across the sample and that in some areas it was stronger than the 70 MPa fracture strength of the adhesion stud. Figure 6-21 presents a load vs. displacement curve for an adhesion test in which the epoxy failed prior to the delamination of the coating.

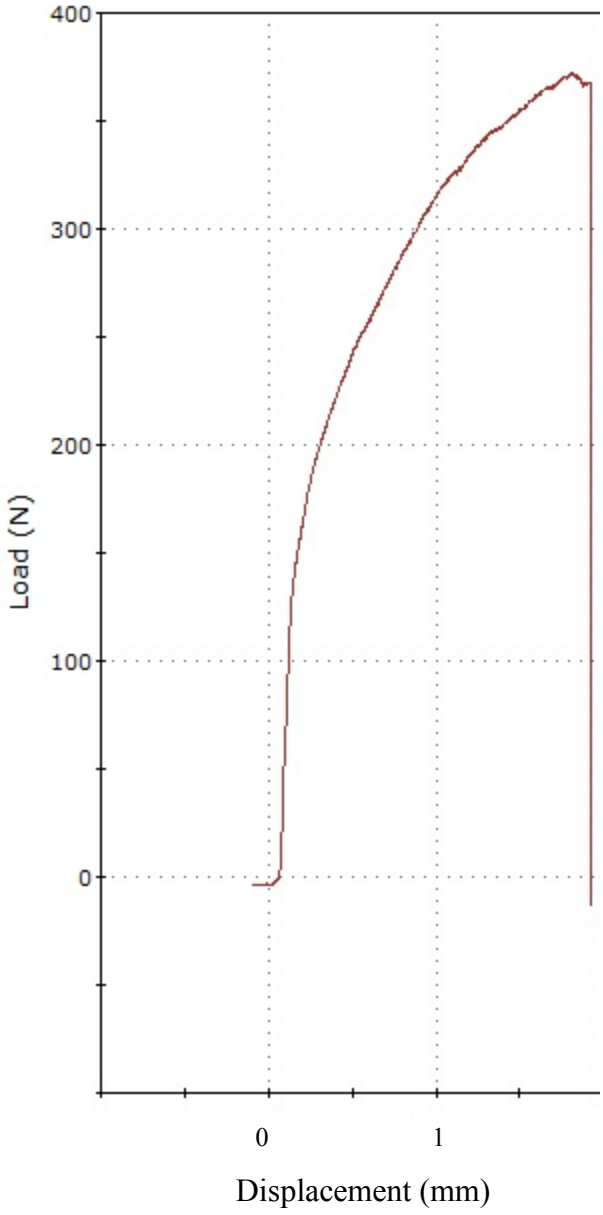

Figure 6-21. Load vs. displacement curve of 210/185 V 90 s EPP deposited Ni on Al.

6.3.3.2 Hardness

Using Eq. 3-2, the grain size of the EPP deposited Ni was approximated to be 125 nm, indicating a nanocrystalline structure, as expected, and suggesting an improvement to the hardness when compared to that of bulk Ni. Hardness values of the 185 V – 90 s sample were taken with a Vickers hardness microindenter using 100 g_f and 50 g_f. The calculated hardness was found to be ~2.2 GPa for both indenting loads, suggesting a measure of reliability to this number. This value fits well with hardeness values for nanocrystalline Ni reported in literaure. Figure 6-22, adapted from [47], shows the hardness values vs. grain size with our determined hardness value inserted. As shown, the determined hardness fits well within the pattern displayed in the graph.

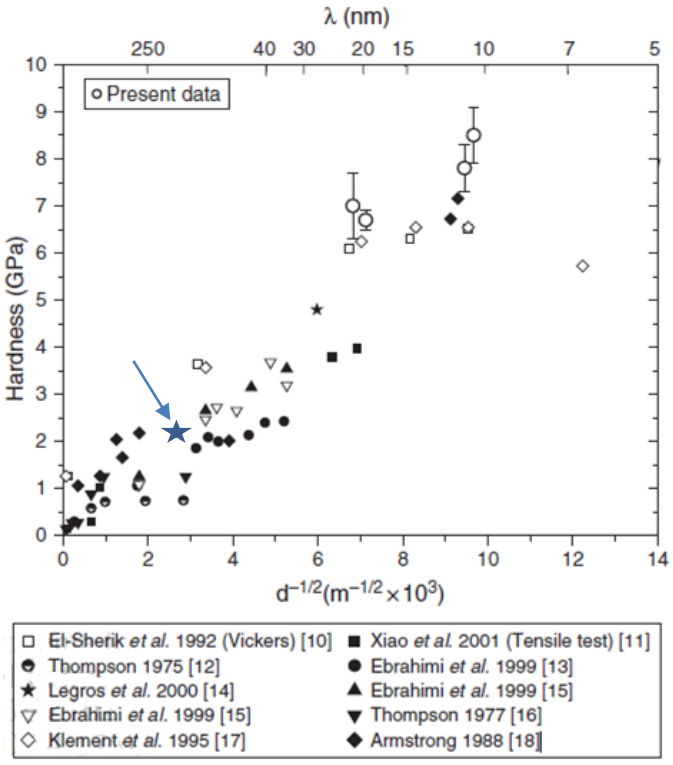

Figure 6-22. Hardness vs. grain size plot. Adapted from [49].

6.3.3.3 Tribological Properties

Examination of the tribological properties was conducted on samples deposited for 60 s and 90 s; the wear properties of the 30 s deposition sample was not investigated due to the non-continuity of the coating. The wear scar from the 210/185 V 90 s sample is shown in the SEM micrograph in Figure 6-23. The presence of gouges along the path of the wear scar suggests that the method of wear is likely due to abrasion. In addition, cracking of the wear scar is believed to be attributed to both the high rate of loading and unloading and the high number of these cycles that the sample undergoes. In effect, the surface suffers from fatigue due to the wear experiment, another possible source of wear. Finally the surface of the wear scar was shown to contain high levels of oxygen, ~50 at. %, which is believed to be the cause of the charging present in the images. This indicates that the surface has converted to Nickel Oxide likely caused by the high heat resulting from the small wear radius and high revolution speed used in the experiments. It should be mentioned that the alumina ball lacked the presence of any detectable wear scar. This can be supported by the lack of any flat bottom to the wear scar in the Ni coating (observable in the 2-D wear scar in Figure 6-26 below) and by the negligible Al content detected in the wear scar itself. A representative EDS spectra of the wear scar of an EPP deposited Ni coating containing the intermetallic interlayer with a deposition time of 90 s is given in Figure 6-24, and the average atomic composition of the wear scar is presented in Table 6-3 as well for reference. It should be noted that the Al content is similar to that present in similar EDS results from areas of the coating not within the wear scar indicating that the Al is likely a small signal coming from the substrate.

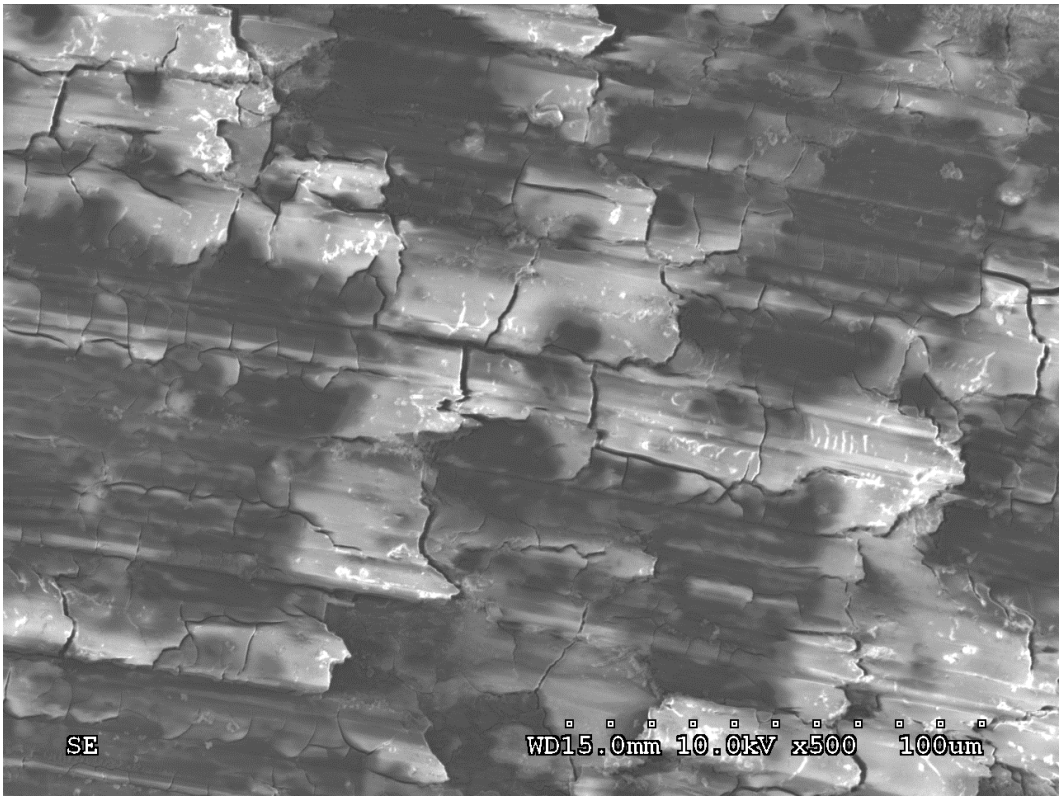

Figure 6-23. SEM micrograph of wear scar after 1,000 m (~53,000 rev) on 90 s deposited sample with interlayer.

Table 6-3. Average elemental composition of wear scar of EPP deposited Ni coating on Al containing intermetallic interlayer, deposited for 90 s.

Element	Elemental Composition (at. %)
O	48.36
Al	2.10
Ni	49.54

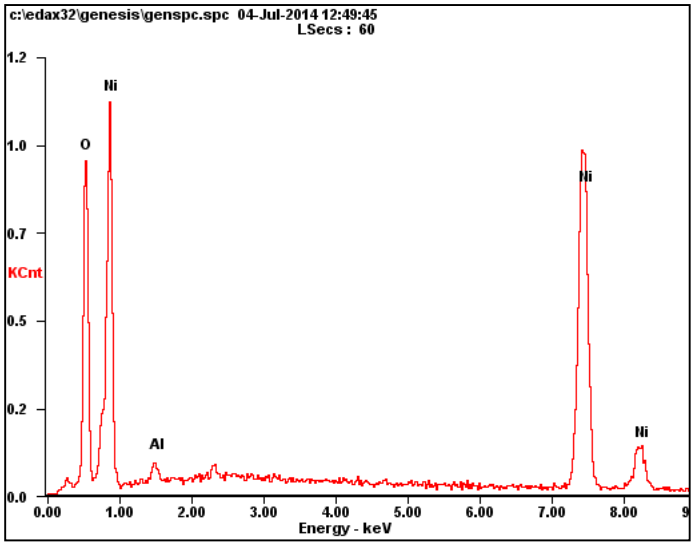

Figure 6-24. Representative EDS spectra of wear scar.

Optical profilometry was utilized in order to study the wear scar and to determine the amount of material removed from the sample. Figure 6-25 displays the 3-d wear scar data obtained via optical profilometry. The presence of the wear scar is easily distinguished from the surrounding surface roughness. Of note is the presence of low spots within the wear scar. Investigations of these regions, both through optical profilometry and through SEM microscopy reveals that these regions are low “valleys” of the coating, demonstrating that the wear scar has not yet worn fully through the surface roughness, even after ~53,000 revolutions. Optical profilometry was also used to calculate the 2-D cross-sectional profile of the wear scar which can be seen in Figure 6-26.This wear cross section was used to determine the wear rate of the samples utilizing Eq. 3-4. It should be noted that due to the high surface roughness of the sample, assumptions were made in order to estimate the wear rate of the EPP processed samples, specifically it was estimated that the coating made up approximately 25% of the volume extending from the surface.

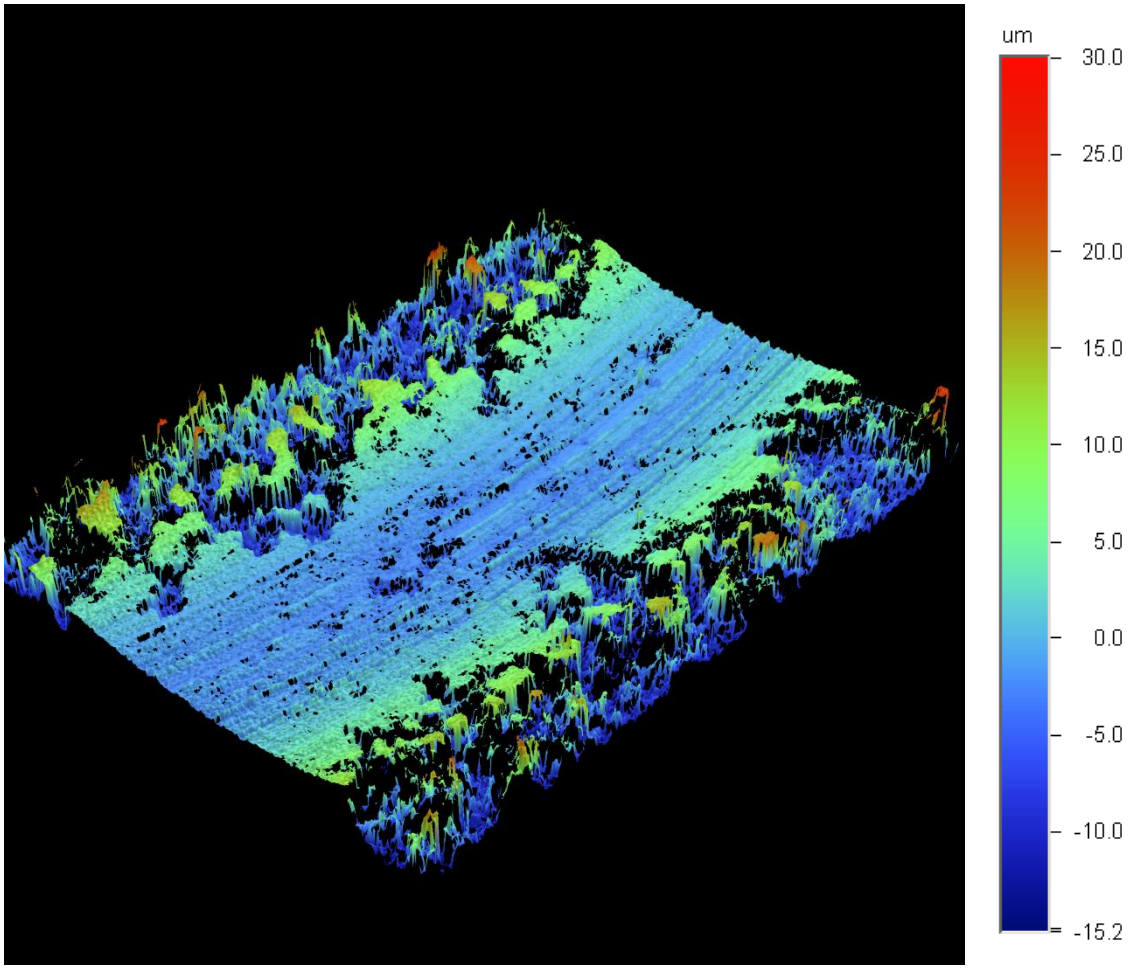

Figure 6-25. 3-D representation of wear scar and surface roughness.

Results showing the coefficient of friction vs. sliding distance can be seen below in Figure 6-27, which shows representative plots for the two 90 s samples. The overall trend, a rapid decrease followed by a gradual increase before leveling off around 250 m was typical for all processed samples at each of the two deposition times. This behavior was also observed in the friction response of bulk Ni, which was studied for comparison purposes, although the break-in period was much quicker. The behavior observed is

believed to be caused by several phenomenon: the initial high friction and rapid decrease is due to elimination of debris from the surface, and the following increase is due to the wearing away of the surface roughness.

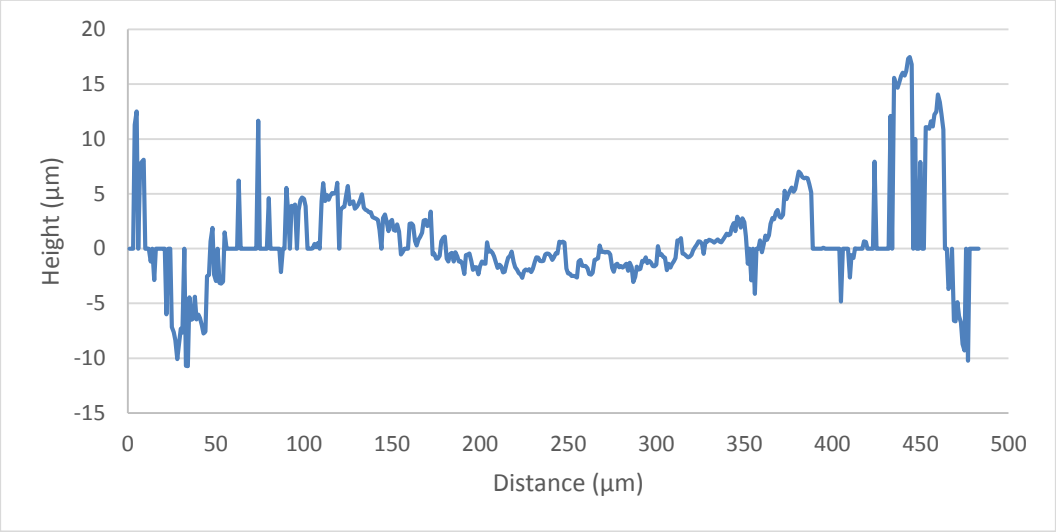

Figure 6-26. 2-D wear scar cross-section of 90 s deposited sample containing intermetallic interlayer.

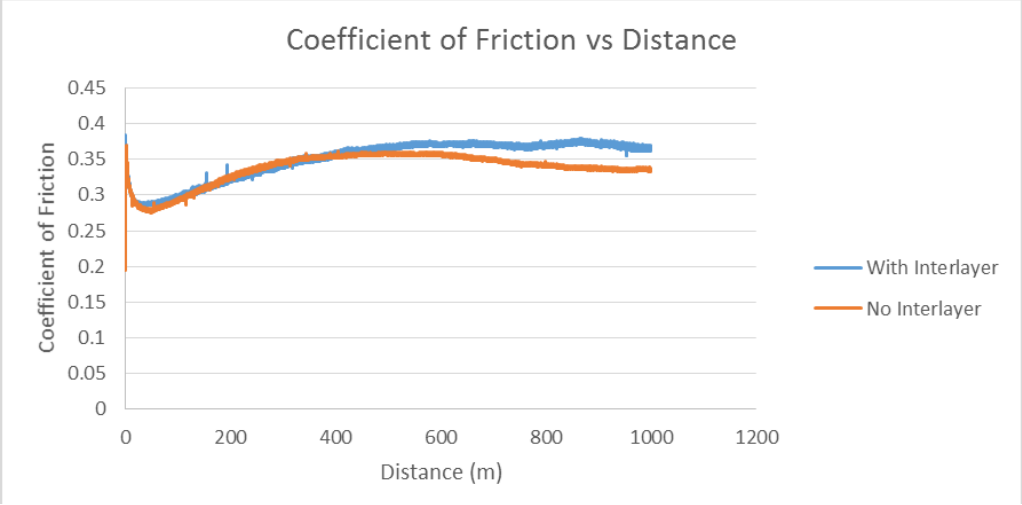

Figure 6-27. Coefficient of friction vs. sliding distance for samples with and without intermetallic interlayer.

Lastly, the wear rate was determined and plotted against the wear distance, given in Figure 6-28. Additionally, control samples of Ni 200 and Al 1100 were used in order to compare the wear rate against these materials. The results show a large decrease in the wear rate of the EPP Ni coated samples when compared to the uncoated Al substrate. In addition, both the 60 s and the 90 s coating containing the 210 V intermetallic interlayer show a slight improvement over the corresponding coating which lacks the interlayer. It is believed that this is likely due to the ability of the hard intermetallic to better support and distribute the load applied to the Ni surface layer. In the coating lacking the interlayer there is likely a larger amount of warping which occurs as the alumina ball passes over the coating which should result in a slight decrease in wear resistance. In addition the coefficient of friction was determined after the wear had reached a steady state, after 250 m. The results for show a slight increase in the coefficient of friction for samples which contain the 210 V intermetallic interlayer. This could be due to the more rigid nature of the coating leading to the coating abrading the alumina ball more than the coating without the interlayer. However, it should be noted that EDS inspection of the wear scar resulted in similar Al values as EDS measurements taken in non-worn areas. Regardless of the slight increase in the coefficient of friction present in the coatings containing the intermetallic interlayer, the coefficient of friction was found to be significantly lower than that of the uncoated Al substrate. All samples showed a wear rate improvement over the Al substrate material with best results obtained for a deposition time of 90 s for the 210/185 V condition in which case an improvement of nearly 1.5 orders of magnitude was observed.

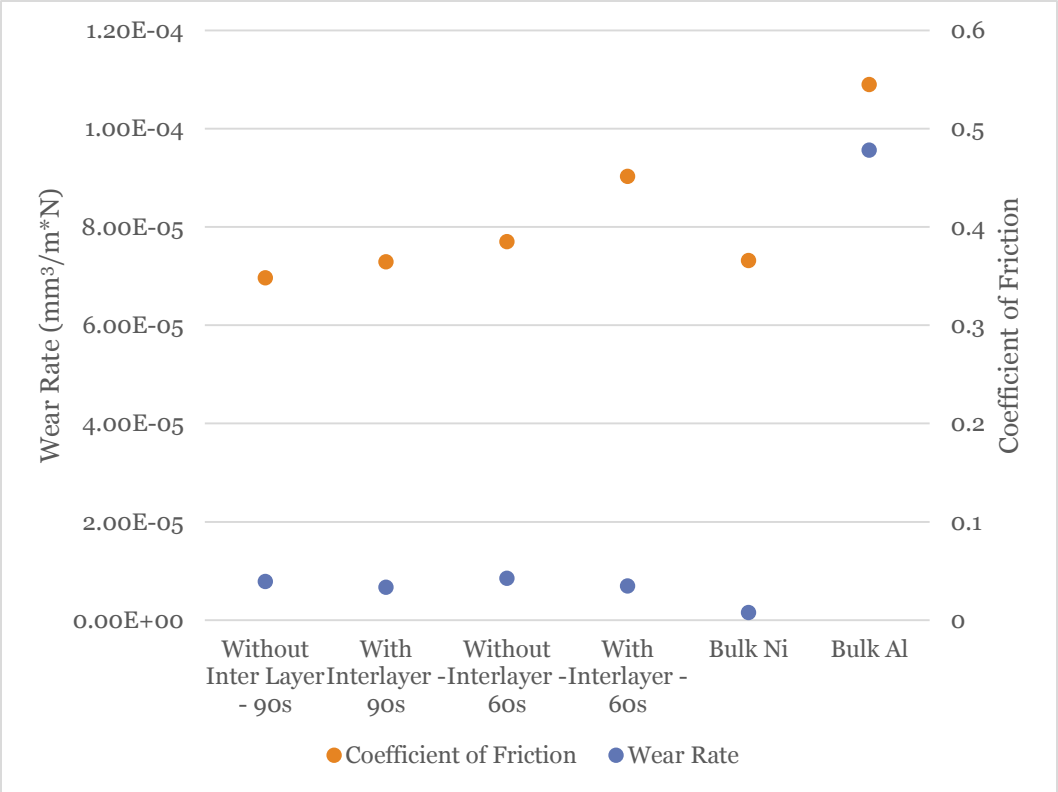

Figure 6-28. Wear rate and coefficient of friction of EPP deposited Ni on Al with and without intermetallic interlayers and for Ni and Al control samples.

6.3.4 Corrosion Properties

It was believed that the application of the EPP deposited Ni coatings would lead to improvements of the corrosion properties of the Al substrate, and in order to determine the effectiveness of the coatings in this application a study of the corrosion properties of the samples was carried out. Corrosion properties were investigated through the use of open circuit potential vs. time and anodic polarization.

6.3.4.1 Open-Circuit Potential vs. Time

OCP vs. time experiments were made in order to determine the long term corrosion potential of the samples. Experiments were conducted on all samples (185 V – 30 s, 60 s and 90 s and 210/185 V – 30 s, 60 s, and 90 s) as well as with control samples of AISI Ni 200 (referred to as Ni) and AISI Al 1100 (referred to as Al) in order to define the improvement of the coating over the substrate material and to observe the level of improvement when compared to bulk Ni. The OCP vs Time plot is shown below in Figure 6-29 and the OCP values are given in Table 6-4. An additional representation of this plot, with the upper and lower voltages displayed altered so as to better display the coated samples' behavior, is also presented as Figure 6-30 for reference. From inspection of the OCP figures and table it can be observed that all coated samples appear to exhibit very similar OCP values, ranging from -745 mV up to a value of -727 mV. In addition, the samples are divided roughly into a bottom group, consisting of the samples without the intermetallic interlayer, and an upper group, which contains the interlayer. This suggests that the presence of the interlayer does offer an improvement, albeit small, to the corrosion resistance off the coating. Additionally, a general trend suggests that increasing deposition time does lead to an increase in the corrosion potential, and thus an increase in the corrosion resistance. In the case of the coatings lacking an interlayer an improvement is observed from the 30 s sample to the 60 s sample and finally to the 90 s sample. However, in the coating containing the interlayer the lowest corrosion potential is still the 30 s sample but it is followed by the 90 s sample with the highest value presenting as the 60 s coating. The values of the 90 s and 60 s sample are extremely close, showing a difference of only one mV, and the difference is well within the slight variations seen in the behavior of the OCP vs. time graph. Additionally, the OCP value of

the 210/185 V 90 s sample shows a much more gradual decrease than that seen in the other samples, suggesting that it may yet offer a better corrosion resisting performance than the other materials. With this in mind, the largest improvement in the OCP value was attained with the 60 s sample (and can be assumed to be the 90 s sample as well) containing the intermetallic interlayer which showed an improvement of ~100 mV or roughly 12%. The behavior observed in the EPP deposited Ni on Al is very similar to that of EPP deposited Ni on Fe reported in the previous chapter. All deposited coatings are seen to have an OCP between that of the Ni and Al control samples and all are seen to move closer towards the Al value as time progresses. The reasons for some of the overall lower values can be attributed to the nano-crystalline nature of the EPP coatings which leads to a high concentration of more active grain boundaries and triple junctions. The behavior observed in which the OCP moves towards the Al value as the experiment progresses may be due to the presence of micro-cracks in the coating which, although these microcracks, were not observed with SEM. These cracks would be expected to allow access to the Al substrate which would lower the overall OCP but time would be needed for the electrolyte to penetrate into the cracks which would result in a gradual decrease in the OCP as electrolyte was able to reach the substrate. The resultant OCP vs. time curve would be expected to look similar to what is shown in the figure below.

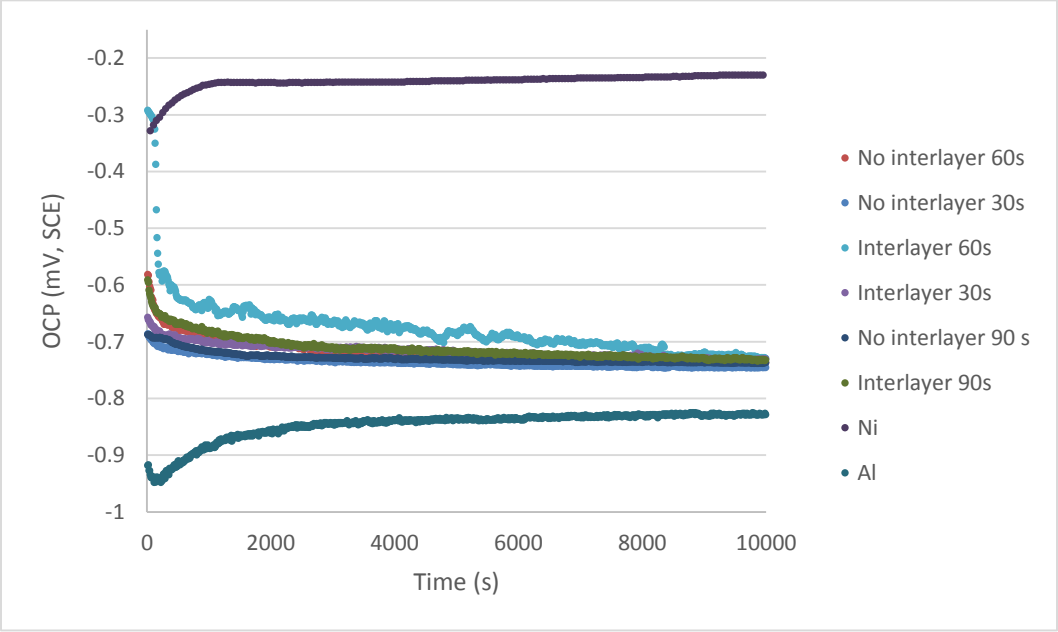

Figure 6-29. OCP vs. time plot for all EPP coated Ni on Al samples and Ni and Al control samples.

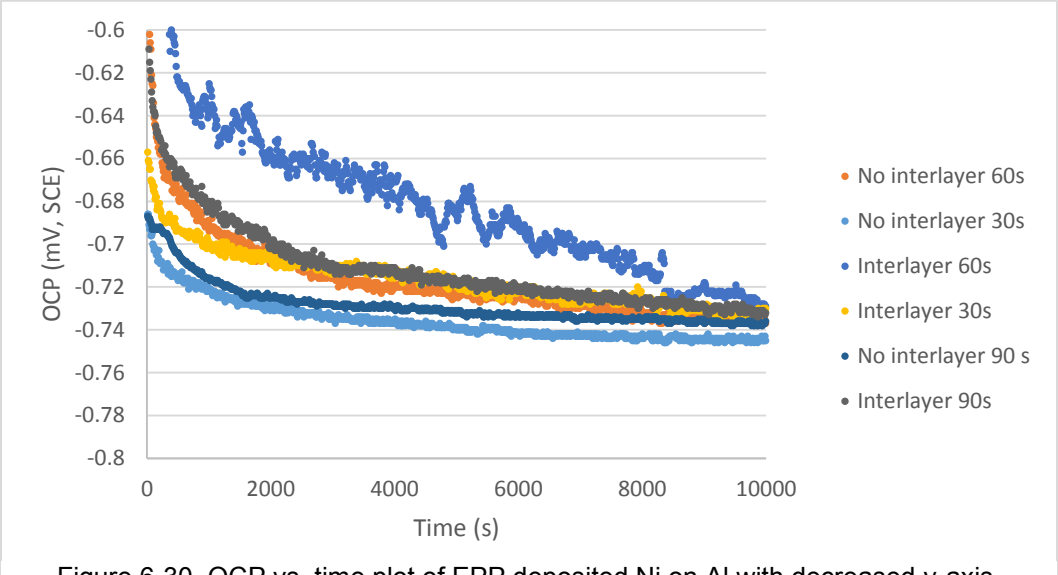

Figure 6-30. OCP vs. time plot of EPP deposited Ni on Al with decreased y-axis, presented for reference.

Table 6-4. OCP values for EPP deposited Ni on Al as well as Ni and Al control samples.

Sample	OCP (mV, SCE)
Ni	-230
Al	-828
W/Interlayer	
90 s	-728
60 s	-727
30 s	-730
W/o Interlayer	
90 s	-737
60 s	-736
30 s	-745

Surface and cross sectional images of the coatings lacking an interlayer are given in Figure 6-31 and those of the coatings containing the interlayer are given in Figure 6-32. Surface SEM images (Figures 6-31 and 6-32 a, b, and c) show the accumulation of corrosion debris with a large quantity visible in the two 30 s deposition samples. The cross section SEM indicate that the coatings have sustained some damage during their 10,000 s exposure to the NaCl solution and this can be seen in the degradation of the coating itself. Pits and gaps in the coating can be seen which are not evident in the coatings prior to the OCP experiments. While the coatings do appear to significantly improve the corrosion resistance of the Al substrate, this presence of coating degradations suggests that this improvement may not be indefinite.

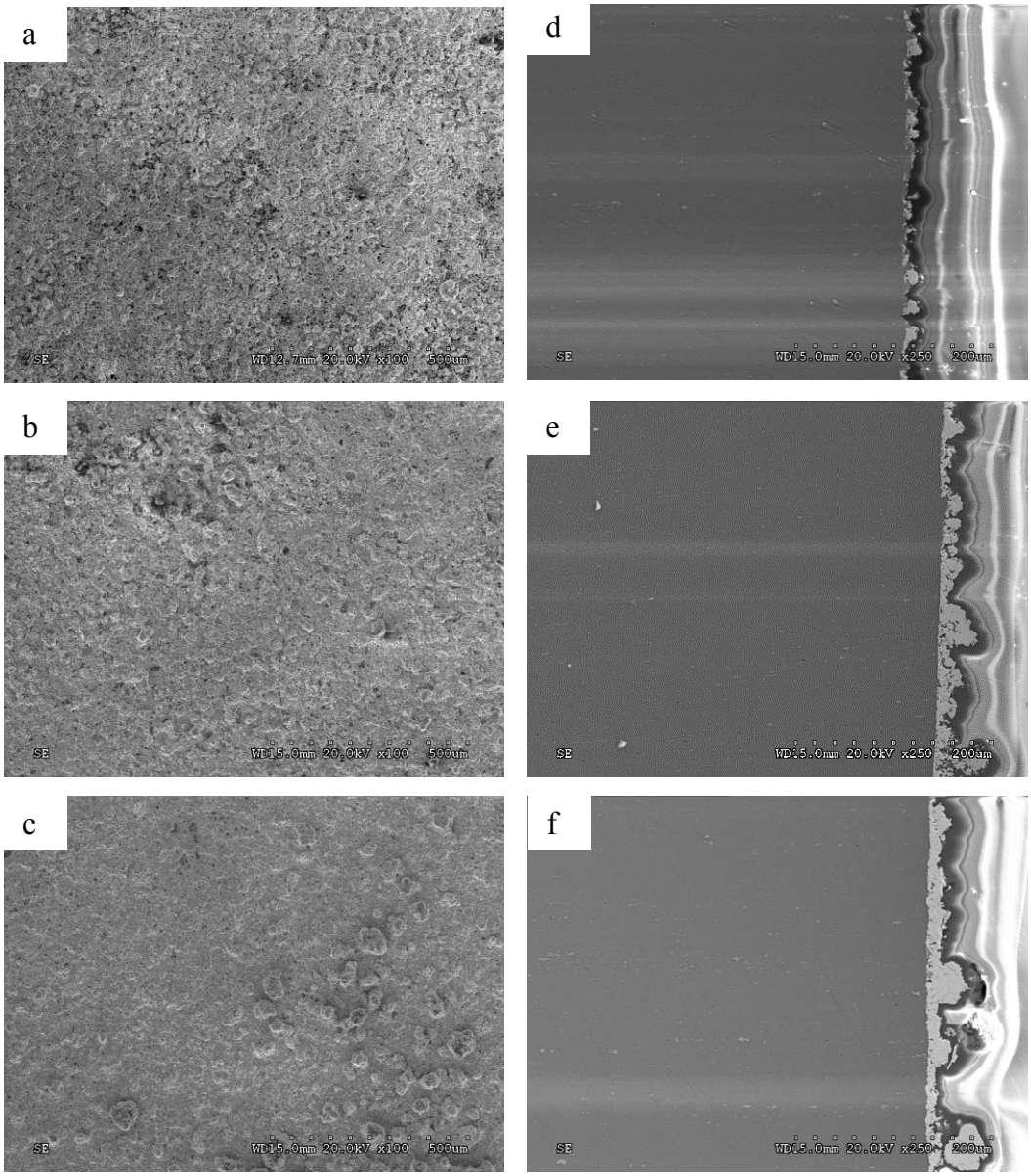

Figure 6-31. Surface and cross-sectional SEM micrographs of EPP deposited Ni on Al at 185 V for 30 s (a, d), 60 s (b, e), and 90 s (c,f) after OCP vs. time measurements.

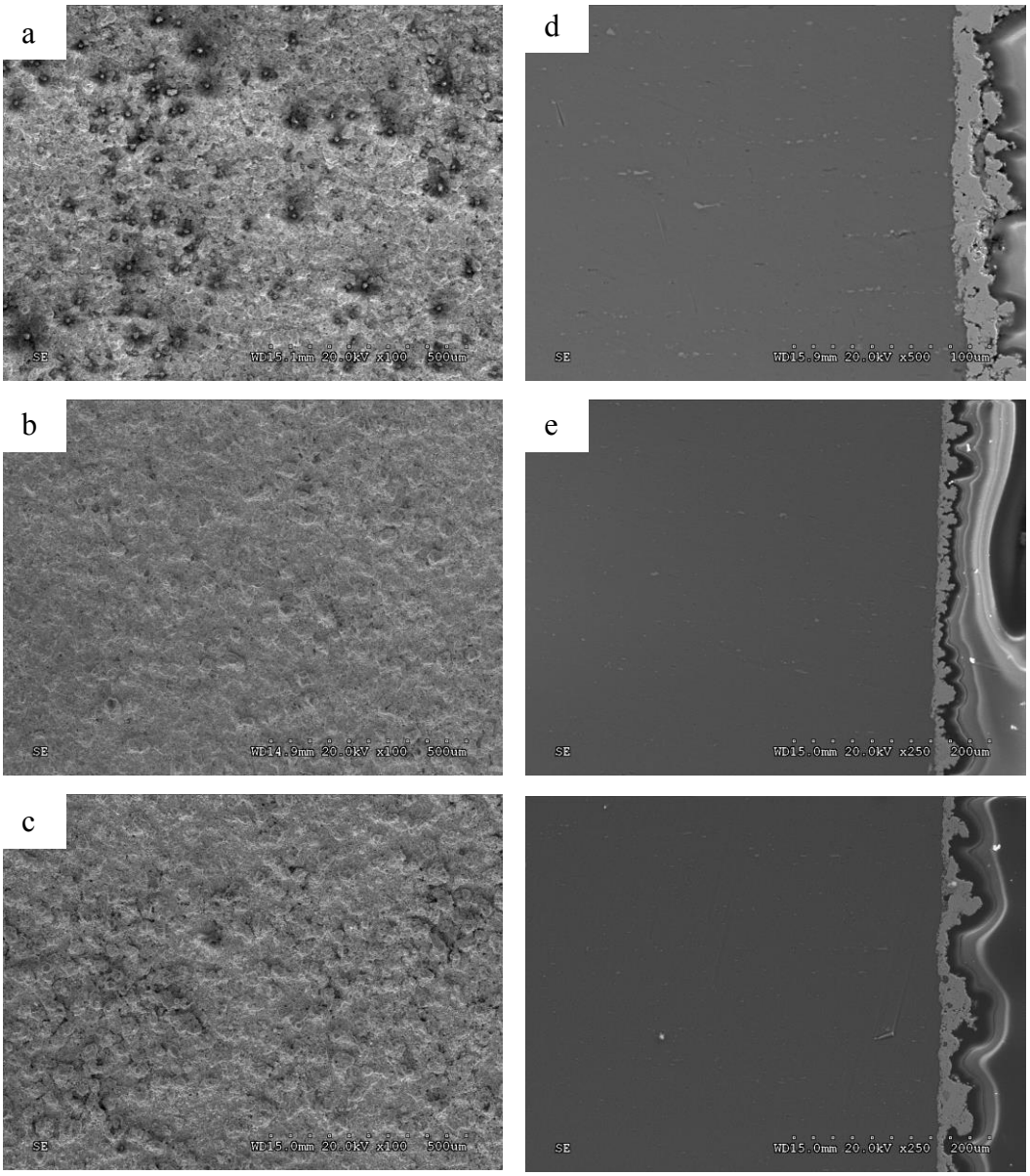

Figure 6-32. Surface and cross-sectional SEM micrographs of EPP deposited Ni on Al at 210/185 V for 30 s (a, d), 60 s (b, e) and 90 s (c, f) after exposure to 3.5% NaCl aqueous electrolyte in open air for 10,000 s.

6.3.4.2 Anodic Polarization

Anodic polarization measurements were conducted on the six coated samples, 185 V – 30 s, 60 s, and 90 s and 210/185 V – 30 s, 60 s, 90 s, and two control samples, Ni 200 (referred to as Ni) and Al 1100 (referred to as Al) in order to determine the corrosion potential and corrosion rate of the samples and compare them to the two bulk materials. Anodic polarization results are presented below in Figure 6-33 and a zoomed in version of the deposited samples is given as Figure 6-34 for reference. Additionally, Table 6-5 lists the specific corrosion potential (E_{corr}) and corrosion rate (I_{corr}) of each of the samples measured. A clear improvement of all of the coated samples over the corrosion potential of the control Al sample is visible and an improvement of the 210/185 V samples over the 185 V samples is also evident. The E_{corr} values of the samples all show improvements with increasing deposition time. However, it is important to note that the samples containing the intermetallic interlayer have more noble E_{corr} values with the 30 s deposition possessing an interlayer having an E_{corr} value approximately the same as the E_{corr} value of the 90 s deposition lacking the intermetallic interlayer. This indicates that the inclusion of the interlayer has a clear effect in improving the corrosion resistance of the coating. It is believed that this is due to the il f yer acting to establish a higher melting temperature base upon which the subsequent 185 V processing step is then able to deposit onto, in effect reducing the detrimental effect that is apparent when depositing on Al. This likely results in a denser and more uniform coating than that achieved when the interlayer is not present. The greatest corrosion resistance is achieved in the 90 s coating with the included intermetallic interlayer (210 V followed by 185 V). In this sample the E_{corr} value increases from -1128 mV of the Al control up to -694 mV, an increase of 434 mV or ~38.5%. It should be noted that the corrosion rate does not appear to show

any significant change between the coated samples or with that of the Al control sample. This may be due to the method by which the samples were mounted involving the application of Microstop to the side of the samples and over the edge to prevent inaccurate measurements due to the poor deposition properties present at these locations. This method decreases the exposed surface area and is not completely uniform between samples. Furthermore, due to the high roughness of the EPP coating, the actual surface area is far higher than that of the measured surface area which suggests that the corrosion rate is actually lower than what is calculated. Further inspection of the results reveals that the E_{corr} of the coatings are approximately the same as $E_{pitting}$ of the substrate material. When comparing the corrosion rates at the E_{corr} of the coatings, a large improvement is observed in the coatings, with the $I_{pitting}$ value of the substrate being ~3 μa/cm^2, almost double that of the I_{corr} values for the coatings.

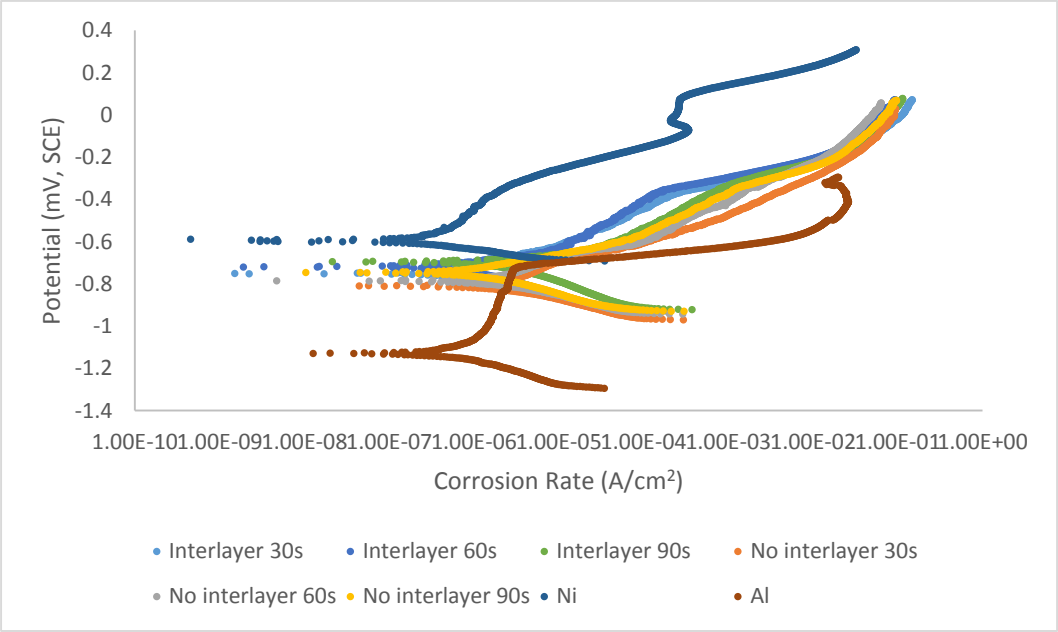

Figure 6-33. Anodic polarization plots of EPP deposited Ni on Al as well as Al and Ni control samples.

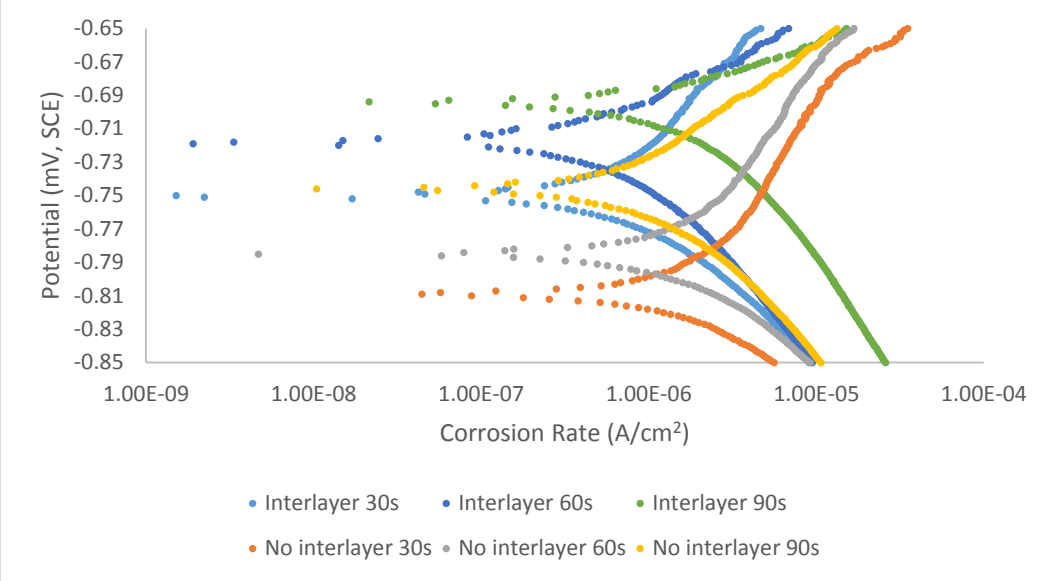

Figure 6-34. Anodic polarization plote of EPP Ni deposited on Al with y-axis reduced. Presented for reference.

Table 6-5. E_{corr} and I_{corr} values for EPP deposited Ni on Al as well as Ni and Al control samples.

Sample	E_{corr} (mV, SCE)	I_{corr} (µA/cm^2)
Ni	-595	0.28
Al	-1128	1.62
W/Interlayer		
90 s	-694.4	1.69
60 s	-718.2	1.51
30 s	-750.3	1.72
W/o Interlayer		
90 s	-746	1.34
60 s	-785	1.52
30 s	-809	1.61

Surface SEM of the samples are presented below in Figure 6-35, for the 185 V depositions, and Figure 6-36 for the 210/185 V depositions. It should be noted that the anodic polarization scans were driven up into the dissolution regime intentionally, and, thus, the presence of pitting of the coatings is expected. Inspection of the coating surfaces did not reveal the presence of large pits on the surface of the 30 s deposition without the interlayer. Instead large quantities of debris was evident and a great number of smaller pits was observed. This is likely due to the low quality of the coating in this instance, which would lead to pitting becoming active in the Al substrate without needing to first penetrate through the Ni EPP coating. In all of the other samples the presence of large pits was observed with fewer pits being seen on the 90 s deposition but with overall pit size appearing to be larger in this case. Additionally, cross-sectional observation revealed that the pits were extremely large and extended deep into the Al substrate and acted to undercut the Ni coating. Due to the much more noble behavior of Ni compared to Al this was expected. It should be mentioned that while Ni does improve the corrosion resistance of Al, it does so as a barrier layer. The results of the anodic polarization experiments clearly show that should this barrier layer become breached, the Al substrate will rapidly corrode.

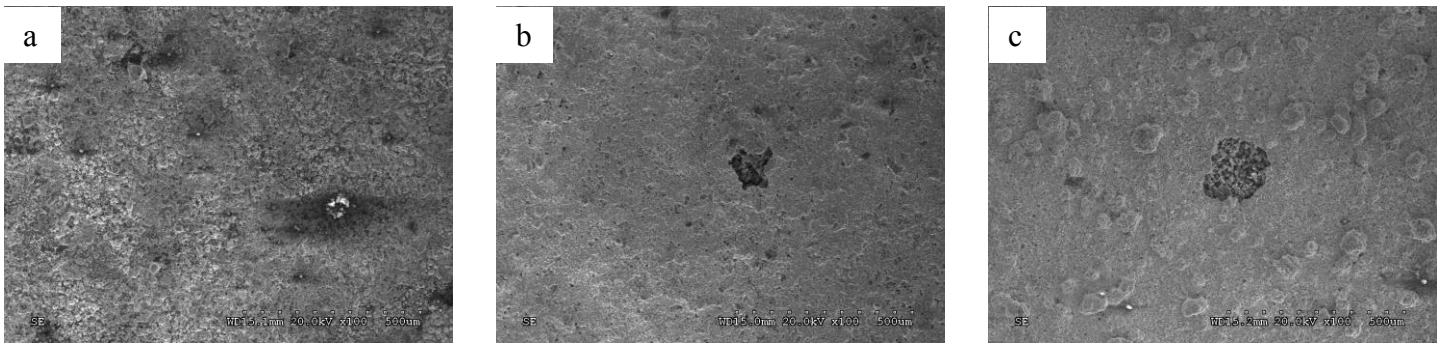

Figure 6-35. Surface SEM micrograph of EPP deposited Ni on Al at 185 V and (a) 30 s, (b) 60 s, and (c) 90 s after anodic polarization measurements.

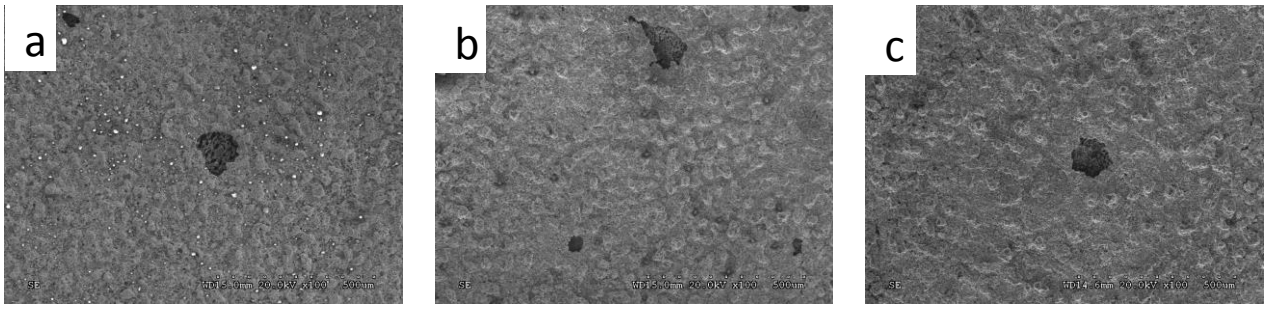

Figure 6-36. Surface SEM micrograph of EPP deposited Ni on Al at 210 V, 30 s and (a) 30 s, (b) 60 s, (c) 90 s after anodic polarization measurements

6.4 Discussion

The deposition of Ni via EPP onto Al substrates revealed a strong correlation between voltage and morphology and elemental composition of the surface coating. It was determined that at lower voltages (185 V) a dense, uniform, and continuous coating was achievable consisting of ~100% Ni. At higher voltages (210 V) the surface was observed to consist largely of raised ridges of intermetallics with an elemental composition consisting of both Ni and Al, although the exact proportion of these two elements was seen to vary. The ability to form these surface intermetallics is a notable achievement, even though the final coating is highly discontinuous. Surface coatings were produced with two different voltage profiles, the first consisting of 185 V for 30 s, 60 s, or 90 s, and the second consisting of an initial 210 V step for 30 s, followed by a second processing step at 185 V for 30 s, 60 s, or 90 s. The inclusion of this initial processing condition resulted in a coating possessing a dispersed interlayer consisting of varios Ni-Al intermetallics covered by a dense Ni coating. Both voltage profiles resulted in a dense and continuous coating. Of note was the demonstrated ability for the EPP

process to remove O from the Al surface during deposition, a benefit of high importance and one not observed in other deposition techniques. Tribology experiments were performed with a pin-on-disk tribometer and a reduction in both the bear rate and coefficient of friction was observed for the EPP coated samples compared to the uncoated Al substrate with slightly larger reduction in the wear rate seen in the coating containing the 210 V interlayer, although this corresponded to a slight increase in the coefficient of friction for these samples compared to the non-interlayer containing coatings. This was credited to the ability of the harder intermetallic interlayer to better support and distribute the load applied to the Ni surface coating. Corrosion experiments reveal a shift of the corrosion potential towards the noble regime with greater improvement correlating with longer deposition time. Once again, slightly better performance was witnessed with the coating containing the 210 V intermetallic interlayer. The cause of this improvement was attributed to the more uniform deposition of the Ni surface layer which the interlayer likely resulted in. Best corrosion resistance was determined to be from the 210/185 V processing condition deposited for 90 s. In this case the E_{corr} value was found to shift 434 mV in the positive, nobler, direction.

Chapter 7

Conclusions

7.1 Effect of Process Variations on Surface Morphology and Current Density of EPP Cleaning on 1018 Steel

Experimentation was conducted in order to determine optimum processing conditions and to explore the capabilities of the process and the recently built in-house EPP device. It was determined that electrolyte concentration, flow-rate, anode-cathode separation distance, and voltage controllability all played crucial roles in determining the final quality of EPP coatings. Optimum conditions for EPP cleaning were found to be: a separation distance of 5 mm, a flow rate of 2 L/min, and an electrolyte concentration of 12% $NaHCO_3$. Furthermore, the ability of the power supply to accurately control the applied, set voltage was determined to have critical importance. An inability to accurately control the voltage was determined to result in a high rate of microarcing which led to sever coating damage. EPP cleaning was conducted utilizing the determined results which

7.2 EPP Deposition and Characterization of Ni deposited on Fe

Deposition of Ni onto Fe substrates via EPP resulted in the formation of a dense, continuous, nanocrystalline Ni coating. Depositions were conducted at times of 10 s, 20 s, and 30 s and it was determined that coatings produced at less than 20 s resulted in poor coating coverage of the substrate and the exposure of the underlying Fe. Corrosion experiments were conducted which revealed an improvement of the corrosion potential

and corrosion rate of the coated samples compared to the underlying substrate. The coating properties were observed to lie between those observed for Fe and those observed for Ni, with increasing improvement seen with increasing coating deposition times. It should be noted that the final corrosion properties of the coatings remained below those of Ni, possibly due to the nanocrystalline nature of the coatings, or possibly due to an un-observed presence of microcracks in the coating. Best corrosion protection results were found to be from a deposition time of 30 s which resultd in a noble shift of the E_{corr} value of ~200 mV and a decrease in the I_{corr} of ~37%.

7.3 EPP Deposition and Characterization of Ni deposited on Al

Deposition of Ni onto Al substrates was conducted with EPP. Two separate methods were used, a single step deposition at 185 V for 30 s, 60 s, or 90 s, and a two-step approach consisting of an initial 210 V step for 30 s followed by 185 V for 30 s, 60 s, or 90 s. EPP depositions at 210 V was shown to result in a surface consisting of raised ridges with elemental compositions consisting of intermetallics of Ni and Al, although the exact percentage of this intermetallic was seen to vary. Depositions carried out at 185 V resulted in a dense, continuous surface coating with an elemental composition of ~100% Ni. Furthermore, and of high importance, the interface between the Al substrate and the coating was observed to be relatively O free, demonstrating that the H^+ plasma of the EPP process acts to both clean and coat simultaneously. At this time, no other coating technology is known to do this. Tribological experimentation revealed that the addition of EPP deposited Ni severely increased the wear resistance and decreased the coefficient of friction of the surface. Comparison to commercially pure Ni was hampered by the difficulty in accurately comparing the results due to the high roughness of the EPP

surface. The inclusion of the 210 V interlayer was shown to slightly improve the wear resistance but also to slightly increase the coefficient of friction when compared to the EPP sample without it, likely due to the presence of a harder base on which load distribution can take place. Corrosion experimentation results showed that the EPP Ni layer led to a noble shift in the corrosion potential compared to the uncoated Al substrate. While it was expected that the corrosion rate would decrease significantly, results proved inconclusive, likely due to the discrepancy in measured area vs. true area owing the very high roughness of the coated samples. The EPP coating were seen to have corrosion potentials between the Al substrate and that of commercially pure Ni, with increasing (more noble) corrosion potential observed to correlate with increasing deposition time. It should be noted that the corrosion potentials remain below that of Ni, which may be due to the nanocrystalline nature of the coatings or possibly due to the presence of un-observed microcracks in the coating allowing for gradual exposure of the substrate to the electrolyte. Once again, the inclusion of the 210 V interlayer resulted in slightly higher performance of the coating than the EPP Ni coating without the interlayer. This is attributed to the more uniform deposition which is likely caused by this initial processing step which results in fewer microcracks in the coating surface. Corrosion results were found to be best for samples deposited with the 210/185 V process at a deposition time of 90 s. The E_{corr} value was found 434 mV in the more noble direction when compared to the underlying Al substrate.

Appendix A

EPP Sample

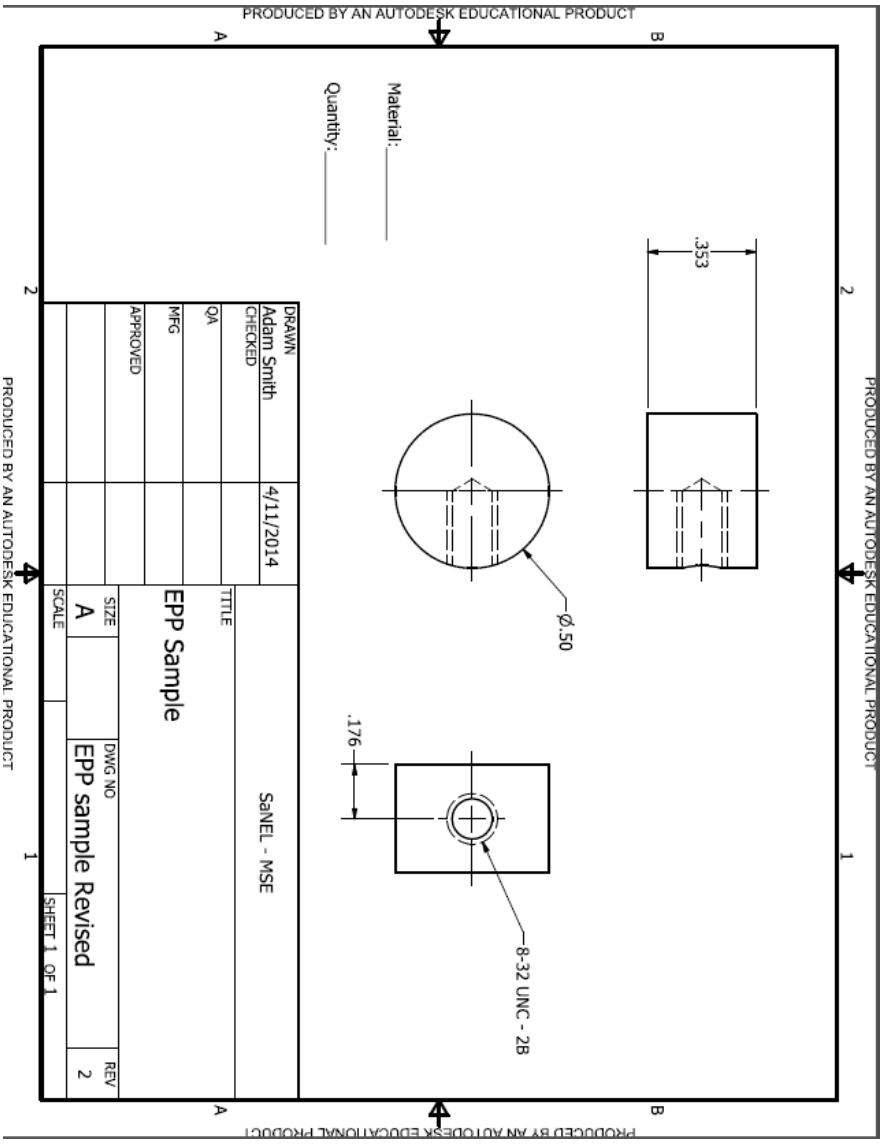
PRODUCED BY AN AUTODESK EDUCATIONAL PRODUCT
Material:
Quantity:
.353
Ø.50
.176
8-32 UNC - 2B
DRAWN
Adam Smith
4/11/2014
CHECKED
QA
MFG
APPROVED
SaMEL - MSE
TITLE
EPP Sample
SIZE
A
DWG NO
EPP sample Revised
REV
2
SCALE
SHEET 1 OF 1

Appendix B

Replaceable Anode

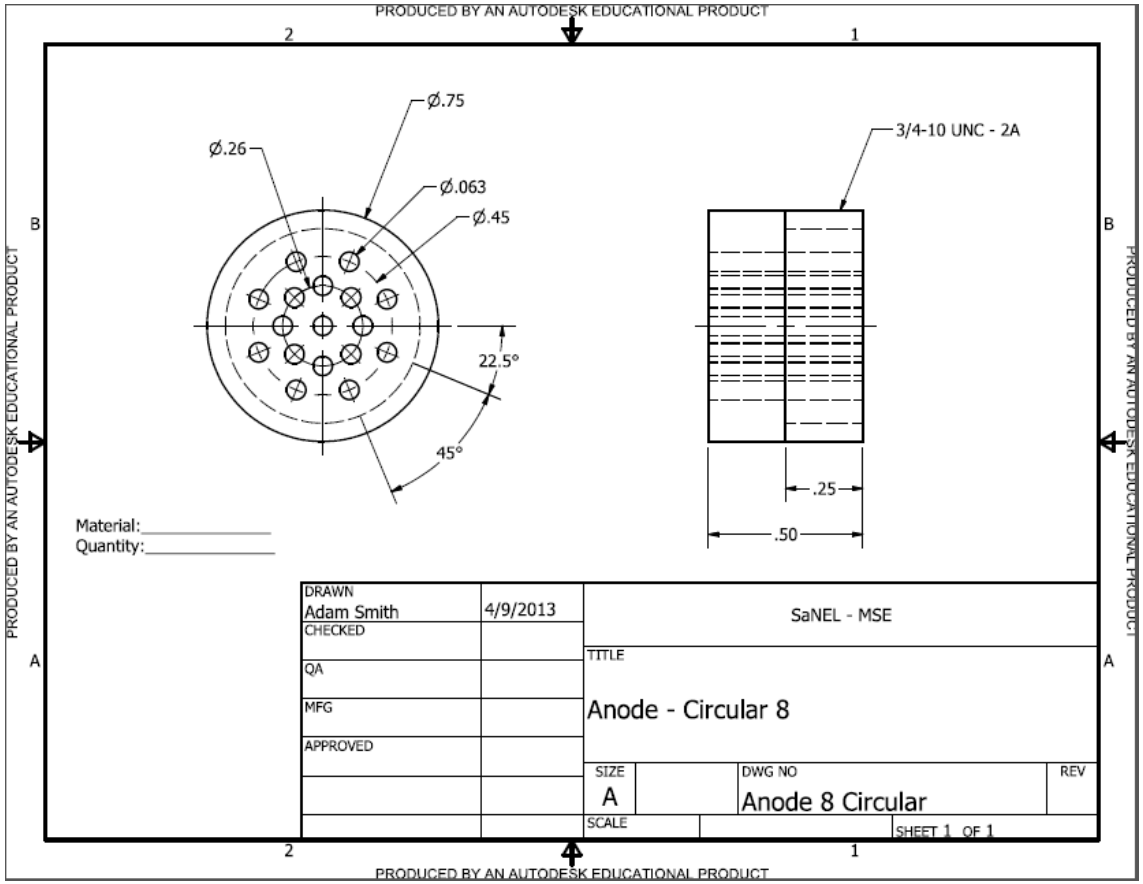
PRODUCED BY AN AUTODESK EDUCATIONAL PRODUCT
Ø.75
Ø.26
Ø.063
Ø.45
22.5°
45°
3/4-10 UNC - 2A
.25
.50
Material:
Quantity:
DRAWN
Adam Smith
4/9/2013
CHECKED
QA
MFG
APPROVED
SaNEL - MSE
TITLE
Anode - Circular 8
SIZE
A
DWG NO
Anode 8 Circular
REV
SCALE
SHEET 1 OF 1

References

[1] C. E. da Costa, W. C. Zapata, F. Velasco, J. M. Ruiz-Prieto and J. M. Torralba, "Wear behaviour of aluminum reinforced with nickel aluminid MMCs," *Journal of Materials Processing Technology,* pp. 66-70, 1999.

[2] S. A. Kori and T. M. Chandrashekharaiah, "Studies on the dry sliding wear behaviour of hypoeutectic and eutectic Al-Si alloys," *Wear,* no. 263, pp. 745-755, 2007.

[3] B. Venkataraman and G. Sundararajan, "Correleation between the characteristics of the mechanically mixed layer and wear behaviour of aluminium, Al-7075 and Al-MMCs," *Wear,* no. 245, pp. 22-38, 2000.

[4] C. Cionea, Microstructural Evolution of Surface Layers during Electrolytic Plasma Processing, Arlington, TX: University of Texas - Arlington, 2010.

[5] J. J. Selvan, G. Soundararajan and K. Subramanian, "Laser alloying of aluminum with electrodeposited nickel: optimisation of plating thickness and processing parameters," *Surface & Coatings Technology,* pp. 117-127, 2000.

[6] P. Bialucki and S. Kozerski, "Study of adhesion of different plasma-sprayed coatings to aluminum," *Surface & Coatings Technology,* pp. 2061-2064, 2006.

[7] P. Sahoo and S. K. Das, "Tribology of electroless nickel coatings - A review," *Materials and Design,* pp. 1760-1775, 2011.

[8] S. S. Yazdi, F. Ashrafizadeh and A. Hakimizad, "Improving the grain structure and adhesion of Ni-P coating to 3004 aluminum substrate by nanostructured anodic film layer," *Surface & Coatings Technology,* pp. 561-566, 2013.

[9] V. Saxena, R. U. Rani and A. K. Sharma, "Studies on ultra high so,ar absorber black electroless nickel coatings on aluminum alloys for space application," *Surface & Coatings Technology,* pp. 855-862, 2006.

[10] A. R. Shashikala, A. K. Sharma and D. R. Bhandari, "Solar selective black nickel-cobalt coatings on aluminum alloys," *Solar Energy Materials and Solar Cells,* pp. 629-635, 2007.

[11] I. Apachitei and J. Duszczyk, "Autocatalytic nickel coatings on aluminum with improved abrasive wear resistance," *Surface & Coatings Technology,* pp. 89-98, 2000.

[12] S. Sadreddini and A. Afshar, "Corrosion resistance enhancement of Ni-P-nano SiO2 composite coatings on aluminum," *Applied Surface Science,* pp. 125-130, 2014.

[13] B. Loonyuk, I. Apachitei and J. Duszczyk, "Effect of high phosphorus electroless nickel coating on fatigue life of Al-Cu-Mg-Fe-Ni alloy," *Scripta Materialia,* pp. 783-786, 2007.

[14] M. Franco, W. Sha, S. Malinov and R. Rajendran, "Phase composition, microstructure and microhardness of electroless nickel composite coating co-deposited with SiC on cast aluminum LM24 alloy substrate," *Surface & Coatings Technology,* pp. 755-763, 2013.

[15] A. H. Committee, Metallography, Structures and Phase Diagrams, Metals Park, OH: American Society of Metals, 1973.

[16] C. Sanchez Bautista, A. Ferriere, G. P. Rodriguez and M. Lopez-Almodovar, "NiAl intermetallic coatings eleaborated by a solar assisted SHS process," *Intermetallics,* no. 14, pp. 1270-1275, 2006.

[17] M. Salehi, F. Karimzadeh and A. Tahvilian, "Formation of Ti-Ni intermetallic coatings on carbon tool steel by a duplex process," *Surface & Coatings Technology,* no. 148, pp. 55-60, 2001.

[18] M. Alaeddine, R. Ranganathan, T. Ando and C. C. Doumanidis, "Modeling intermetallic coating growth during reactive thermal processing of layered precursors," *Surface & Coatings Technology,* no. 200, pp. 5181-5192, 2006.

[19] Y. Ding, Y. Zhang, D. Northwood and A. T. Alpas, "PVD NiAl intermetallic coatings: microstructure and mechanical properties," *Surface and Coatings Technology,* pp. 483-489, 1997.

[20] P. J. Blau and C. E. DeVore, "Sliding friction and wear behaviour of several nickel aluminide alloys under dry and lubricated conditions," *Tribology International,* vol. 23, no. 4, pp. 226-234, 90.

[21] Y. Wang, Z. Wang, Y. Yang and W. Chen, "The effects of ceria on the mechanical properties and thermal shock resistance of thermal sprayed NiAl intermetallic coatings," *Intermetallics,* no. 16, pp. 682-688, 2008.

[22] C. Choux, A. J. Kulinska and S. Chevalier, "High temperature reactivity of nickel aluminide diffusion coatings," *Intermetallics,* no. 16, pp. 1-9, 2008.

[23] J. A. Hearley, J. A. Little and A. J. Sturgeon, "The erosion behaviour of NiAl intermetallic coatings produced by high velocity oxy-fuel thermal spraying," *Wear,* pp. 328-333, 1999.

[24] Y. Wang, W. Chen and L. Wnag, "Micro-indentation and erosion of thermal sprayed NiAl intermetallic-based alloy coatings," *Wear,* no. 254, pp. 350-355, 2003.

[25] P. Gupta, G. Tenhundfeld, E. O. Daigle and D. Ryabkov, "Electrolyti plasma technology: Science and engineering - An overview," *Surface and Coatings Technology,* no. 201, pp. 8746-8760, 2007.

[26] A. l. Yerokhin, L. O. Snizhko, N. L. Gurevina, A. Leyland, A. Pilkington and A. Matthews, "Discharge characterization in plasma electrolytic oxidation of aluminium," no. 36, pp. 2110-2120, 2003.

[27] M. Aliofkhazraei and A. S. Roohaghdam, "A novel method for preparing aluminum diffusion coating by nanocrystalline plasma electrolysis," *Electrochemistry Communications,* no. 9, pp. 2686-2691, 2007.

[28] A. L. Yerokhin, X. Nie, A. Leyland, A. Matthews and S. J. Dowey, "Plasma electrolysis for surface engineering," *Surface and Coatings Technology,* no. 122, pp. 73-93, 1999.

[29] E. I. Meletis, X. Nie, F. L. Wang and J. C. Jiang, "Electrolytic plasma processing for cleaning and metal-coating of steel surfaces," *Surface and Coatings Technology,* no. 150, pp. 246-256, 2002.

[30] M. Aliofkhazraei, A. Sabour Rouhaghdam and P. Gupta, "Nano-Fabrication by cathodic plasma electrolysis," *Critical Reviews in Solid State and Materials Science,* vol. 36, no. 3, pp. 174-190, 2011.

[31] A. Yerokhin, A. Pilkington and A. Matthews, "Pulse current plasma assisted electrolytic cleaning of AISI 4340 steel," *Journal of Materials Processing Technology,* vol. 210, pp. 54-63, 2010.

[32] P. Gupta, G. Tenhundfeld, E. O. Daigle and P. J. Schilling, "Synthesis and characterization of hard metal coatings by electro-plasma technology," *Surface & Coatings Technology,* vol. 200, pp. 1587-1594, 2005.

[33] W. C. Gu, G. H. Lu, H. Chen, G. L. Chen, W. R. Feng, G. L. Zhang and S. Z. Yang, "Investigation of morphology and composition of plasma electrolytic oxidation coatings in systems of Na2SiO3-NaOH and (NaPO3)6-NaOH," no. 182, pp. 28-33, 2007.

[34] Y. Ma, H. Hu, D. Northwood and X. Nie, "Ptimization of the electrolytic plasma oxidation process for corrosion protection of magnesium alloy AM50 using Taguchi method," *Journal of Materials Processing Technology,* no. 182, pp. 58-64, 2007.

[35] S. S. Byeon, K. Wang, Y. G. Jung and B. H. Koo, "Characteristic of AlON-Al2O3 coatings on Al6061 alloy by electrolytic plasma processing in aluminate and nitride electrolytes.," no. 204, pp. 3196-3199, 2010.

[36] L. Ceschini, E. Lanzoni, C. Martini, D. Prandstraller and G. Sambogna, "Comparison of dry sliding friction and wear of Ti6Al4V alloy treated by plasma electrolytic oxidation and PVD coating," *Wear,* no. 264, pp. 86-95, 2008.

[37] T. Abdulla, A. Yerokhin and R. Goodall, "Effect of plasma electrolytic oxidation coating on the specific strength of open-cell aluminium foams," *Materials and Design,* no. 32, pp. 3742-3749, 2011.

[38] C. S. Dunleavy, I. O. Golosnoy, J. A. Curran and T. W. Clyne, "Characterisation of discharge events during plasma electrolytic oxidation.," no. 203, pp. 3410-3419, 2009.

[39] A. L. Yerokhin, X. Nie, A. Leyland, A. Matthews and S. J. Dowey, "Plasma electrolysis for surface engineering," no. 122, pp. 73-93, 1999.

[40] E. Matykina, R. Arrabal, P. skeldon and G. E. Thompson, "Optimisation of the electrolytic oxidation process efficiency on aluminium.," no. 42, pp. 221-226, 2009.

[41] X. Zhang, Y. Zhang, L. Chang, Z. Jiang, Z. Yao and X. Liu, "Effects of frequency on growth process of plasma electrolytic oxidation coating," *Materials Chemistry and Physics,* no. 132, pp. 909-915, 2012.

[42] H. Kalkanci and S. C. Kurnaz, "The effect of process parameters on mullite-based plasma electrolytic coatings," *Science and Coatings Technology,* no. 203, pp. 15-22, 2008.

[43] K. Wang, S. S. Byeon, Y. G. Jung and B. H. Koo, "effect of the nitrogen inducing agent ont he corrosion behavior of the oxide coatings prepared by electrolytic plasma processing on the Al2021 alloy," *Ceramics International,* no. 38S, pp. S669-S672, 2012.

[44] Z. Yao, Y. Jian and Z. W. F. W. Z. Jiang, "Preparation and structure of ceramic coatings containing zironium oxide on Ti alloy by plasma electrolytic oxidation," *Journal of Materials Processing Technology,* no. 205, pp. 303-307, 2008.

[45] M. A. Béjar and R. Henríquez, "Surface hardening of steel by plasma-electrolysis boronizing," *Materials and Design,* no. 30, pp. 1726-1728, 2009.

[46] X. M. Li and Y. Han, "Porous nanocrystalline Ti(CxN1-x) thick films by plasma electrolytic carbonitriding," *Electrochemistry Communications,* no. 8, pp. 267-272, 2006.

[47] M. Aliofkhazraei, C. Morillo, R. Miresmaeili and A. Sabour Rouhaghdam, "Carburizing of low-melting-point metals by pulsed nanocrystalline plasma electrolytic carburizing," *Surface and Coatings Technollogy,* no. 202, pp. 5493-5496, 2008.

[48] F. Çavuşlu and M. Usta, "Kinetics and mechanical study of plasma electrolytic carburizing of pure iron.," *Applied Surface Science,* no. 257, pp. 4014-4020, 2011.

[49] D. J. Guidry, K. Lian, J. C. Jian and E. I. Meletis, "Tribological Behavior of Nanocrystalline Nickel," *Journal of Nanoscience and Nanotechnology,* pp. 4156-4163, 2009.

[50] A. L. Yerokhin, L. O. Snizhko, N. L. Gurevina, A. Leyland, A. Pilkington and A. Matthews, "Discharge characterization in plasma electrolytic oxidation of aluminium," *Journal of Physics D: Applied Physics,* no. 36, pp. 2110-2120, 2003.

Biographical Information

Adam Smith attained a Bachelor's of Science in Mechanical Engineering from Lake Superior State University in 2009. After graduation he enrolled in the University of Texas – Arlington's Materials Science Department and began in January 2010 in the department's B.S. to PhD program.

At UTA he became a member of Dr. Efstathios Meletis' Surface and Nano-Engineering Laboratory. He conducted research on several topics including the incorporation of Ni or Ti nanoparticles into friction stir welds in Al, investigated the mechanical properties of hollow gold nanoparticles, performed work in collaboration with University of Texas – Southwest's Medical Center on the properties of surgical meshes, and proposed his own research topic on deposition of Ni onto Al via Electrolytic Plasma Processing. He presented twice at the ICMCTF conference in San Diego (2011 and 2014) and has had one paper published on the properties of surgical meshes. A second paper, on corrosion of Ni coatings on Fe substrates deposited via EPP, is in review.

He has interned at Argonne National Laboratory in the tribology group of the Energy Systems Division, where he aided wear research on thermoelectrically borided D2 tool steel. Prior to graduation Adam moved to Albany, NY with his wife in order for her to attain a doctorate in Public Health.